Large-Scale Testing and Numerical Modeling of Full- and Reduced-Scale Rail Car Floor Assemblies

REPORT DOCUMENTATION PAGE

1. REPORT DATE *(DD-MM-YYYY)*	**2. REPORT TYPE** Technical Report	**3. DATES COVERED** *(From - To)* October 2018–June 2021

4. TITLE AND SUBTITLE
Large-Scale Testing and Numerical Modeling of Full- and Reduced-Scale Rail Car Floor Assemblies

5a. CONTRACT NUMBER
693JJ618C000022

5b. GRANT NUMBER

5c. PROGRAM ELEMENT NUMBER

6. AUTHOR(S)
Christian Rippe 0000-0002-8283-5639
Brian Lattimer 0000-0002-4743-6122
Anil Kapahi 0000-0001-9279-7544

5d. PROJECT NUMBER

5e. TASK NUMBER

5f. WORK UNIT NUMBER

7. PERFORMING ORGANIZATION NAME(S) AND ADDRESS(ES)
Jensen Hughes, Inc.
3610 Commerce Drive, Suite 817
Baltimore, MD 21227-7164

8. PERFORMING ORGANIZATION REPORT NUMBER

9. SPONSORING/MONITORING AGENCY NAME(S) AND ADDRESS(ES)
U.S. Department of Transportation
Federal Railroad Administration
Office of Railroad Policy and Development
Office of Research, Development and Technology
Washington, DC 20590

10. SPONSOR/MONITOR'S ACRONYM(S)

11. SPONSOR/MONITOR'S REPORT NUMBER(S)
DOT/FRA/ORD-22/36

12. DISTRIBUTION/AVAILABILITY STATEMENT
This document is available to the public through the FRA website.

13. SUPPLEMENTARY NOTES
COR: Melissa Shurland

14. ABSTRACT
A previously developed methodology for reducing the physical scale of test articles for fire performance testing of rail car floors was benchmarked using a series of large-scale tests and validated finite element simulations. The simulations showed that the experimental differences between the full-scale and reduced-scale test articles was due to testing discrepancies in the actual thermal and mechanical boundary conditions observed during the tests. While not directly validating the reduction methodology, this effort found no fundamental flaws in the methodology if the reduced-scale tests are properly executed.

15. SUBJECT TERMS
Rail car, fire performance, floor assembly, large-scale testing, numerical modeling, reduced-scale test article, rolling stock

16. SECURITY CLASSIFICATION OF:			**17. LIMITATION OF ABSTRACT**	**18. NUMBER OF PAGES**	**19a. NAME OF RESPONSIBLE PERSON** Anil Kapahi
a. REPORT	**b. ABSTRACT**	**c. THIS PAGE**		138	**19b. TELEPHONE NUMBER** *(Include area code)* 443-313-9795

METRIC/ENGLISH CONVERSION FACTORS

ENGLISH TO METRIC

LENGTH (APPROXIMATE)

1 inch (in)	=	2.5 centimeters (cm)
1 foot (ft)	=	30 centimeters (cm)
1 yard (yd)	=	0.9 meter (m)
1 mile (mi)	=	1.6 kilometers (km)

AREA (APPROXIMATE)

1 square inch (sq in, in^2)	=	6.5 square centimeters (cm^2)
1 square foot (sq ft, ft^2)	=	0.09 square meter (m^2)
1 square yard (sq yd, yd^2)	=	0.8 square meter (m^2)
1 square mile (sq mi, mi^2)	=	2.6 square kilometers (km^2)
1 acre = 0.4 hectare (he)	=	4,000 square meters (m^2)

MASS - WEIGHT (APPROXIMATE)

1 ounce (oz)	=	28 grams (gm)
1 pound (lb)	=	0.45 kilogram (kg)
1 short ton = 2,000 pounds (lb)	=	0.9 tonne (t)

VOLUME (APPROXIMATE)

1 teaspoon (tsp)	=	5 milliliters (ml)
1 tablespoon (tbsp)	=	15 milliliters (ml)
1 fluid ounce (fl oz)	=	30 milliliters (ml)
1 cup (c)	=	0.24 liter (l)
1 pint (pt)	=	0.47 liter (l)
1 quart (qt)	=	0.96 liter (l)
1 gallon (gal)	=	3.8 liters (l)
1 cubic foot (cu ft, ft^3)	=	0.03 cubic meter (m^3)
1 cubic yard (cu yd, yd^3)	=	0.76 cubic meter (m^3)

TEMPERATURE (EXACT)

[(x-32)(5/9)] °F = y °C

METRIC TO ENGLISH

LENGTH (APPROXIMATE)

1 millimeter (mm)	=	0.04 inch (in)
1 centimeter (cm)	=	0.4 inch (in)
1 meter (m)	=	3.3 feet (ft)
1 meter (m)	=	1.1 yards (yd)
1 kilometer (km)	=	0.6 mile (mi)

AREA (APPROXIMATE)

1 square centimeter (cm^2)	=	0.16 square inch (sq in, in^2)
1 square meter (m^2)	=	1.2 square yards (sq yd, yd^2)
1 square kilometer (km^2)	=	0.4 square mile (sq mi, mi^2)
10,000 square meters (m^2)	=	1 hectare (ha) = 2.5 acres

MASS - WEIGHT (APPROXIMATE)

1 gram (gm)	=	0.036 ounce (oz)
1 kilogram (kg)	=	2.2 pounds (lb)
1 tonne (t)	=	1,000 kilograms (kg)
	=	1.1 short tons

VOLUME (APPROXIMATE)

1 milliliter (ml)	=	0.03 fluid ounce (fl oz)
1 liter (l)	=	2.1 pints (pt)
1 liter (l)	=	1.06 quarts (qt)
1 liter (l)	=	0.26 gallon (gal)
1 cubic meter (m^3)	=	36 cubic feet (cu ft, ft^3)
1 cubic meter (m^3)	=	1.3 cubic yards (cu yd, yd^3)

TEMPERATURE (EXACT)

[(9/5) y + 32] °C = x °F

QUICK INCH - CENTIMETER LENGTH CONVERSION

Inches	0	1	2	3	4	5
Centimeters	0 1 2 3 4 5	6 7 8 9	10 11	12 13		
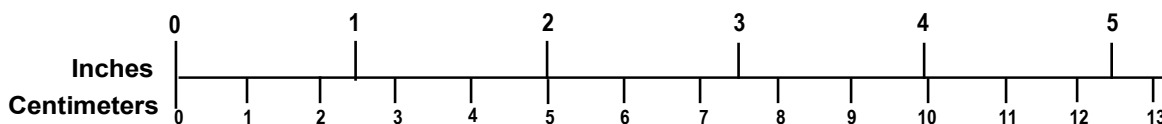
QUICK FAHRENHEIT - CELSIUS TEMPERATURE CONVERSIO

°F	-40°	-22°	-4°	14°	32°	50°	68°	86°	104°	122°	140°	158°	176°	194°	212°
°C	-40°	-30°	-20°	-10°	0°	10°	20°	30°	40°	50°	60°	70°	80°	90°	100°
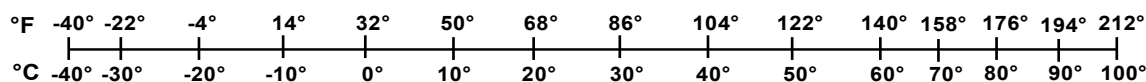
For more exact and or other conversion factors, see NIST Miscellaneous Publication 286, Units of Weights and Measures. Price $2.50 SD Catalog No. C13 10286

Acknowledgments

Contents

Illustrations

Tables

Equations

Executive Summary

This research is the latest portion of an ongoing effort to investigate the feasibility of reducing the physical size requirements of test articles for fire performance testing of passenger rail car floor assemblies. The Federal Railroad Administration (FRA) funded Jensen Hughes to conduct this research in December 2016, with the current phase conducted in October 2018 through June 2021. The first phase used computer simulations to develop a methodology that allowed for the reduction of a test article's longitudinal size, while maintaining a thermo-mechanical response consistent with the rail car floor assembly's end-use condition. This work conducted a series of large-scale experiments to further explore and validate that previously developed methodology.

The large-scale experimental study executed in this work consisted of four test assemblies. The first was a full-scale floor assembly tested in accordance with the National Fire Protection Association (NFPA) 130 loading and support conditions. The second was a full-scale floor assembly using proposed alternative support conditions that better represent the end-use application. The third test article was a reduced-scale version of the second test article designed in accordance with the previously developed size reduction methodology. The last assembly was an alternative design that was also tested according to the developed size reduction methodology. The two reduced-scale test articles were concurrently tested in the same furnace.

A series of computer simulations of the experiments were developed using the finite element (FE) method. Researchers developed the first iteration of models prior to finalizing the test article designs and the subsequent large-scale testing. The second phase of models corrected discrepancies between the idealized design and actual implementation, and made other changes based on observed behavior during the large-scale tests. Following the second phase of models, a series of small- and intermediate-scale tests were conducted to better understand the thermal and mechanical properties of the materials used in the large-scale assemblies. Upon the conclusion of those tests, a final iteration of models was developed to predict the large-scale test assembly with as high an accuracy as possible.

The first, pre-test iteration of simulations of the large-scale experiments generally resulted in an over-prediction of performance of the test articles. This was partially attributed to uncertainty in the final design of the test articles, details of how the test articles would be structurally supported, and the precise thermal and mechanical properties of some of the materials within the floor assemblies.

The second iteration of simulations developed after the large-scale testing was more accurate than the pre-test simulations because it incorporated the final design of the test articles. Additional modifications were made to the second iteration of simulations, such as changes to account for slipping between the floor topper panels and the underlying steel frames as this slippage was observed during the large-scale experiments. However, uncertainty in the properties of materials used in the composite floor topper panels created continuing differences between the experimentally observed behavior and the predicted behavior of the floor assemblies.

A series of small- and intermediate-scale thermal and mechanical experiments were conducted to obtain more accurate thermal and mechanical material model inputs for a final iteration of models. These experiments included radiant exposure of floor topper panels in a cone calorimeter, which was used in conjunction with multi-parameter optimization schemes to develop updated thermal properties for composite skin and core materials. Intermediate-scale

furnace tests on the topper panels were used to benchmark and validate the developed thermal properties while furnace tests on cross-sectional mock-ups of the full-scale rail car floor assemblies was conducted to ensure applicability to the large-scale tests. Finally, a series of small-scale mechanical tests, including tension, compression, and bending were conducted to develop updated mechanical properties of the composite topper panels.

A third and final iteration of computer simulations was developed to incorporate updated material thermal and mechanical properties into the predictions of the large-scale test article behavior. Generally, these simulations were able to capture the thermal and mechanical behavior of the large-scale test articles.

The final iteration of simulations was used to explore the sensitivity of the thermal and mechanical behavior of large-scale test articles to the size reduction methodology and possible complications of executing such fire resistance tests. This included the incidental thermal shielding at the edges of the test article when sealing the test article in the furnace. It was found that the mechanical response of reduced-scale test articles is sensitive to such shielding as structural members are located at the edges of the assembly. Incidentally, shielding just 102 mm (4 in.) of the transverse ends of a reduced-scale test article can decrease the resulting deformations and increase failure times by over 80 percent. Similarly, the incidental confinement of a test article due to the physical support structure can cause localized stress and strain increases in critical structural members, especially in the transverse direction. This can cause premature structural failure of test articles.

Overall, the experimental data gathered in this effort did not contradict the previously developed methodology for reducing the physical size of fire resistance test articles. Combined with the insights gained from the high-fidelity computer simulations of the large-scale tests, this research highlighted sensitivities of reduced-scale testing to logistical challenges in the implementation of test methods.

1. Introduction

The Federal Railroad Administration (FRA) has a defined mission to enable the safe, reliable, and efficient movement of people and goods throughout the United States. To this end, FRA has established fire safety regulations for the design and operation of new and existing passenger trains in the U.S., and these regulations have been published in Title 49 Code of Federal Regulations (CFR) Part 238. In the rule-making process, for 49 CFR Part 238 that was issued in 2002, there were technical comments made on the large-scale floor assembly fire resistance testing. In particular, comments were made relating to the potential of reducing the size of the test article needed in large-scale fire testing to make testing more cost-effective. This report details the results of continued research to address this comment. FRA provided funding for this research in collaboration with the Volpe National Transportation Systems Center, while Jensen Hughes conducted the research between October 2018 and June 2021.

Previous research conducted as part of this effort used the development of computer simulations of rail car floor assemblies to develop a methodology for reducing the physical size of the rail car floor assembly. The current research aimed to conduct a series of large-scale experiments and develop the corresponding computer models to validate the methodology that was previously developed and explore the sensitivity of the methodology to different floor assemblies.

A summary of the series of tasks performed to address these requirements are as follows:

- The design of a large-scale experimental test series to validate the findings of the computer models conducted as part of the previous research. This involved the design and construction of two full-scale test articles which would be tested individually and two reduced-scale test articles which could be concurrently tested in the same furnace. Three of the four total test articles were based on the exemplar floor assembly geometry analyzed in the previous research which consisted of primary structural side sills with a secondary transverse and longitudinal structure. The last floor assembly represented an alternative structural design consisting of a primary central sill with a secondary transverse structure.

- Researchers developed pre-test computer simulations to predict the expected behavior of the test assemblies. These models would be based solely on material models from the engineering literature and theoretical test details such as support conditions. The pre-test models were wholly uninfluenced by the results of the large-scale testing program.

- The execution of the three large-scale furnace tests took place. This included individual tests of the two full-scale test assemblies and the concurrent test of the reduced-scale test assemblies. Researchers conducted these experiments over the course of 5 days in May 2019.

- The pre-test computer simulations were modified to account for discrepancies between the theoretical pre-test models and the actual large-scale tests. This included changes such as application of the measured thermal exposure and modification of the contact model between the assembly topper panels and underlying frame based on observations of the large-scale tests.

- Development and execution of small- and intermediate-scale experiments to increase the accuracy of thermal and mechanical material models used in the computer simulations

were done. This included thermal and mechanical property testing of the materials in the floor assembly topper panels as well as validation testing of updated material models using an intermediate-scale furnace.

- Researchers identified the need for further modification of the pre-test computer simulations to account for updated thermal and mechanical material models. The updated models were then used to explore the sensitivity of the thermo-mechanical response and scaling methodology to inconsistencies and difficulties in implementing reduced-scale test articles for fire performance testing.

1.1 Background

Rail car floor assemblies are currently required by the National Fire Protection Association (NFPA) 130 and 49 CFR Part 238 to undergo a large-scale furnace test to demonstrate their fire resistance in accordance with ASTM E119, including structural integrity and limited heat transmission. ASTM E119 requires test articles to be exposed to a prescribed time-temperature curve using a furnace. While ASTM E119 provides test article size requirements, these are superseded by requirements provided within NFPA 130 which state that the test article must include the entire width of the rail car and a minimum of 3.7 m (12 ft) of a rail car length. In addition, samples must contain one of each type of penetration present in the entire rail car construction.

The current size test article requires a large-scale test to be performed to evaluate a single section of the floor. With modern rail car floor assemblies including structural detail that may vary along the length, this may result in testing multiple floor assemblies to demonstrate the adequacy of the entire rail car to meet the required fire resistance. Reducing the test assembly size would potentially allow for testing in a smaller furnace or multiple test articles to be exposed at the same time in a larger furnace.

Previous research by Kapahi et al. (2018) from this program investigated the feasibility of reducing a full-scale fire resistance test article. This previous research was limited to numerical simulation of floor assemblies and did not include physical experimentation to explore and validate the proposed methods and results. It was first found that supporting the test article by the primary structural elements, which was the side sills for the considered exemplar assembly, resulted in a mechanical response more representative of the end-use application in a full rail car. With that updated support condition, it was found that the longitudinal size of the fire resistance test article could be reduced to a single repeating structural cell and still produce an equivalent thermal and structural response when exposed to an ASTM E119 test. Comparison of such a reduced-scale and full-scale test assembly response is shown in Figure 1.

This research included large-scale experiments to further explore and validate the size reduction methodology proposed by Kapahi et al. (2018) in the previous research.

4
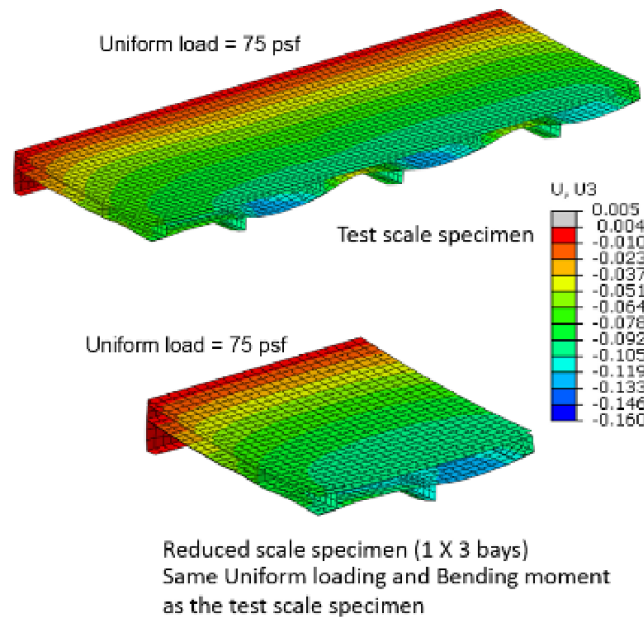
Figure 1. Predicted deflection response of full-scale and reduced-scale test articles using methodology previously developed by Kapahi et al. (2018)

1.2 Objectives

The primary objectives of this research were to validate the previously developed scaling methodology and identify potential difficulties with implementing fire resistance testing on reduced-scale test articles.

1.3 Overall Approach

The objectives were accomplished through a combined experimental and numerical simulation effort to understand and validate the relevant physics involved in reducing the physical scale of test articles for fire resistance testing. The experimental program consisted of a series of three large-scale tests in which four large-scale test articles were exposed to the ASTM E119 time-temperature curve and mechanical loads detailed in NFPA 130. An additional series of small- and intermediate-scale experiments were conducted to validate the thermal and mechanical material models being used to understand the behavior observed in the large-scale tests.

All the simulations discussed in this report were conducted using Abaqus 2017. Abaqus is a commercially available finite element (FE) software package including the Abaqus FE solver and the Abaqus "Complete Abaqus Environment" (CAE) pre-processor and post-processor. The Abaqus solver is capable of applying the FE method to a non-rectilinear meshed domain including non-linear effects from geometry and materials. This includes sequentially and simultaneously coupled thermal and mechanical evaluations of a meshed geometry, including temperature-dependent material properties. Many of the thermal models discussed in the report are simultaneous-coupled, also called fully-coupled, thermal-mechanical models to capture the effects of degradation of fiberglass insulation at elevated temperature. Temperature predictions of the floor assembly structural elements and floor panel are then sequentially coupled to the mechanical analysis to predict the structural response of the floor assembly. This process is

5

further documented in a previously published FRA report [1]. Material properties for all models discussed in this report are provided in Appendix A.

1.4   Scope

The scope of this effort was limited to the testing and simulation of the exemplar floor assembly design and the single alternative assembly design. Much of the experimentation and simulation is focused on the exemplar floor assembly. However, a wide variety of possible railcar floor assembly structures is possible, and the implementation and validation of the previously developed scaling methodology on a wider array of floor assembly designs is not addressed in this report.

1.5   Organization of Report

This report is divided into several primary sections based on the overall tasks conducted as part of this research. Section 2 provides additional details on the floor assembly test articles considered in this research. Section 3 contains details about the execution of the large-scale test series and the measured thermal and mechanical response of the test articles. Sections 4 and 5 discuss the development of the pre-test models, called the Phase I models, as well as the modifications made to address discrepancies between the pre-test models and actual testing conditions in the updated models, called the Phase II models. Section 6 provides details of the small- and intermediate-scale material and section testing conducted to develop and validate updated material models for the floor assemblies. Section 7 contains the simulations updated with the developed material models, called the Phase III models, and a comparison to the experimental results and previous models. Section 8 includes a discussion on the impact and sensitivity of inputs and inconsistencies of experiments on the full- and reduced-scale floor assemblies. Section 9 provides details on the essential findings and future recommended steps. Appendix A contains additional information on the simulation material models, and Appendix B shows illustrations and images of test article drawings.

2. Floor Assembly Description

Three different floor assembly designs were tested in the large-scale furnace at the Southwest Research Institute (SwRI). The first design was a full-scale floor assembly meeting the dimensional requirements of NFPA 130. Two full-scale assemblies were tested. The first full-scale assembly was supported on the transverse ends in accordance with NFPA 130, the second full-scale assembly was supported on the longitudinal ends according to the proposed alternative conditions. The second tested design was a reduced-scale assembly of the same general design as the full-scale assemblies. The last assembly was an alternative structural design. A detailed description of each of the assemblies is provided in the following sections. Appendix B contains drawings of the test articles can be found in Appendix B.

2.1 Test Article 1: Full-Scale Transverse Supports

The first test article was a full-scale floor assembly tested in accordance with NFPA 130. The floor assembly consisted of a ply-metal composite floor panel on a carbon steel frame, as shown in Figure 2. The ply-metal composite consisted of a 19 mm (0.75 in.) maple ply core sandwiched between 1.4 mm (0.55 in.) thick steel skins. The assembly contained three ply-metal panels along the longitudinal span. The panels were mounted to the frame using screws at approximately 200 mm (8 in.) spacing.

The steel frame consisted of interior transverse and longitudinal channels between primary structural side sills. The side sills were 235 mm (9.25 in.) tall channels with a 76 mm (3 in.) leg at the bottom and a 38 mm (1.5 in.) leg at the top. The interior structural channels were 101 mm (4 in.) wide and 76 mm (3 in.) tall. There were also 38 mm (1.5 in.) by 13 mm (0.5 in.) stiffeners directly above the lower transverse channel stiffeners. All the stiffeners were fabricated from 3 mm (0.12 in.) sheet steel. The structural frame contained three nominal repetitions at a 1.2 m (4 ft.) spacing. Additional transverse channels were placed at the bottom ends of the side sills to prevent localized buckling at the support locations. A steel belly pan made of a 3 mm (0.125 in.) sheet spanned the entire assembly. The team placed 76 mm (3 in.) of spun fiberglass insulation between the belly pan and the ply-metal panels.
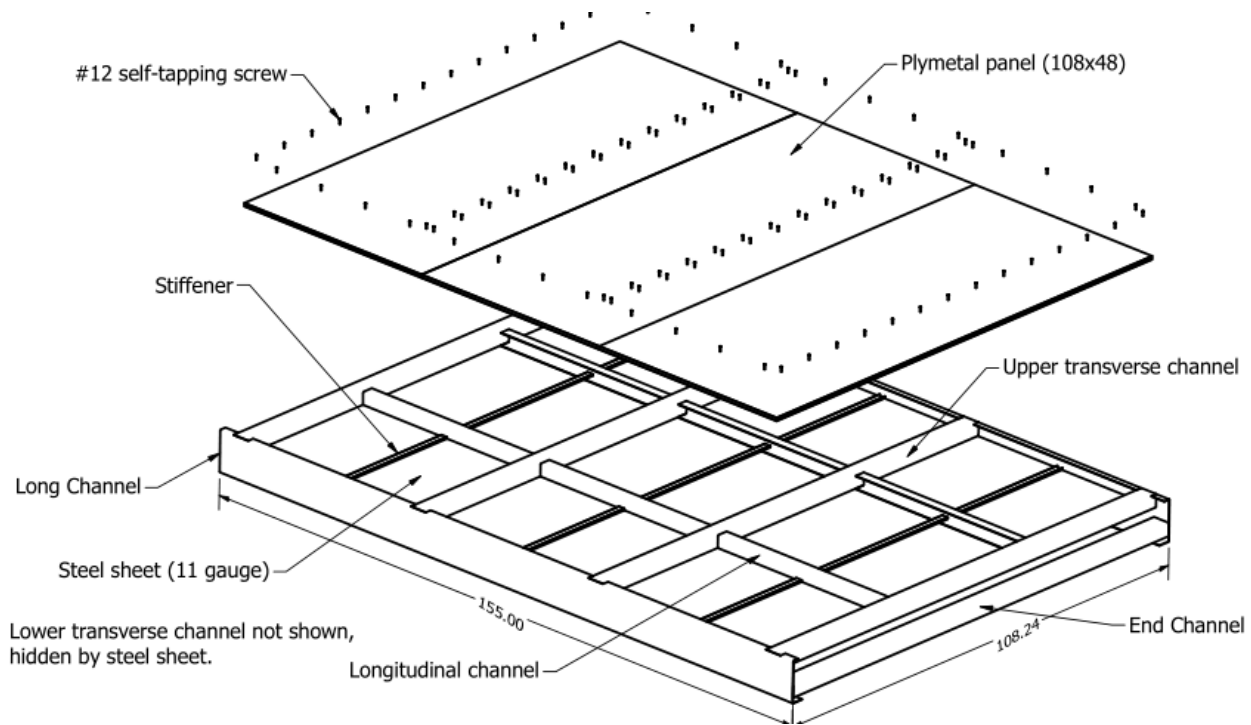
Figure 2. Schematic of full-scale exemplar test article

2.2 Test Article 2: Full-Scale Longitudinal Supports

The second test article was nominally identical to the first test article. The only design difference between the two test articles is that the second test article did not have the additional transverse channels at the ends of the side sills because it was not being supported exclusively at these locations. Instead the second test article was supported along the entire length of the side sill. This required a constructed support as described in Section 3.2.

2.3 Test Article 3a: Reduced Scale Longitudinal Supports

The third test article was a reduced-scale version of the full-scale test articles described in the previous two sections. A diagram of the test article is shown in Figure 3. The assembly consisted of a ply-metal floor panel of the same cross-sectional dimensions as the full-scale test articles described in the previous sections. The reduced-scale test article only contained a single ply-metal panel. The panel was supported by a carbon steel frame with the same layout as described in the full-scale test articles. While the full-scale test articles contained three nominal structural repetitions, the reduced scale test article only contained one repetition.
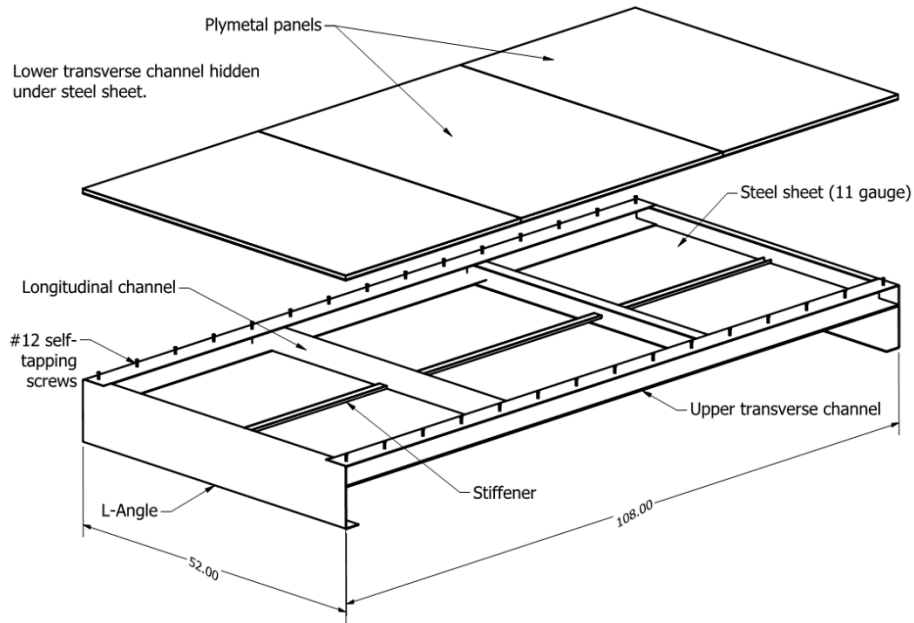
Figure 3. Schematic of reduced-scale exemplar test article

2.4 Test Article 3b: Reduced Scale Alternative Design

The final test article to undergo testing at SwRI was of a structurally different concept. This test article consisted of a large sill that ran longitudinally down the center of the test article. This sill was built of a 0.32 m (12.5 in) wide, 6.35 mm (0.25 in) thick base plate with two 0.2 m x 0.83 m x 6.35 mm (8 in x 3.25 in x 0.25 in) channels welded to the top, as shown in Figure 4. Above the sill was a 1.6 mm (0.06 in) steel sheet that served as the belly pan. The interior structure consisted of 0.095 m x 0.28 m x 1.6 mm (3.75 in x 1.1 in x 0.06 in) transverse Z-channels spaced 0.65 m (25.8 in) apart. 101 mm (4 in) of Spin-Glas TC fiberglass insulation was placed in the voids between the interior structural elements. The longitudinal ends of the floor assembly were capped with a 0.95 m x 0.76 m x 6.35 mm (3.75 in x 4 in x 0.25 in) channel. The floor assembly was topped with a 19 mm (0.75 in) thick fiber reinforced polymer (FRP)/Balsa panel consisting of 3 mm (0.125 in) glass fiber reinforced phenolic resin skins with a low-density end-grain balsa core.
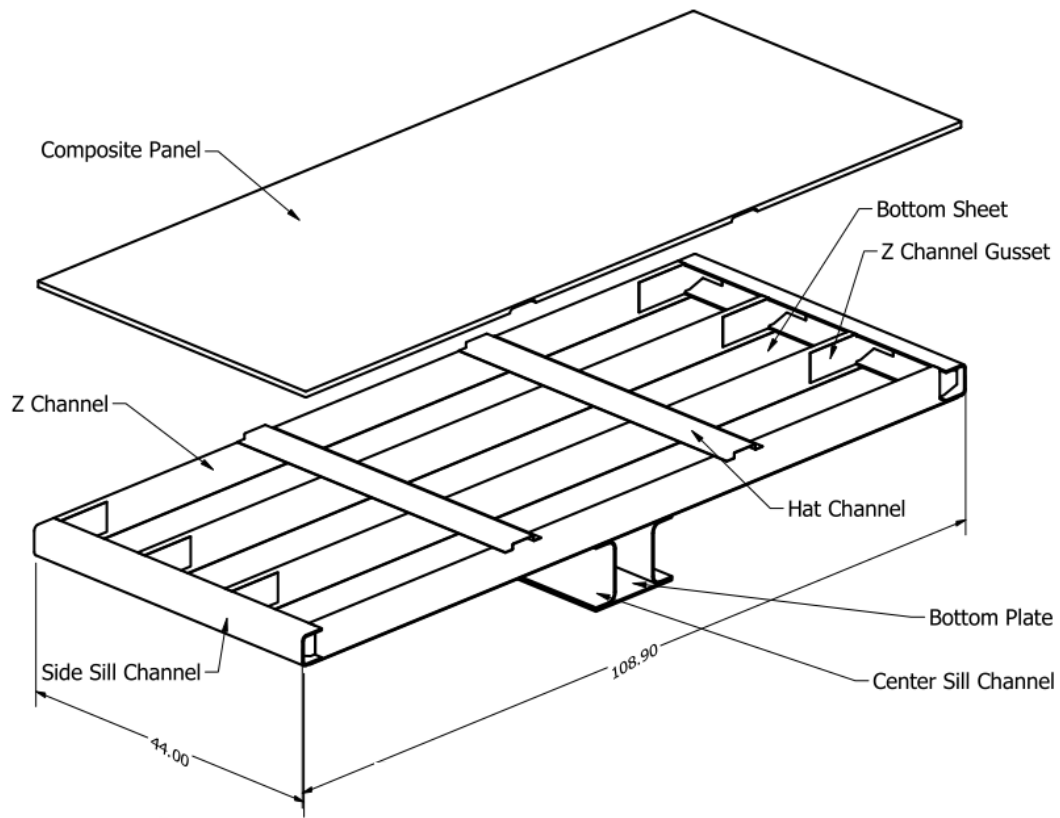
Figure 4. Schematic of reduced-scale alternative design test article

3. Large-Scale Testing

Subsequent to the pre-test modeling, the floor assemblies were manufactured and tested in the large-scale furnace at SwRI. The following sections describe the large-scale test methods and results and compare them to the pre-test modeling results for each floor assembly.

3.1 Test Article 1: Full-Scale Transverse Supports

Test Article 1 was tested in accordance with NFPA 130 and ASTM E119. The test article was supported by the furnace walls at the transverse ends of the test article. A live load equivalent to 75 psf was applied to the top of the test article across 12 locations using 6 hydraulic jacks. The resulted in a total load of 33.6 kN (7,560 lbs) on the test article. The loading locations are shown in Figure 5 and were 305 mm (12 in) long by 128 mm (5 in) wide. The deflection response of the test sample was measured at three locations using string potentiometers. The thermal response of the unexposed surface was measured in nine locations. The temperature of the bottom of the ply-metal panel, top of the fiberglass insulation, mid-depth of the insulation, and belly pan were measured at two locations. Temperature of an internal transverse channel web and top flange were measured at two locations. All the measurement locations are shown in Figure 5, and note that the test article is supported at the top and bottom edges. The drawing is not to scale, and all the dimensions are in inches.
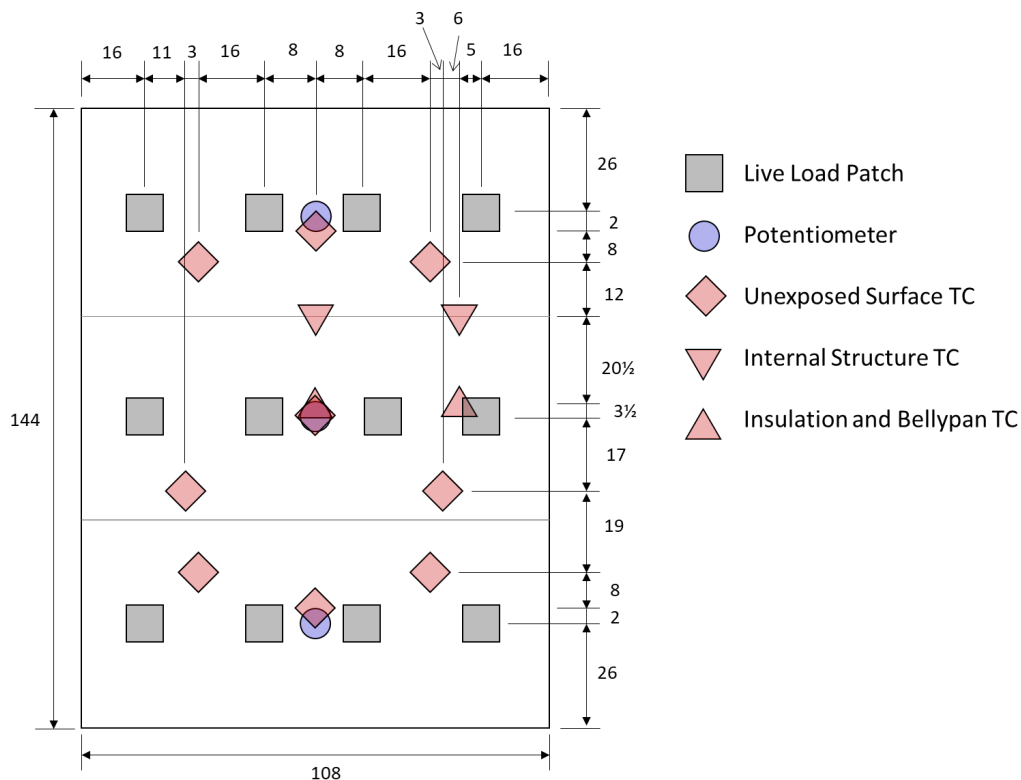
Figure 5. Location of loading and measurement points for Test Article 1

The measured thermal and structural response of Test Article 1 under the ASTM E119 loading and exposure is shown in Figure 6. The temperature at the unexposed surface was well below the

ASTM E119 limits as the exposure time approached 30 minutes. However, the deflection rates of the test article were increasing, which prompted termination of the test just prior to 30 minutes.

Unexposed surface temperatures were below 70 °C at the time of test termination. This is well below the necessary ASTM E119 temperature requirements for the unexposed surface. Temperature measured at two locations on the bottom of the ply-metal panel were similar and reached 400 °C at the end of the test. Temperature measurements of the fiberglass insulation resulted in variations of approximately 60 °C between measurement locations both on the top and at the mid-height of the insulation. Temperature measurements of the internal structural elements were consistent between locations and yielded measurements up to 600 °C.

The structural response floor assembly was reasonably symmetric based on the deflection measurements. The deflection evolution consisted of an initial rapid deflection period of approximately 10 minutes. This is caused by the rapid initial heating rate of the ASTM E119 temperature curve which results in thermal gradients through the thickness of the assembly creating thermally induced bending moments. The deflection rate slows between 10 and 20 minutes of exposure as the thermal gradients reduce. Beyond 20 minutes, a tertiary regime occurs where the deflection rate increases upon the onset of failure. This is due to the increasing temperature of the structural elements through the entire assembly causing reduced stiffness, strength, and an increase in creep strains.
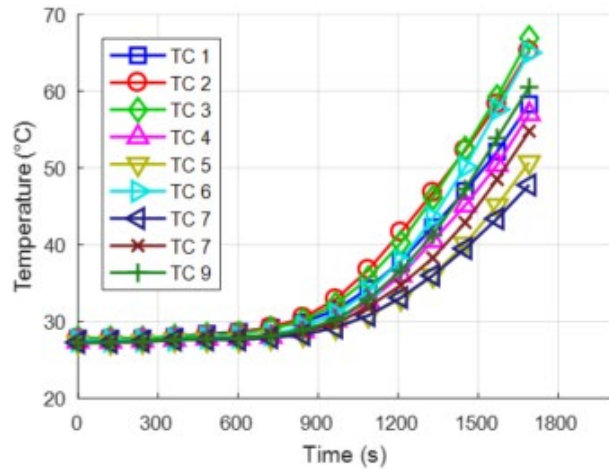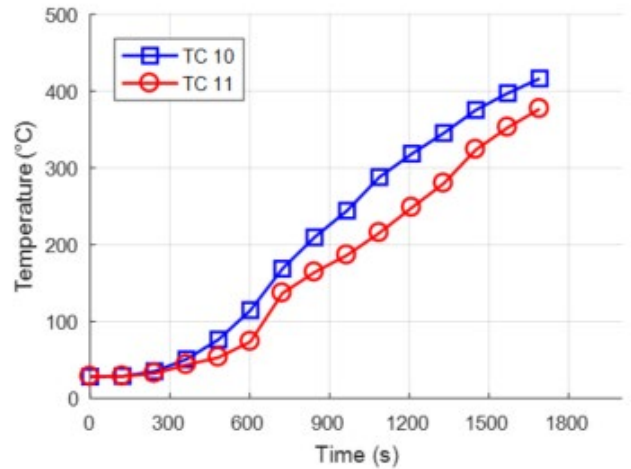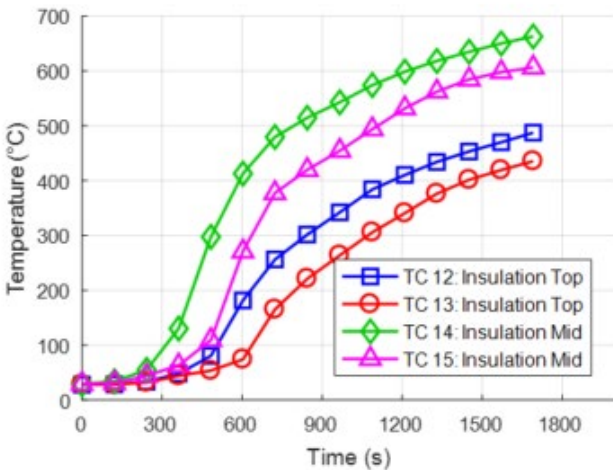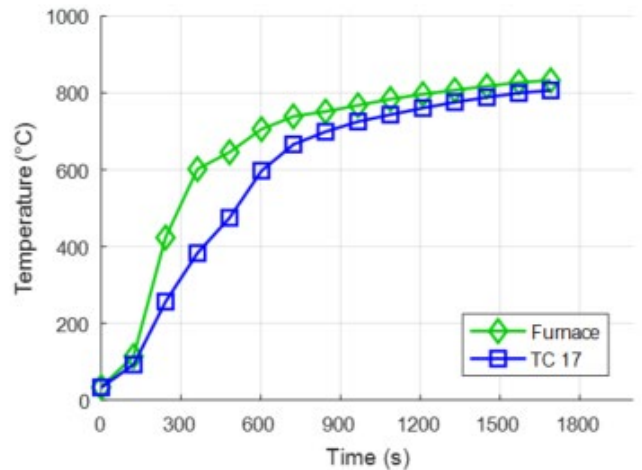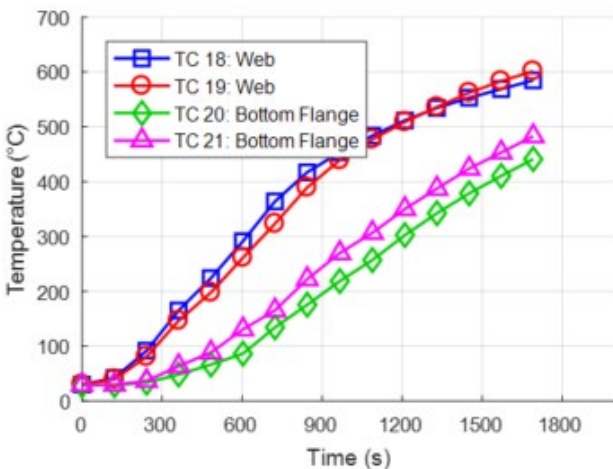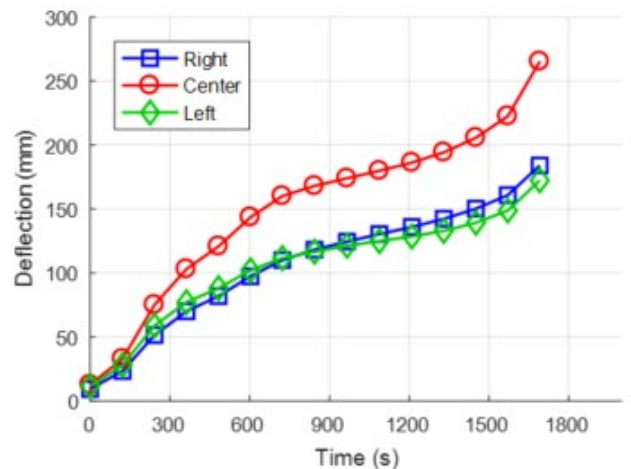
Figure 6. Test results for Test Article 1. (a) Unexposed surface temperature (b) ply-metal bottom temperature (c) insulation top and middle temperature (d) belly pan and furnace temperature (e) internal structural channel temperature (f) test article deflection

13

3.2 Test Article 2: Full-Scale Longitudinal Supports

Test Article 2 was of the same nominal design as Test Article 1 as described in Section 2.2 and many test parameters are the same as those for Test Article 1. Test Article 2 had the same 75 psf applied live load as Test Article 1. However, the exact load patch locations for Test Article 2 was different from Test Article 1 because it was oriented differently in the test frame. Test Article 2 was supported by the side sills using a built-up steel frame that attached to the furnace walls and overhead support beams. An inadvertent consequence of this support configuration was the confinement of the test article in the transverse direction as seen in Figure 7. This confinement impacted the failure behavior of the assembly as discussed below. The location of the deflection measurements was also different because Test Article 2 was supported by the side sills on the longitudinal ends. Unexposed surface temperature was measured at nine locations like Test Article 1 and internal and belly pan temperature measurements were also obtained. The location of the load patches and measurements is shown in Figure 8, and the test article is supported at top and bottom edges. The drawing is not to scale and all dimensions are in inches.

Figure 7. Test Article 2 within the built-up steel support frame
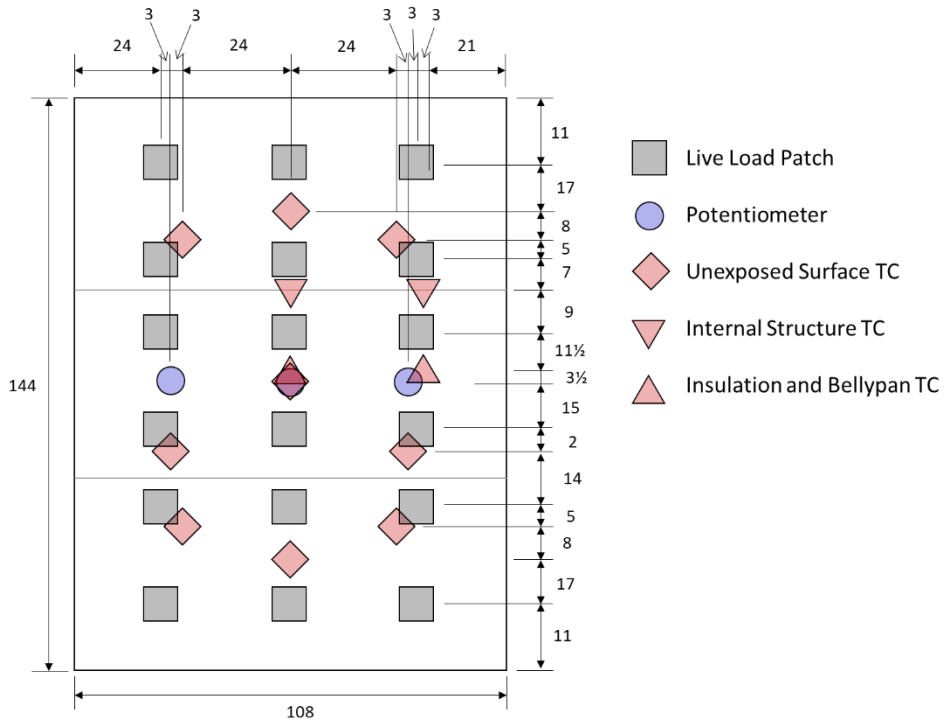
Figure 8. Location of loading and measurement points for Test Article 1

The measured thermal and structural response of Test Article 2 is shown in Figure 9. Test Article 2 was exposed for a duration of 45 minutes. At this point, increased deflection rates were indicative of imminent failure, and the test was terminated. This test duration was approximately 15 minutes longer than Test Article 1. This was expected as the transverse span of the test article was smaller than the longitudinal span.
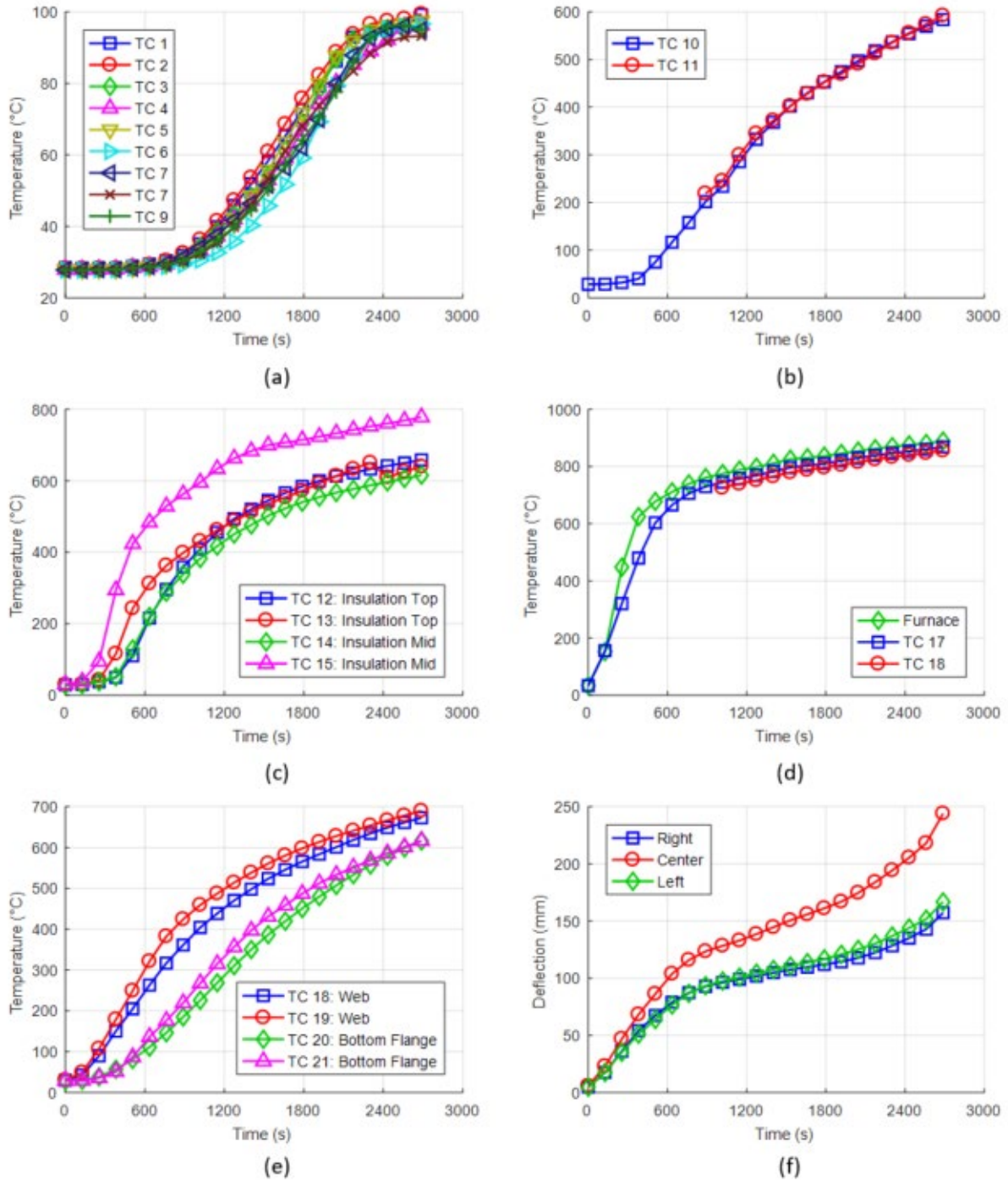
Figure 9. Test results for Test Article 2. (a) Unexposed surface temperature (b) ply-metal bottom temperature (c) insulation top and middle temperature (d) belly pan and furnace temperature (e) internal structural channel temperature (f) test article deflection

The measured unexposed surface temperature at the end of the 45-minute exposure was approximately 100 °C with some variation between measurement locations. There was an observed pause in the heating rate of the unexposed surface temperature at 100 °C. This is caused by the moisture within the plywood core of the ply-metal composite panel evaporating

16

into steam. This effect of moisture content was not considered in the Phase I models as the moisture content was not known before the test articles were manufactured and neglecting moisture content effects provides conservative estimates of temperature. The measured temperature at the bottom of the ply-metal was 600 °C at the end of the experiment. At these temperatures, oxidation of the wood char begins to occur. The temperature measurements on the top of the fiberglass insulation were quite variable between the two measurement locations with temperature differences of over 150 °C. This could be the result of inconsistent performance of the fiberglass insulation at temperatures above its maximum operating temperature of 500 °C. Measured temperatures of the belly pan, and internal structural elements were consistent with those measured on Test Article 1.

The observed deflection behavior of Test Article 2 was similar to Test Article 1. There was an initial primary region of higher deflection rates followed by a secondary region reduction in deflection rate and then a tertiary region with an increase in deflection rate at the onset of failure. The deflection response was also nominally symmetric in the transverse direction. Failure of Test Article 2 was caused by compressive failure of the floor panels in the transverse direction near the centerline of the test article. The support configuration of the test article within the built-up steel frame generated thermally induced confinement in the transverse direction. This confinement generated compressive stresses in the transverse direction ultimately causing localized buckling of the ply-metal steel skins as seen in Figure 10.

Figure 10. Failure location of Test Article 2 by localized bucking caused by confinement after 45 minute exposure to ASTM E119 conditions

3.3   Test Article 3a: Reduced Scale Longitudinal Supports

Test Article 3a was of the same nominal design as Test Articles 1 and 2 except it only spanned 52 inches in the longitudinal direction. Like Test Article 2, Test Article 3a was supported at the longitudinal edges by the frame side sills. This support came from the same built-up steel frame that was used to support Test Article 2. However, the steel frame was set to a slightly larger span for Test 3, providing room for thermal expansion of the test articles in the transverse direction for Test 3. This resulted in a difference in failure behavior of the test article as discussed below. A live load distribution of 75 psf was applied to Test Article 3a. This resulted in a total load of 13 kN (2,925 lbs) on the test article spread across six locations. The unexposed surface temperature of Test Article 3a was measured at three locations along with the deflection

response. The temperature of the insulation and belly pan was measured at two locations and the temperature of an internal structural element was measured at one location. The location of the loading patches as well as the thermal and deflection measurements is shown in Figure 11; note that the test article is supported at left and right edges. The drawing is not to scale, and all the dimensions are in inches.
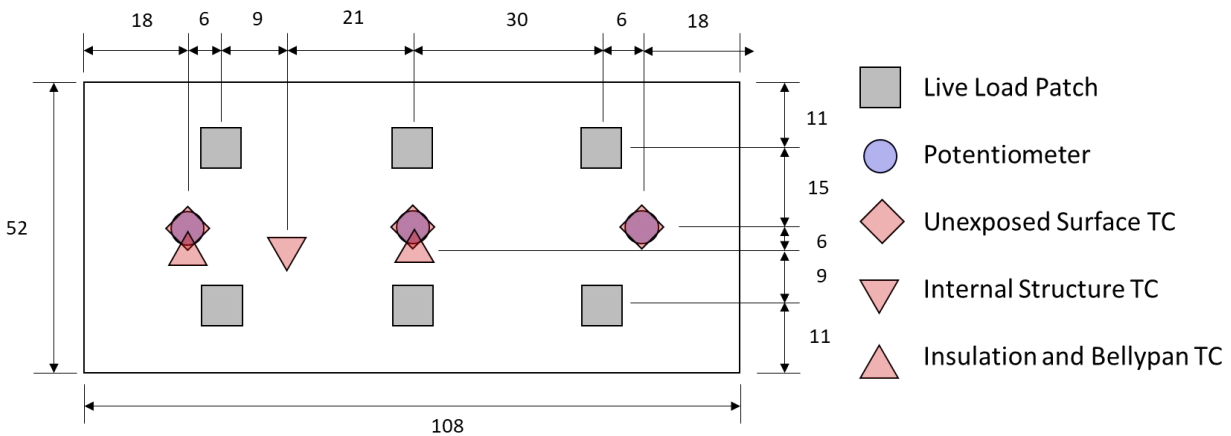
Figure 11. Location of loading and measurement points for Test Article 3a

The thermal and deflection response of Test Article 3a is provided in Figure 12. Test Article 3a was able to carry the applied live load over the full duration of the 60-minute ASTM E119 exposure conditions. However, the deflection response at the end of the 60-minute period was indicative of immanent failure. This failure time is at least 15 minutes longer than Test Article 2 which was designed to have a similar response. The lack of transverse confinement as well as incidental shielding of part of the test article cause Test Article 3a to maintain load carrying capacity longer than Test Article 2.

The unexposed surface temperature of Test Article 3a was similar to Test Articles 1 and 2. There was an initial heating period followed by a pause in heating at 100 °C due to evaporation of the moisture within the plywood core of the ply-metal panel. At 3,300 seconds, moisture evaporation had finished, and the unexposed surface temperature began to increase. The average temperature rise of the unexposed surface was 95 °C at the end of the 60-minute exposure which is less than the ASTM E119 requirement of 139 °C. Temperature at the bottom of the ply-metal panel at the end of the exposure was above 600 °C. Some variation between the two temperature measurement locations within the fiberglass insulation was observed. Again, this suggests variability in the performance of the fiberglass insulation above its maximum operating temperature of 500 °C. Temperature measurements of the belly pan and internal structural elements were consistent with measurements for Test Articles 1 and 2.

The observed structure response of Test Article 3a was similar in nature to Test Articles 1 and 2. There was an initial primary region of higher deflection rates followed by a secondary region reduction in deflection rate and then a tertiary region increase in deflection rate at the end of the exposure. Failure did not occur within the 60-minute exposure duration but the measured increase in deflection rate at the end of the test duration suggested structure failure of the test article was imminent. Like the previous test articles, the deflection behavior was observed to be symmetric across the centerline of the unsupported span.
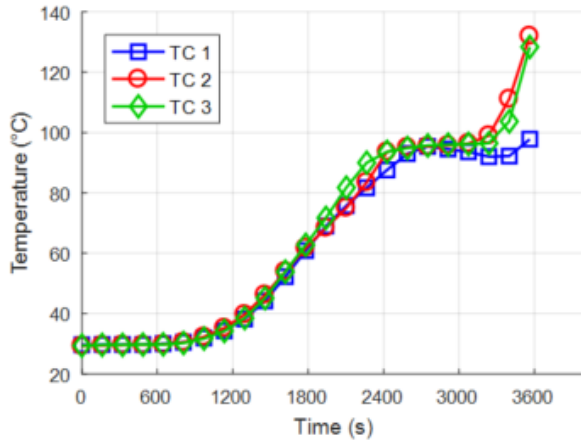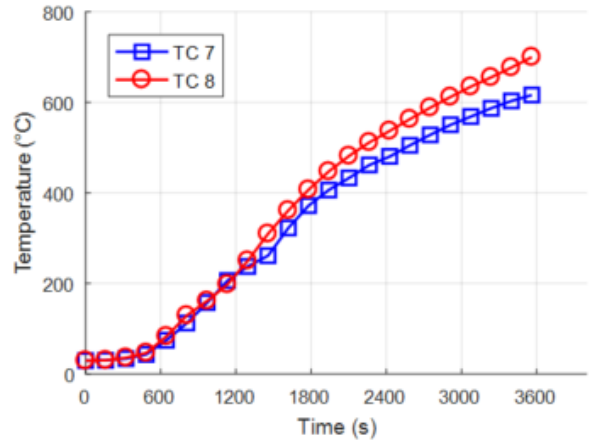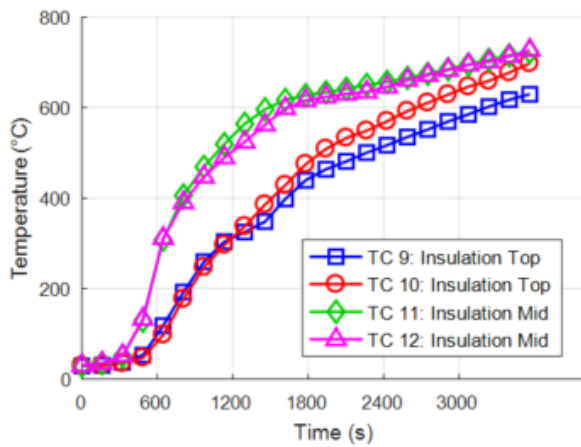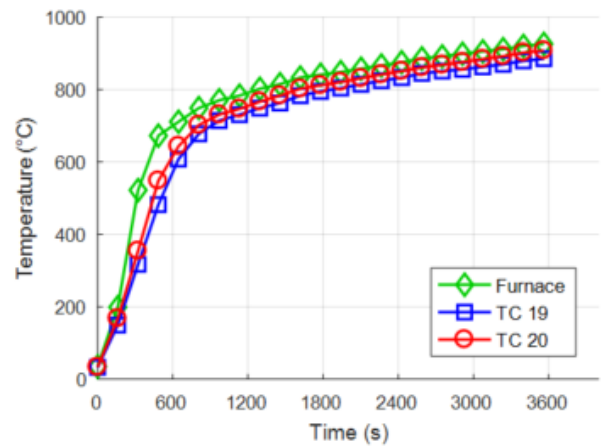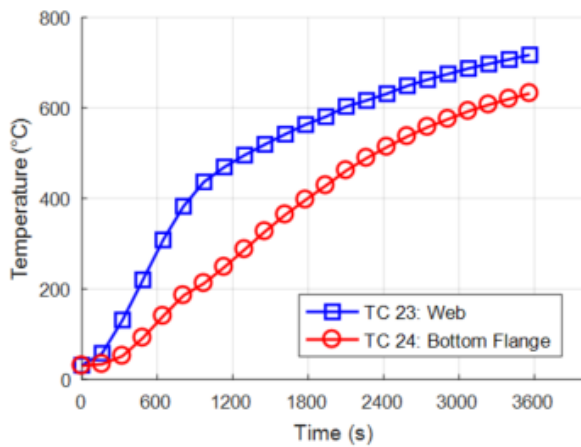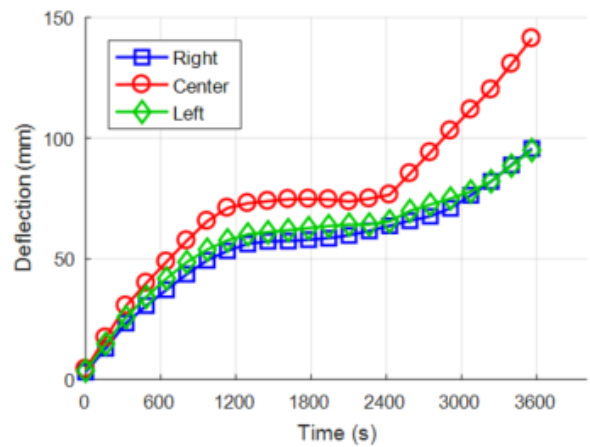
Figure 12. Test results for Test Article 3a. (a) Unexposed surface temperature (b) ply-metal bottom temperature (c) insulation top and middle temperature (d) belly pan and furnace temperature, (e) internal structural channel temperature (f) test article deflection

3.4 Test Article 3b: Reduced Scale Alternative Design

Test Article 3b was tested at the same time as Test Article 3a. The two test articles were placed above the furnace supported by the built-up steel frame. The span of the built-up frame was such to allow for expansion of the test articles in the transverse direction. Test Article 3b had an applied live load distribution of 40 psf which resulted in a total load on the assembly of 7.6 kN (1,716 lbs). This load was applied across 6 patches. The instrumentation of Test Article 3b was similar to that of Test Article 3a. Unexposed surface temperature and deflection were obtained at 3 locations along the transverse span of the test article. Insulation and belly pan temperatures were obtained near the central sill and near the longitudinal end of the test article and internal structural temperature was obtained near the center of the test article. Measurement and loading locations for Test Article 3b are provided in Figure 13. Note that the test article is supported at left and right edges. The drawing is not to scale, and all dimensions are in inches.
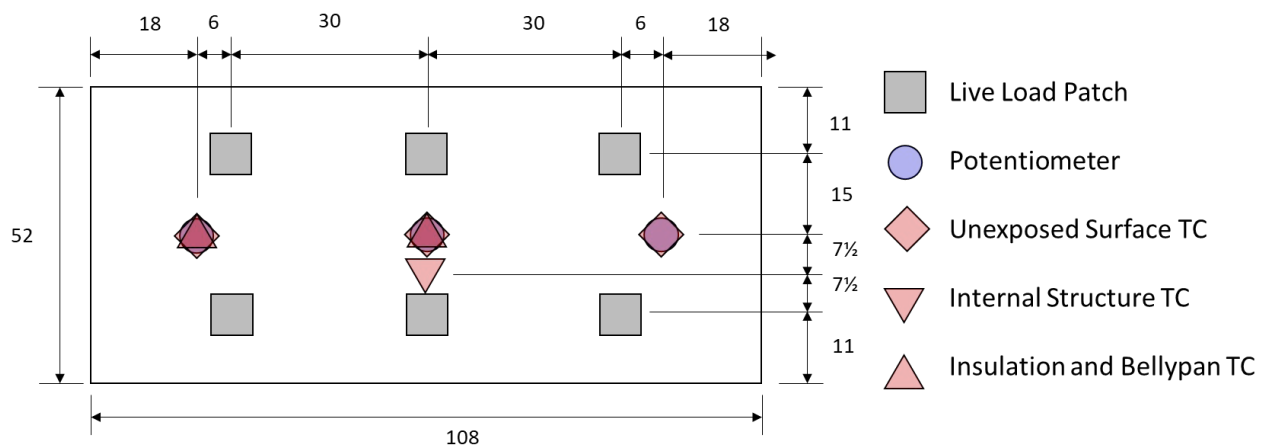
Figure 13. Location of loading and measurement points for Test Article 3b

Test Article 3b was able to maintain load carrying capacity for 50 minutes of the ASTM E119 exposure conditions. At that point, deflection rates were rapidly increasing, and load was removed from the test article to prevent a catastrophic collapse of the test article into the furnace. This failure time is higher than the current NFPA 130 required time of 30 minutes.

The measured thermal and structural response of Test Article 3b is provided in Figure 14. The average measured temperature rise of the unexposed surface was 136 °C after 30 minutes of exposure which is slightly below the ASTM E119 requirement of 139 °C. At the time of the test article failure, the average unexposed surface temperature was 398 °C. There was some difference in measured unexposed surface temperature between measurement locations. The exact source of this variability is not known. The measured temperatures at the bottom of the FRP/balsa panel were above 600 °C at the time of failure which is high enough to result in oxidation of the balsa core char. Temperature measurements of the fiberglass insulation showed significant variation between measurement locations. This is likely due to one set of measurements being taken above the central sill which lower localized heating. This can also be observed in the temperature response of the belly pan during the first 20 minutes of the experiment. TC20 which was near the central stiffener measured a lower initial heating rate than TC 19 due to the higher thermal mass of the central sill near TC 20. Temperature measurements of the internal structure were approaching 700 °C, which suggests significant degradation of steel stiffness and strength at the time of test article failure.
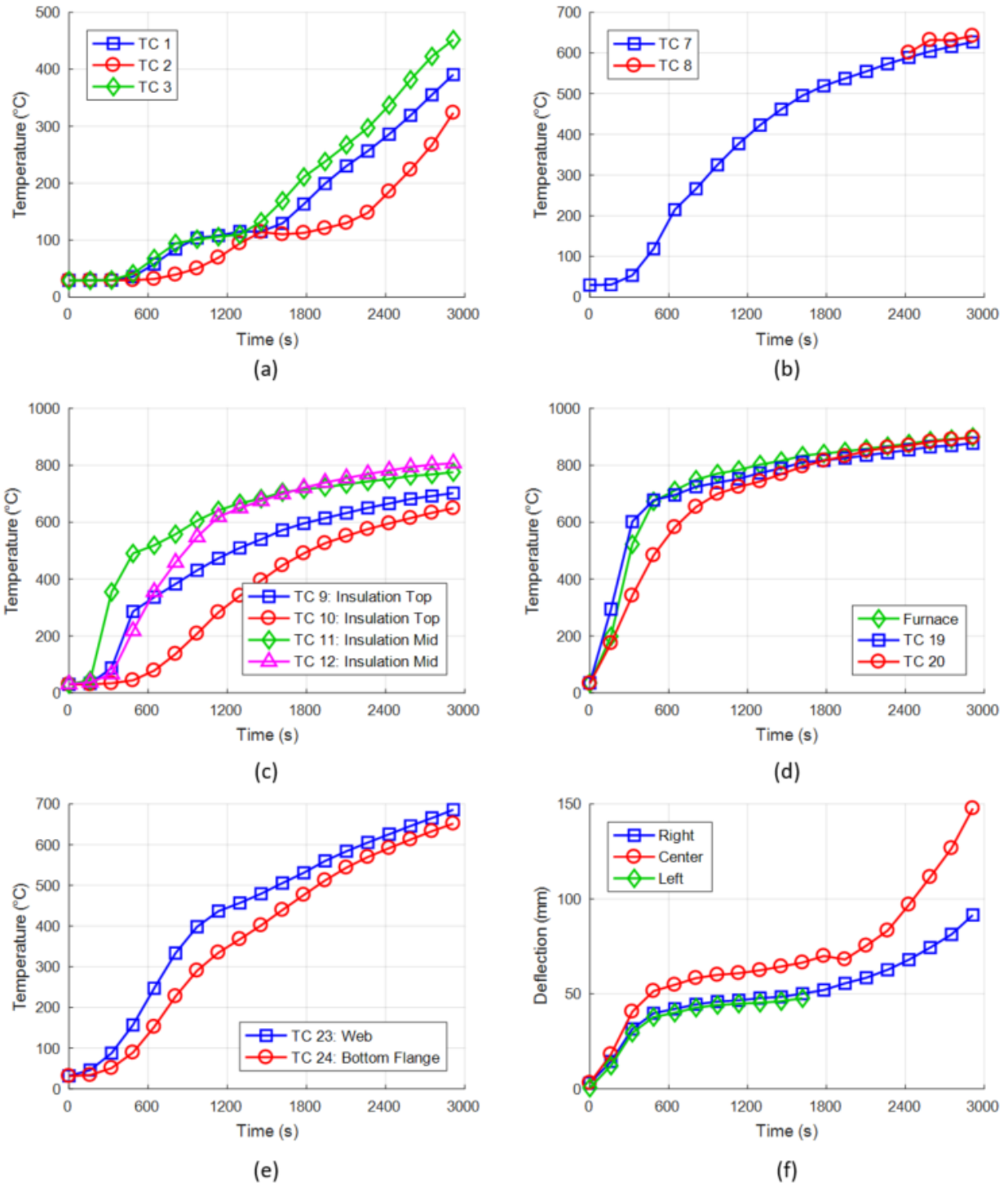
Figure 14. Test results for Test Article 3b. (a) Unexposed surface temperature (b) ply-metal bottom temperature (c) insulation top and middle temperature (d) belly pan and furnace temperature (e) internal structural channel temperature (f) test article deflection

The structural response of Test Article 3b was similar to other test articles with primary, secondary, and tertiary deflection phases before the occurrence of failure after 50 minutes of exposure.

21

3.5 Comparison of Test Article Performance

The thermal performance of Test Articles 1, 2, and 3a was expected to be similar in the ASTM E119 tests according to pre-test modeling shown in Section 1.2. A comparison of the measured thermal performance for each of these tests is provided in Figure 15. The measured thermal performance was generally similar between tests at most of the measurement locations. The largest discrepancy between tests was the insulation measurements both at the top surface and in the middle of the thickness. The temperature at the top surface of the insulation of Test Article 2 was consistently 100–150 °C higher than the other tests. This led to slightly higher temperatures at the bottom surface of the ply-metal panel for Test Article 2 as well. Temperature measurements of the insulation also exhibited the highest variability between measurement locations in the same experiment.

The structural response of Test Articles 1 and 2 was not expected to be similar. The structural span of Test Article 2, 2.74 m (108 in.), was smaller than Test Article 1, 3.66 m (144 in.). This reduced span was expected to result in a higher fire resistance time for Test Article 2. The result may have been different if Test Article 1 was also supported by the transverse stiffeners at the transverse ends of the test article as allowed by NFPA 130. However, Test Article 1 was only supported by the side sills in the corners of the test article.

Test Articles 2 and 3a were expected to have similar structural performance based on pre-test modeling. This was not observed during the experiments as seen in Figure 16. Test Article 2 experiences high amounts of deformation and loss of structural stability after 45 minutes whereas Test Article 3a sustained the applied load for the 60-minute test duration. There are two primary contributors to this difference in behavior that were not accounted for in the pre-test models. The first is accidental shielding of the transverse ends of the test articles when sealing the articles in the furnace. This is shown in Figure 17. Note that shielding of left and right ends of the test article by ceramic fiber insulation is in effort to seal the furnace. The second contributor was transverse confinement of Test Article 2 by the steel support frame. The impact of these phenomena was numerically explored and is further discussed in Sections 5.2 and 5.3 of this report.
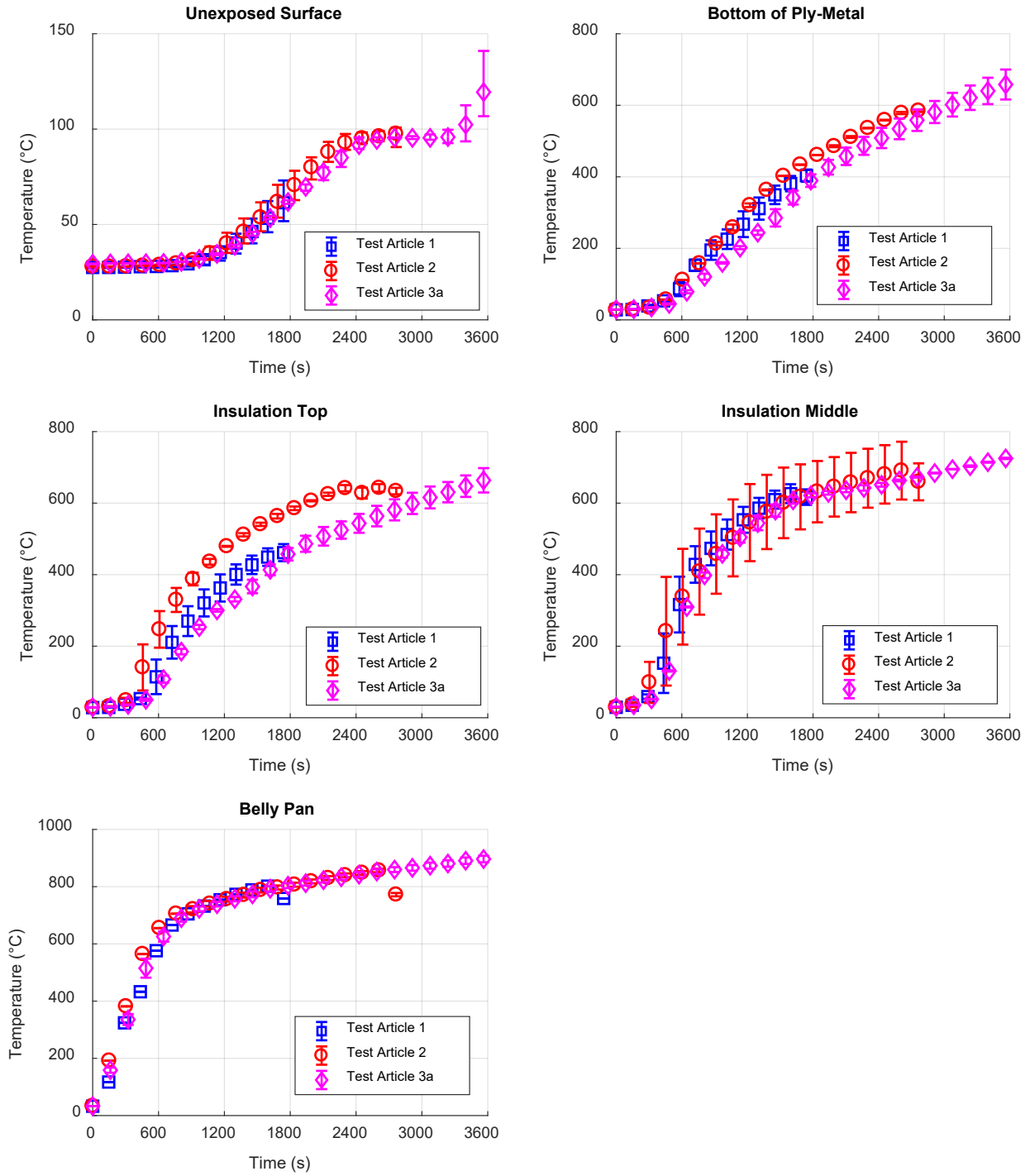
Figure 15. Comparison of the thermal response of Test Articles 1, 2, and 3a under ASTM E119 furnace exposure
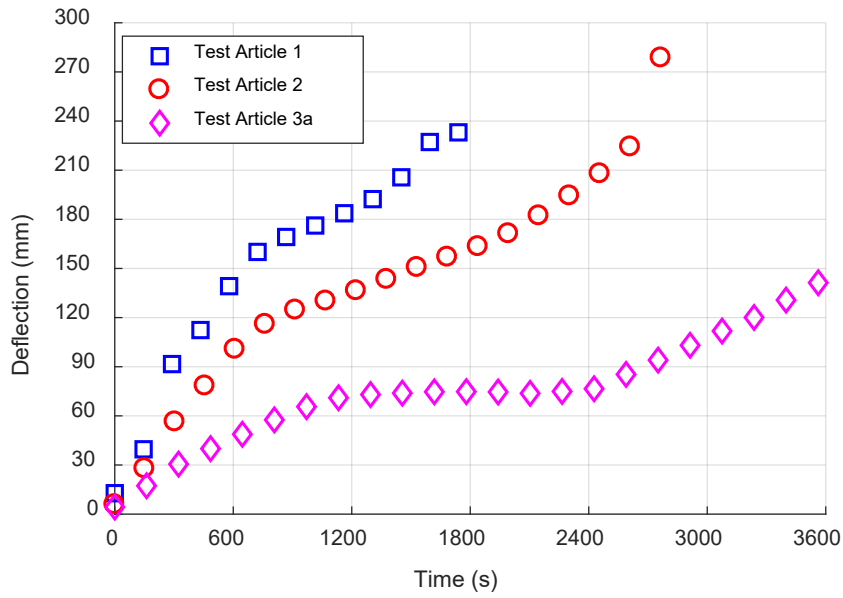
Figure 16. Comparison of structural response at the center of Test Articles 1, 2, and 3a under ASTM E119 exposure and loading
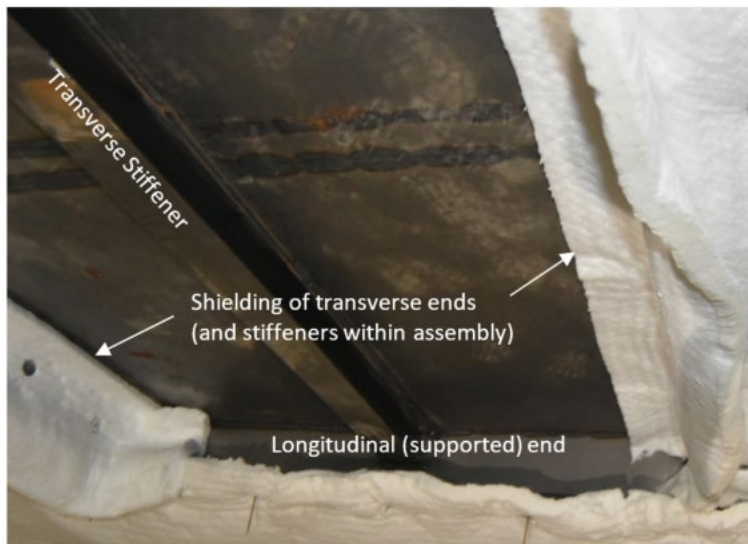
Figure 17. Exposed surface of Test Article 3a mounted in furnace prior to testing

4. Pre-Test Modeling (Phase I Models)

The Phase I simulations of the assemblies were developed before the physical assemblies were manufactured and tested. These models were developed based on the intended design and testing method for each of the assemblies. This section discusses some discrepancies between these pre-test models and as-built manufactured test article assemblies. The following sections summarize the development and results of the pre-test modeling effort.

4.1 Test Article 1: Full-Scale Transverse Supports

Figure 18 shows the model geometry for the Phase I simulation of Test Article 1. Note that only half of the test assembly is shown to reveal the internal structure. The model included the carbon steel framing members, belly pan, ply-metal composite panel, and internal fiberglass insulation. Note that the fiberglass insulation was not included in the mechanical analysis of the test article as it only contributes to the thermal performance of the floor assembly. The test article was modeled as being supported from the transverse ends of the side sills as well as the transverse channels at the transverse ends of the test article. No confinement of the test article was modeled as described in NFPA 130.

Temperature dependent thermal properties of steel from EN 1993-1-2 [2] were used in the thermal model. Temperature dependent stiffness and strength reductions were also obtained from EN 1993-1-2. Effective temperature dependent thermal properties of plywood were calculated from Fateh et al. (2014). Temperature dependent thermal properties of spun fiberglass insulation were obtained from manufacturer data for temperatures up to 500 °C. Thermal properties above 500 °C were extrapolated and a physical degradation model was developed that captured contraction of the insulation and the subsequent impact on thermal performance. The degradation model featured a linear shrinking rate of the insulation in the through-thickness direction of 0.1%/°C that began at 500 °C. Radiation exchange was calculated within the cavity that formed above the degraded insulation.
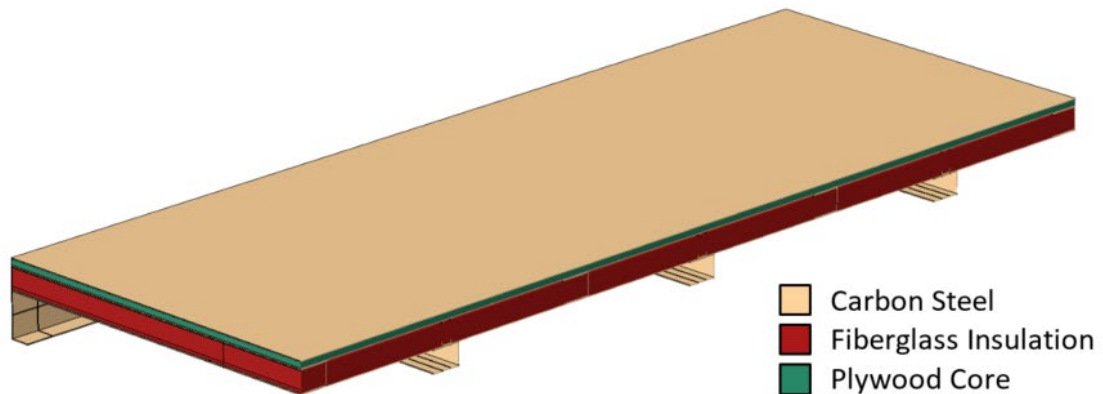
Figure 18. Phase I model geometry for Test Articles 1 and 2

All the Phase I models exposed the test articles to the idealized ASTM E119 time-temperature curve shown in Figure 19 from underneath. Exposure conditions were represented using convection and radiation. A convection heat transfer coefficient of 25 W/m²K was used on exposed surfaces which is recommended by EN 1991-1-2 [4] for furnace exposure simulations.

The exposed steel surface emissivity was assumed to be 0.7 which is the value recommended by EN 1993-1-2 [2]. Thermal losses from the top surface were also included in the models. These losses were represented with a convection heat transfer coefficient of 4 W/m²K as recommended by EN 1991-1-2 [4] and a steel surface emissivity of 0.7.
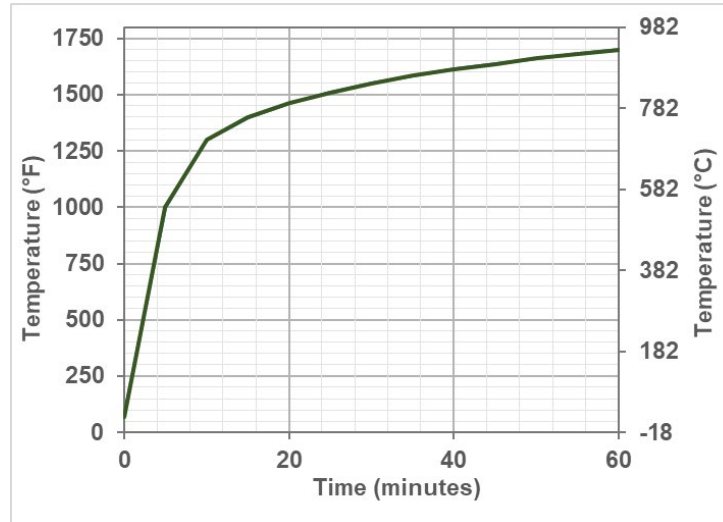
Figure 19. ASTM E119 time-temperature curved applied to exposed surfaces in Phase I railcar floor models

The predicted thermal response of Test Article 1 is provided in Figure 20 while the predicted structural response is provided in Figure 21. The unexposed surface temperature was predicted to reach a maximum of 100 °C within the 30-minute exposure duration currently required by NFPA 130. The predicted temperature of the bottom surface of the ply-metal agreed well with experimental data. However, the temperature at the top of the insulation was over-predicted. This suggests that the radiation heat transfer between the insulation and ply-metal was slightly under-predicted to compensate. The over-prediction of temperature at the top of the insulation also suggests that the insulation did not degrade as quickly as expected from the insulation degradation model. Temperature predictions of the belly pan agree well with experimental measurements suggesting the appropriate model input values for the convective and radiative boundary conditions on the exposed surface. Temperatures of the internal transverse stiffener top flange were well predicted but the web temperature was under-predicted, particularly for the second half of the exposure.

Test Article 1 was predicted to maintain structural stability for the 30-minute exposure duration with a center deflection of 200 mm at the end of the exposure. In actuality, the test article experienced loss of load carrying capability just prior to the 30-minute requirement. The deflection is also under-predicted over the entire duration of the experiment. This can be attributed to the shorter overall span modeled in the Phase I and possibly attributed to the lower inner stiffener temperatures predicted by the model.
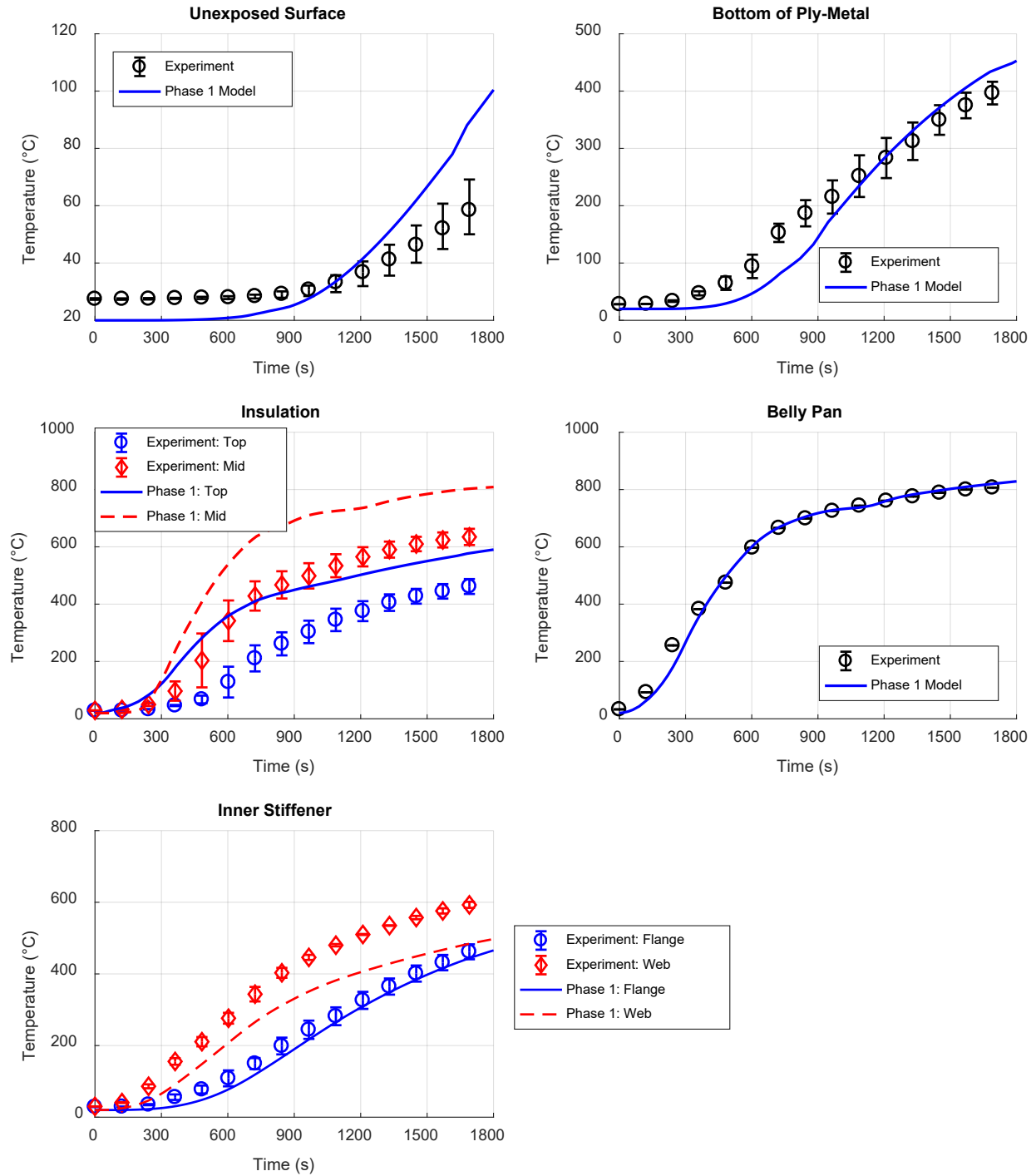
Figure 20. Comparison of predicted thermal response of Test Article 1 from Phase I pre-test models to experimentally measured response
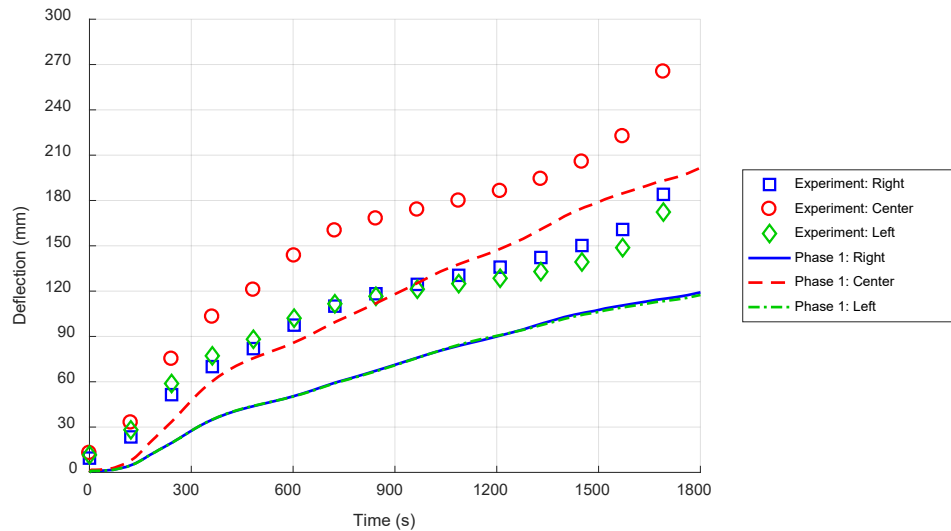
Figure 21. Comparison of predicted structural response of Test Article 1 from Phase I pre-test models to experimentally measured response

4.2 Test Article 2: Full-Scale Longitudinal Supports

The model geometry for the Phase I simulation of Test Article 2 was exactly the same as Test Article 1 as shown in Figure 18. The slight differences between Test Articles 1 and 2, particularly the presence of the transverse channel stiffeners at the transverse ends of the test article, were not included in the pre-test models. The only difference between the simulations of Test Articles 1 and 2 in the Phase I models was the support conditions. The simulation for Test Article 2 included support of the entire side-sill bottom flange as a proposed alternative boundary condition. No confinement of the test article was modeled as described in NFPA 130. The thermal boundary conditions for the exposed and unexposed surfaces of Test Article 2 were exactly the same as Test Article 1. Thus, the predicted thermal response of Test Articles 1 and 2 from the pre-test simulations is the same.

A comparison between the predicted thermal response for Test Article 2 from the Phase I model and the measured response is shown in Figure 22. At the unexposed surface, the impact of moisture within the core of the experimental test article can be observed by the pause in heating at 100 °C. The predicted temperature at the bottom of the ply-metal agrees well with the experiment. Predicted insulation temperatures have a similar level of accuracy as the Test Article 1 predictions. However, the impact of variation in measured insulation temperature as seen in Figure 15 and the accuracy of the model prediction can be seen when comparing this to the Test Article 1 predictions. Temperature predictions of the internal structural stiffener are of similar accuracy to the Test Article 1 results.

The structural response of Test Article 2 was generally under-predicted when compared to the measured response as seen in Figure 23. Considering the relative accuracy of the thermal predictions, this suggests that there is another phenomenon contributing to the increased deflection of the test article. It was suspected that small amounts of slipping between the ply-metal panels and the underlying steel frame attributed to this under-prediction. More about this and how the models were adjusted to include this phenomenon is provided in Section 5.1.1.

28
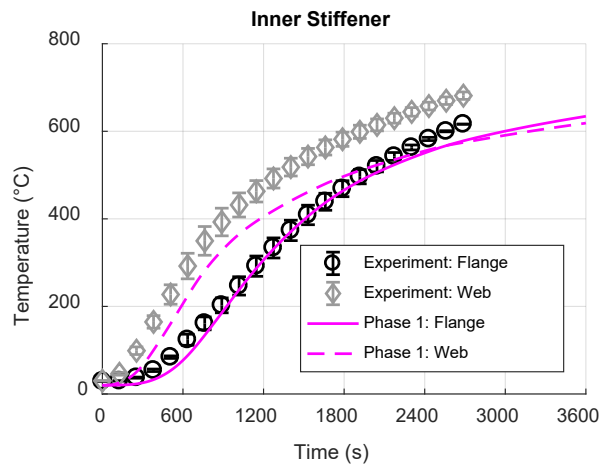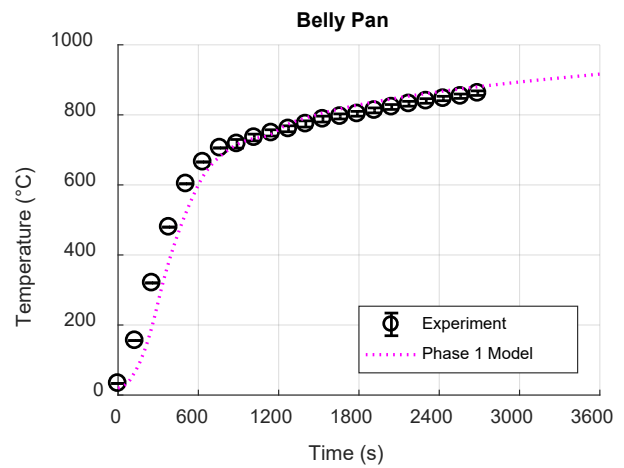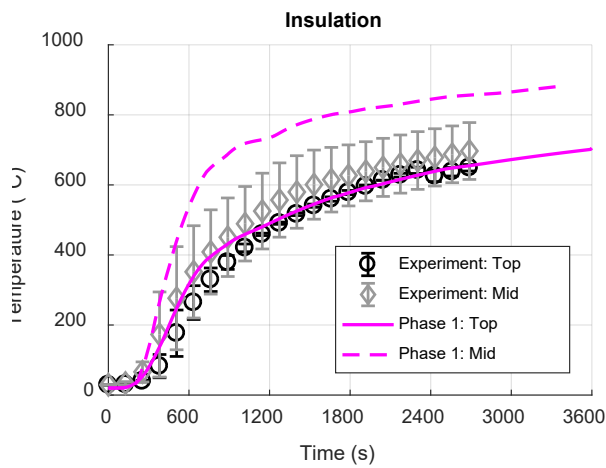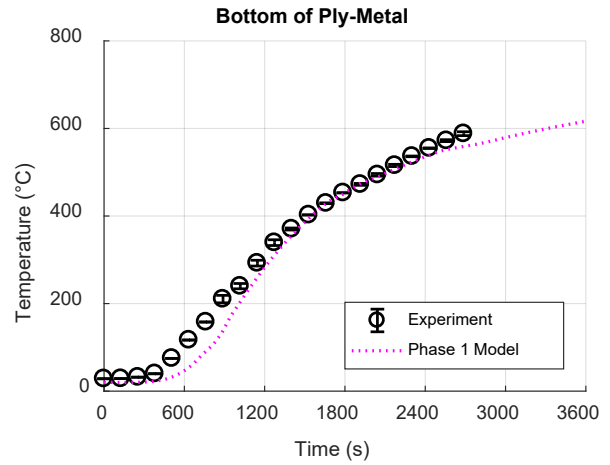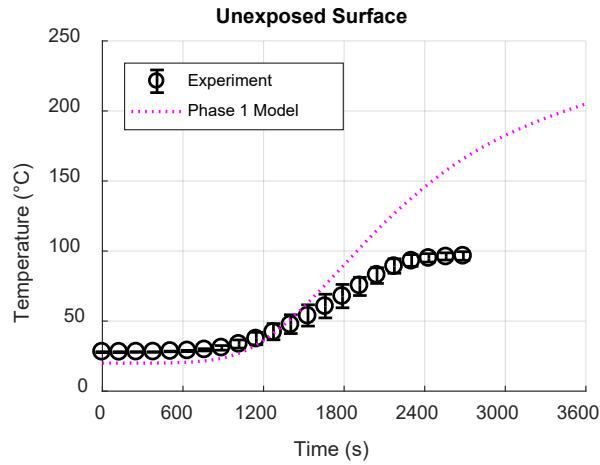
Figure 22. Comparison of predicted thermal response of Test Article 2 from Phase I pre-test models to experimentally measured response
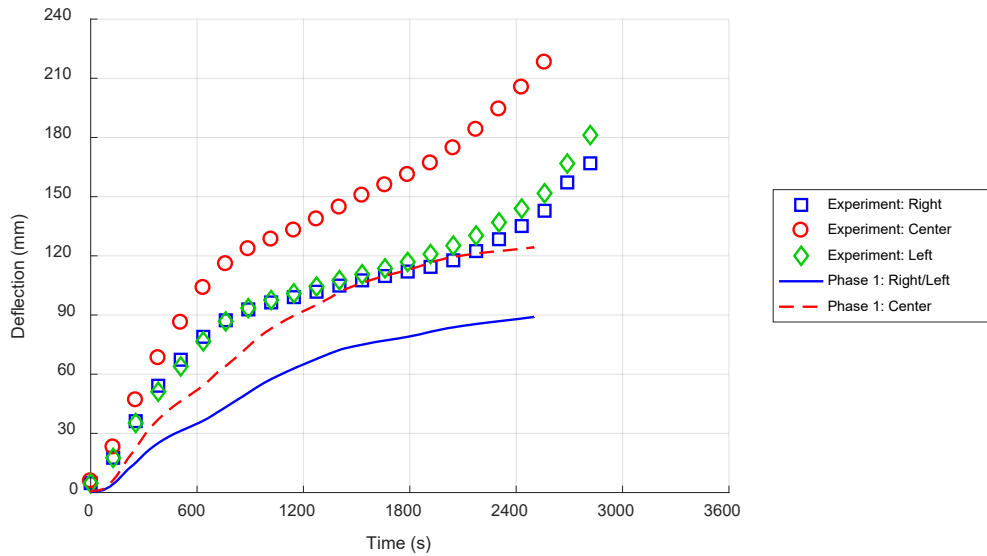
Figure 23**. Comparison of predicted structural response of Test Article 2 from Phase I pre-test models to experimentally measured response**

4.3   Test Article 3a: Reduced Scale Longitudinal Supports

The model geometry for Test Article 3a is shown in Figure 24. Note that only half of the geometry is shown to reveal the internal structure and fiberglass insulation. The model included the carbon steel frame and side sill, belly pan, ply-metal panel, and fiberglass insulation. Like the analysis of Test Articles 1 and 2, the fiberglass insulation was not included in the mechanical model as it does not contribute to the mechanical behavior and does not represent a significant mechanical load on the assembly. Like Test Article 2, Test Article 3a was modeled as being supported on the entire bottom flange of the side sill. No confinement of the test article was modeled as described in NFPA 130.

The same temperature dependent thermal properties of steel, plywood, and fiberglass insulation used in the models of Test Articles 1 and 2 were also used for Test Article 3a. Likewise, the same thermal boundary conditions used to capture the exposed and unexposed surfaces as well as the internal cavity radiation within for Test Articles 1 and 2 were also used for the model of Test Article 3a.
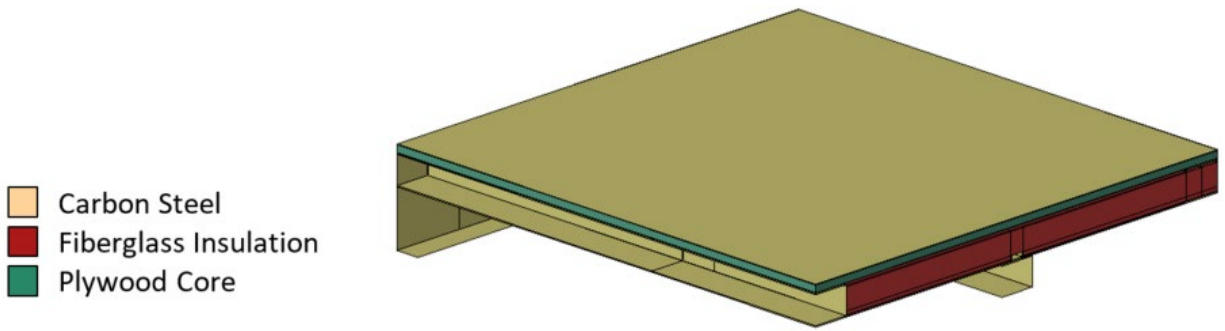
Figure 24. Phase I model geometry for Test Article 3a

The predicted thermal response of Test Article 3a is compared to the measured temperatures in Figure 25. The unexposed surface temperature is over-predicted, especially in the second half of the 60-minute exposure, because the impact of moisture content in the plywood core was not considered in the Phase I models. Like the models for Test Articles 1 and 2, the temperature at the bottom surface of the ply-metal is well predicted but the fiberglass insulation temperature is over-predicted. Temperature predictions of the belly pan and inner structural member are again of similar accuracy as the Test Article 1 and 2 models. Note that the shielding of the transverse ends of the Test Article 3a in the experiment as discussed in Section 3.5 does not impact the measured thermal response at the locations of the thermocouples. This is because the thermocouples were generally placed near the longitudinal center of the test article away from the transverse ends.

The predicted deflection of Test Article 3a is generally over-predicted when compared to the experimental measurements as seen in Figure 26. This is the opposite trend when compared to the predictions of Test Articles 1 and 2. This reversal is because the deflection of Test Article 3a was significantly less than Test Articles 1 and 2 as seen in Figure 16. The model of Test Article 3a does not capture this reduction in deflection because it does not include the effects of the thermal shielding of the transverse ends of the test article. Because of this, the predicted response is similar to that of Test Article 2.

31
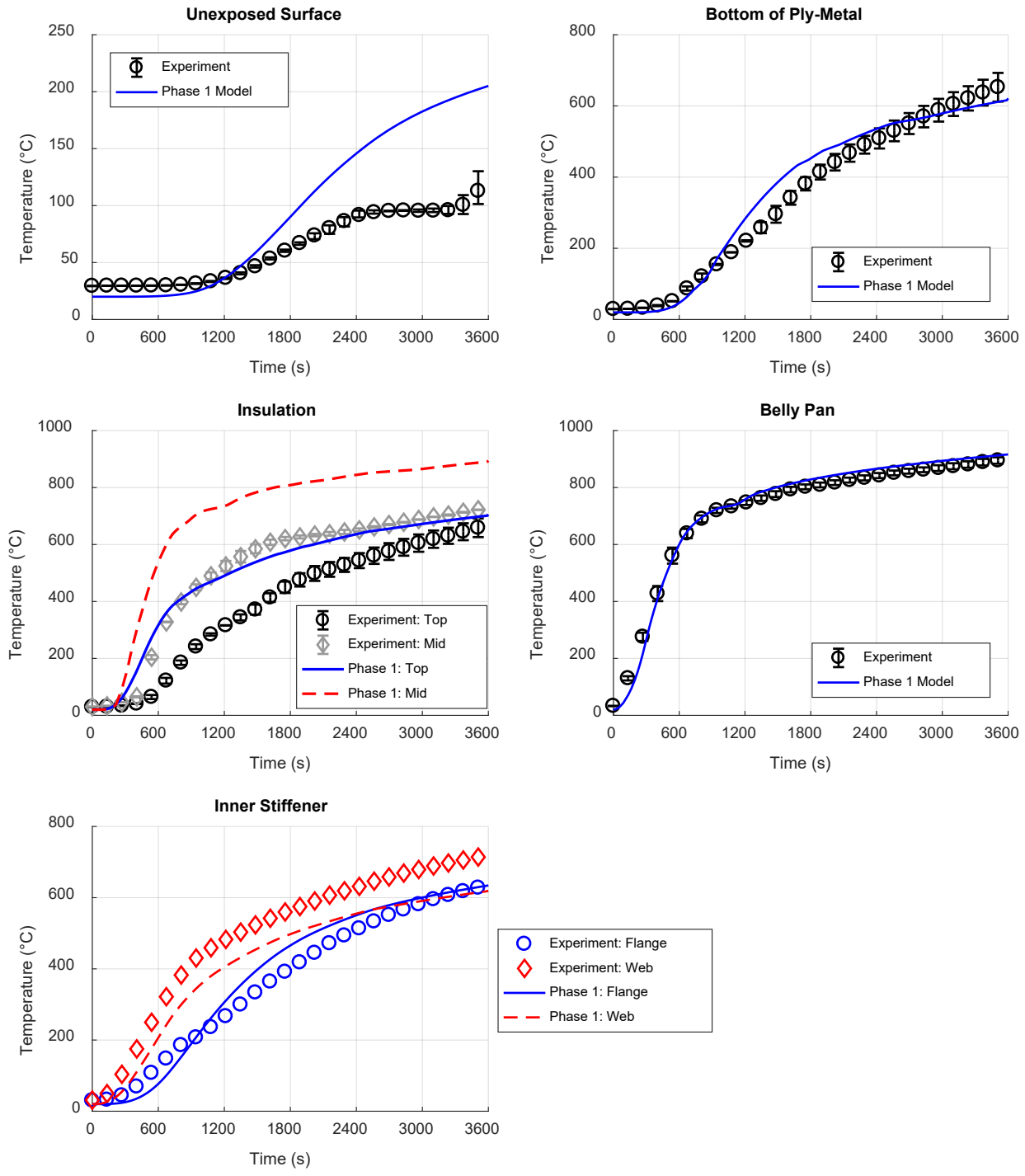
Figure 25. Comparison of predicted thermal response of Test Article 3a from Phase I pre-test models to experimentally measured response
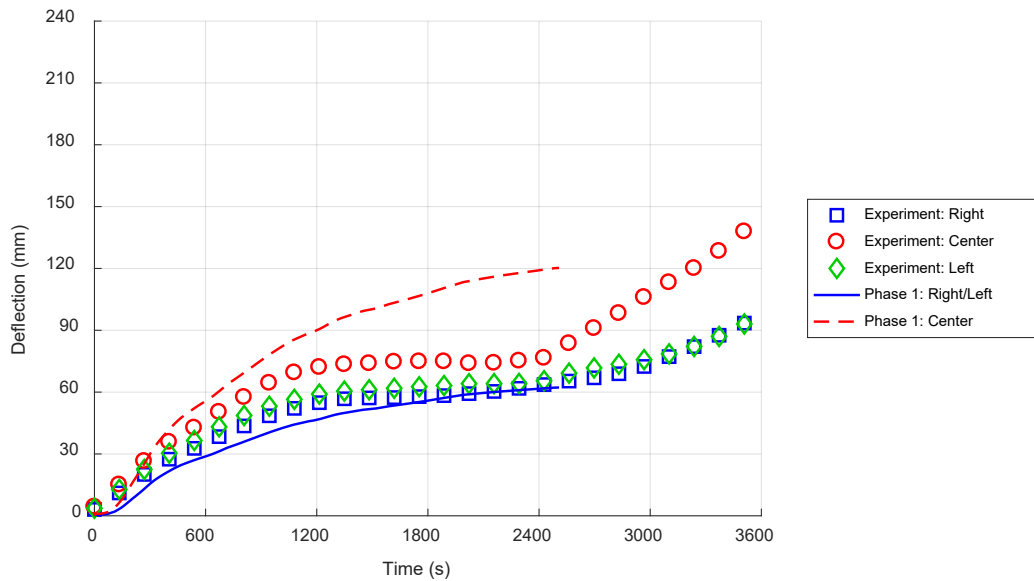
Figure 26. Comparison of predicted structural response of Test Article 3a from Phase I pre-test models to experimentally measured response

4.4 Test Article 3b: Reduced Scale Alternative Design

The model geometry for the Phase I simulation of Test Article 3b is shown in Figure 27. Note that only half of the test assembly is shown to reveal the internal structure and fiberglass insulation. The model domain included the steel frame and belly pan, FRP/balsa composite topper panel, and internal insulation. Like the previous models, the fiberglass insulation was only included in the thermal model of Test Article 3b. The model of Test Article 3b was supported from the longitudinal ends like the experiment leaving the large center sill unsupported. A split in the FRP/balsa composite panel for the Phase I simulation was modeled at the hat channel on top of the frame. Because the model geometry was developed before the test article was fabricated, the handling of the topper panel at the hat channel on the actual test article was unknown, and a compliant solution had to be assumed.

The same temperature dependent thermal properties for steel and the fiberglass insulation from the previous test article models was also used in the model of Test Article 3b. Test Article 3b also included temperature dependent properties of the balsa core from the engineering literature [5]. This included both thermal and mechanical properties. Material properties for the FRP skins was obtained from manufacturer data on phenolic resin composites. There is a significant variation in the performance of different manufactured phenolic composites so there was expected to be significant uncertainty regarding the FRP skin properties used in the Phase I and II models before properties for the specific composite used here could be explored.

The same thermal boundary conditions used in the models of the other test articles were used in the model of Test Article 3b. This includes the input parameters for the convective and radiative boundary conditions on the exposed and unexposed surfaces. Note that the interior cavity of the center sill was assumed not to be exposed to the hot gases of the furnace. While not sealed, the small openings at the transverse ends were expected to minimize gas flow in and out of the cavity.
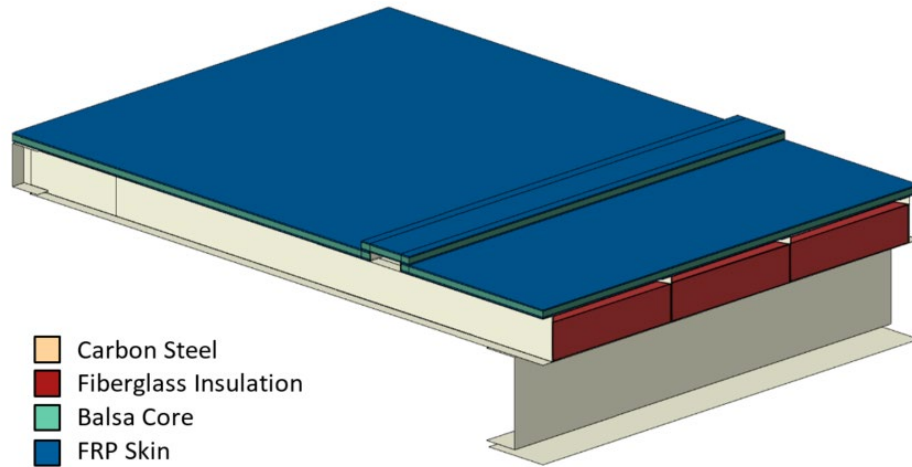
Figure 27. Phase I model geometry for Test Article 3b

A comparison between the predicted and measured thermal response of Test Article 3b is provided in Figure 28. The predicted temperature at the bottom and top of the FRP/balsa panel is not well predicted by the model, suggesting that the exemplar properties obtained from manufacturer data do not include all the relevant energetics. This is further supported by a poor prediction of the top flange temperature of the inner transverse stiffener. Insulation temperatures are generally well predicted by the model as well as the belly pan temperatures.

The predicted deflection of Test Article 3b under the exposure and loading conditions was higher than the measured values as seen in Figure 29. The assumed discontinuity of the FRP/balsa floor panel at the hat channel is a significant contributor to this over-prediction. Additional uncertainty can be attributed to uncertainty in the high temperature mechanical properties of the FRP/balsa including softening, weakening, and expansion.
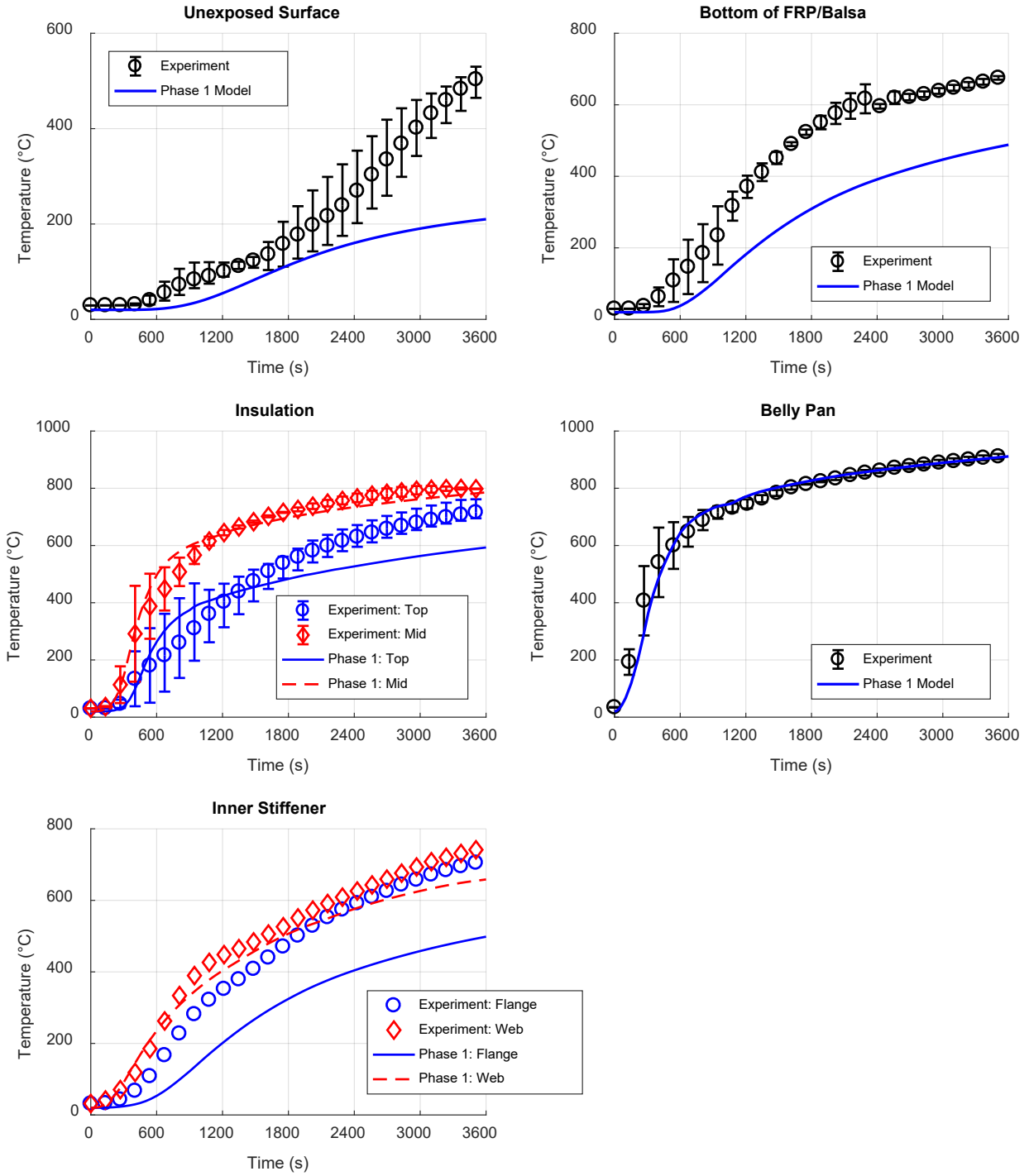
Figure 28. Comparison of predicted thermal response of Test Article 3b from Phase I pre-test models to experimentally measured response
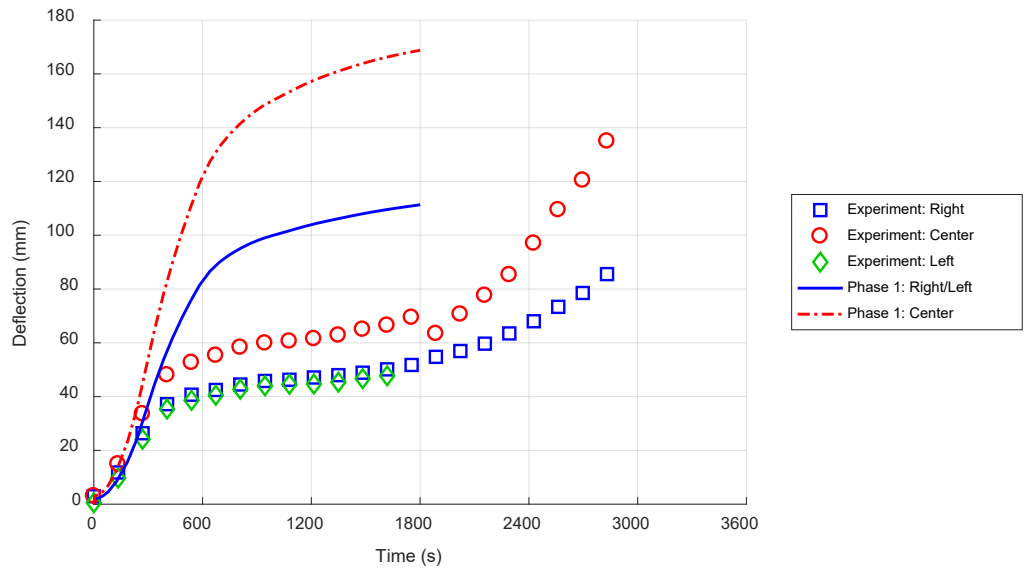
Figure 29. Comparison of predicted structural response of Test Article 3b from Phase I pre-test models to experimentally measured response

5. Post-Test Corrected Modeling (Phase II Models)

The purpose of the Phase II models was to correct discrepancies between the idealized theoretical conditions used in the Phase I models and the large-scale tests conducted at SwRI. Some of these discrepancies are expected based on unknown test details. These include aspects like the actual furnace time-temperature profile compared to the prescribed ASTM E119 time-temperature profile. Figure 30 contains the furnace time-temperature curves for each of the three large-scale tests compared to the ideal curve in ASTM E119. ASTM E119 allows for a certain amount of deviation in the furnace temperature and the measured furnace temperatures were within allowable limits for all three tests. The following sections discuss the corrections applied to the Phase II models and their impact on the predicted test article performance. Note that only the changes in the simulations between the Phase I and Phase II models are discussed here. A full description of the models is not provided.
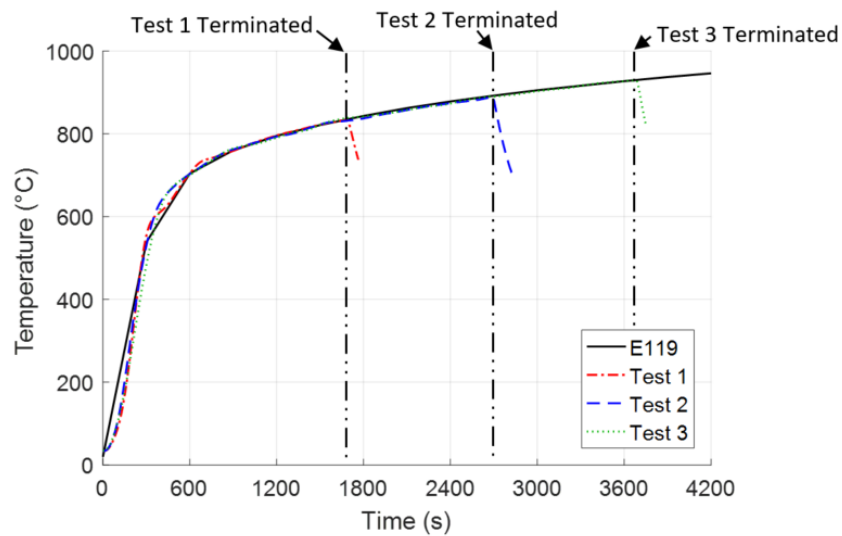
Figure 30. Comparison of ASTM E119 prescriptive fire curve to actual furnace temperature measured in large-scale experiments at SwRI

Many aspects of the Phase II models remained the same as the pre-test models. This included all of the thermal and mechanical properties for all the materials used in the models. Appendix A provides these Phase II material models are provided in. The exposed surface boundary conditions also remained the same as described in Section 1.2.

5.1 Test Article 1: Full-Scale Transverse Supports

Several updates to the model of Test Article 1 were implemented based on the observed experimental setup and results. The following sections describe the specific updates and their impact on the predicted thermal and structural response of the test article.

5.1.1 Model Definition Updates

Several geometric and boundary conditions were made to the model of Test Article 1 to rectify discrepancies between the pre-test model and the large-scale experiment. The updated model geometry and material are shown in Figure 31. Note that only half of the model is shown to reveal internal structure. The first change was in the overall length and unsupported span of the

test article. The pre-test model had an overall length and an unsupported span of 3.45 m (136 in.). This was updated to an overall panel length of 3.94 m (155 in.) with an unsupported span of 3.66 m (144 in.). The next modification to be made was to the steel frame member thicknesses. Pre-test models used a frame member thickness of 3.18 mm (0.125 in.). Actual framing member thickness in the large-scale test was 3.0 mm (0.12 in.) so the Phase II model utilized the actual member thicknesses. The Phase II models also included the additional transverse channel member at the transverse ends of the test article to provide local support to the side-sill at the support location.

Carbon Steel
Fiberglass Insulation
Plywood Core
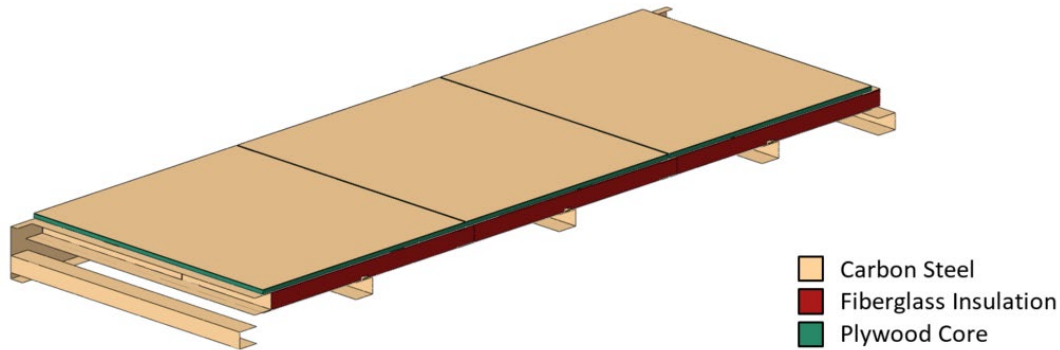
Figure 31. Phase II and Phase III model geometry and materials for Test Article 1

Two modifications were made regarding the ply-metal floor panels. The first is that the three individual panels along the longitudinal direction of test article were considered. The pre-test model considered the ply-metal over the entire sample as a single continuous panel. Secondly, some slippage between the ply-metal floor panels and the underlying steel frame was allowed in the model. This was included because such slippage was observed during the large-scale tests, as seen in Figure 32. The contact between the ply-metal and the steel frame was modeled as a normally hard contact with tangential sliding using a friction coefficient of 0.1. A sensitivity study was performed on the friction coefficient and the predicted mechanical response was found not to be significantly impacted by changes by the friction coefficient value.

Gap

Interference

Figure 32. Observed location of ply-metal floor panel seam (left) before test with approximately 1 mm gap between panels and (right) after test with approximately 2 mm of interference between panels

The last change to be made to the Phase II model geometry is the inclusion of manufacturing error on the large-scale test article. The bottom flange of the right side-sill was not properly welded near the center of the test article, as seen in Figure 33. This defect was not discovered

until the test article was viewed after testing when significant deflection caused a noticeable gap between the connected members.
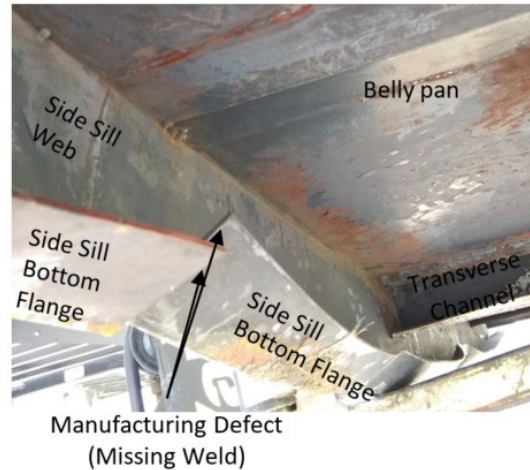
Figure 33. Manufacturing defect on large-scale Test Article 1

5.1.2 Updated Model Results

The updated predictions for the thermal response of Test Article 1 are shown in Figure 34 compared to the Phase I model predictions and experimental measurements. The most significant difference in the predicted thermal response is in the fiberglass insulation. While no changes were made to the fiberglass insulation material model, difference between the Phase I and Phase II model highlights the sensitivity of the thermal response of the fiberglass to the surrounding temperatures. The degradation model is the source of this sensitivity because slight decreases in temperature result in decreases in insulation degradation which result in further decreases in temperature. This feedback mechanism in the model amplifies the impact of input temperatures on the predicted temperatures through the thickness of the fiberglass insulation. The differences in predicted temperature at the bottom of the ply-metal panel and unexposed surface can be attributed to this difference in temperature response of the fiberglass insulation.

A comparison of the predicted structural response from the Phase I and Phase II models as well as the experimental measurements is provided in Figure 35. The Phase II models predict significantly higher amounts of deflection than the Phase I models mainly due to the inclusion of slipping between the ply-metal panel and the underlying steel frame. This results in a Phase II prediction slightly higher than the experimentally measured values. Additionally, the test article was predicted to collapse after 1,670 seconds of exposure which is similar to the experimentally observed value of 1,705 seconds. Note, though, that there are still several inaccuracies within the predicted thermo-structural response and that the accurately predicted failure time is not reflective of a highly accurate prediction in all aspects of the test article behavior.
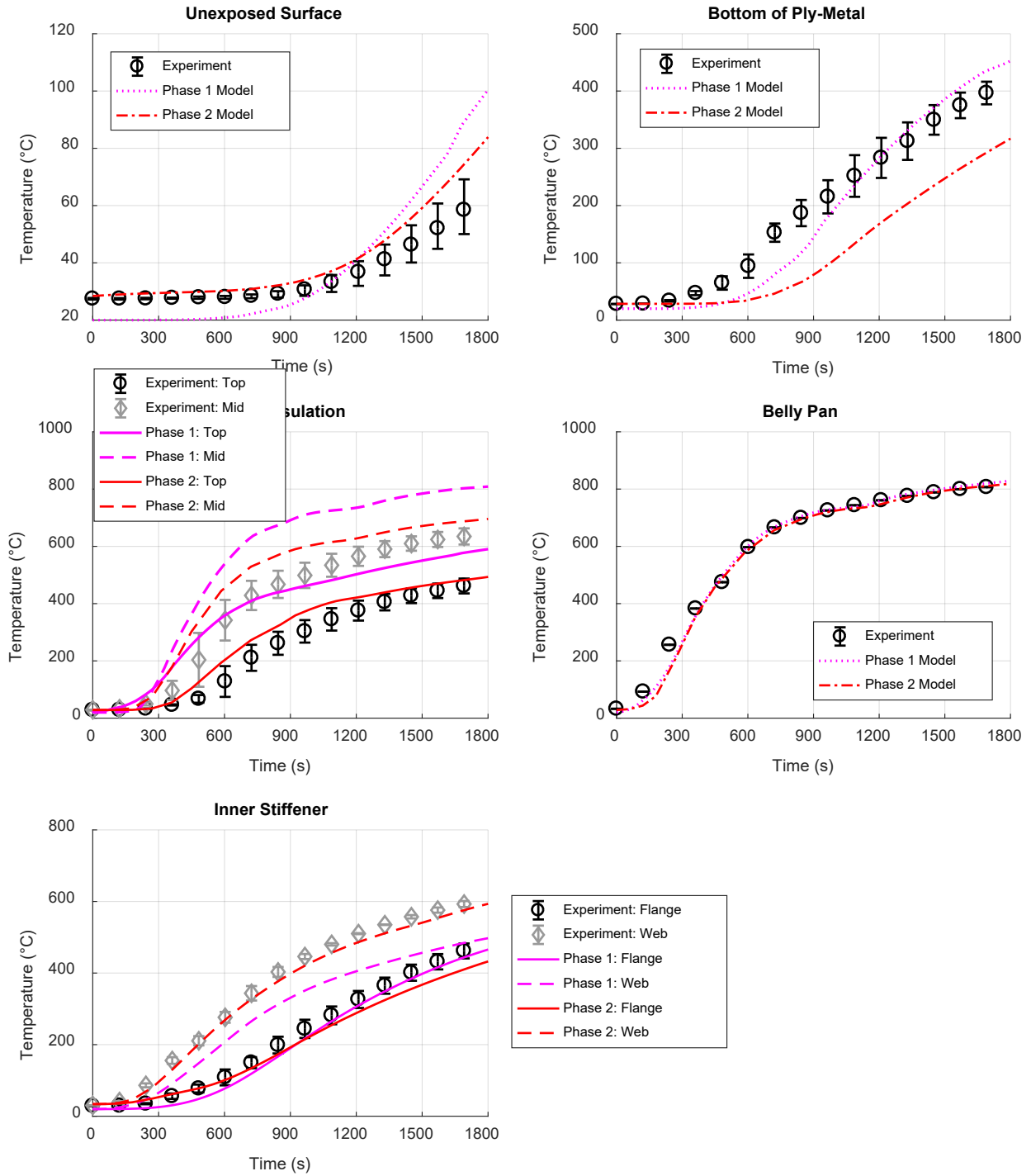
Figure 34. Comparison of measured thermal response of Test Article 1 and predicted response from Phase 1 and Phase 2 models
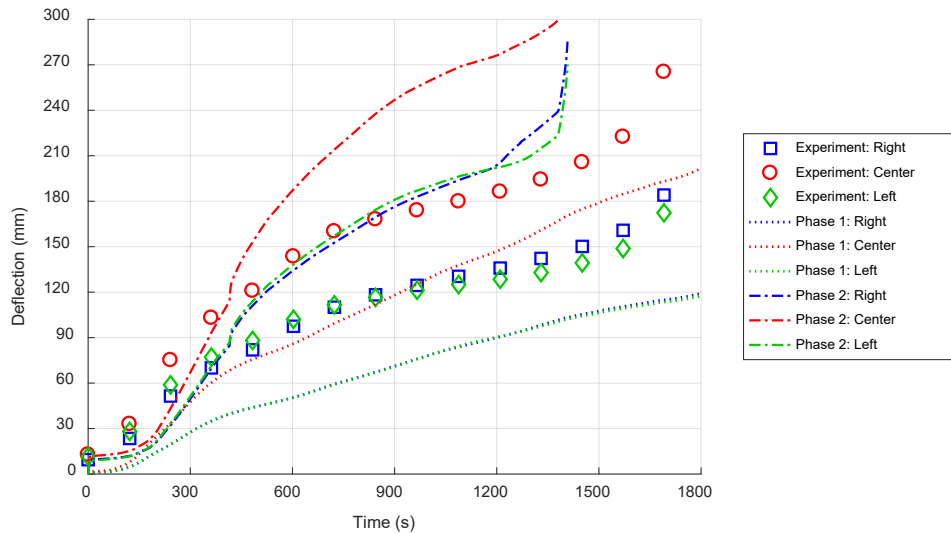
Figure 35. Comparison of measured structural response of Test Article 1 and predicted response from Phase 1 and Phase 2 models

5.2 Test Article 2: Full-Scale Longitudinal Supports

Several updates to the model of Test Article 2 were implemented based on the observed experimental setup and results. The following sections describe the specific updates and their impact on the predicted thermal and structural response of the test article.

5.2.1 Model Definition Updates

Several changes to the model of Test Article 2 were made that were similar to changes made in Test Article 1 described in Section 5.1.1. The longitudinal length of the test article was updated to match the constructed assembly. Likewise, the steel frame member thicknesses were also updated from 3.18 mm (1.25 in.) to 3.0 mm (1.12 in.). The ply-metal floor panel was also discretized and the contact between the floor panel and the underlying steel frame was modeled to allow for slippage as previously described.

The last significant improvement to the Phase II model of Test Article 2 is the inclusion of the steel frame on which the test article was supported. This was done because data from the large-scale test suggested that deformation of the support frame was contributing to the measured mechanical response of the test assembly. The frame consisted of a steel angle with a 152 mm (6 in.) base and 101 mm (4 in.) web, and 9.5 mm (0.375 in.) thick legs. The angle was 4.85 m (191 in.) long and supported at the ends. A pair of channels were welded to the angle and attached to the rigid loading frame above. The channels were separated by 2.34 m (92 in.) and had 38 mm (1.5 in.) legs and a 76 mm (3 in.) web with a thickness of 6.35 mm (0.25 in.). Figure 36 provides the complete test article and support frame geometry used in the Phase II model of Test Article 2. Note that only half of the model geometry shown revealed the internal structure.

41
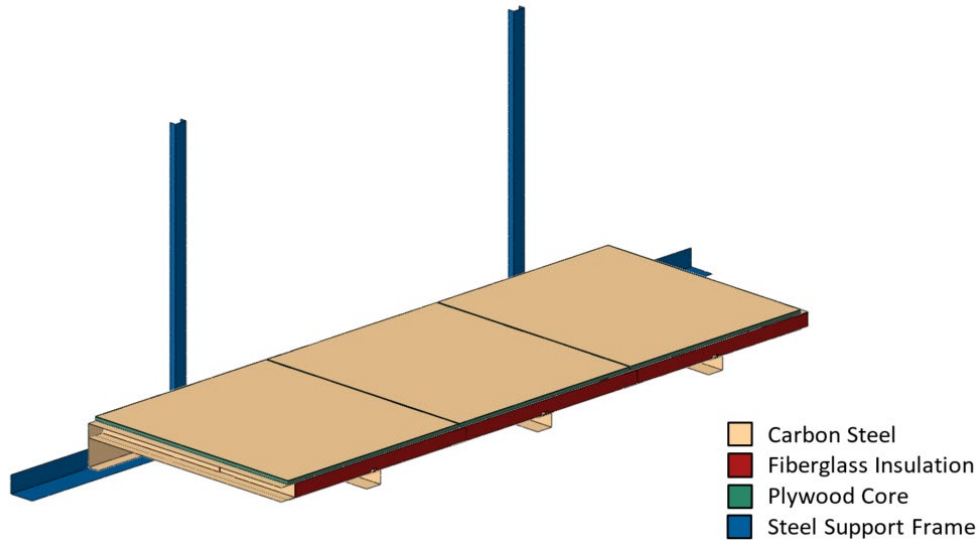
Figure 36. Phase II and Phase III model geometry and materials for Test Article 2

5.2.2 Updated Model Results

The impact of the model updates on the predicted thermal response of Test Article 2 is similar to that of Test Article 1 as seen in Figure 37. Predicted insulation temperatures are lower, resulting in lower temperature predictions at the bottom surface of the ply-metal panel and slightly lower predictions at the unexposed surface.

A comparison of the updated prediction of structural response to the experimentally measured value and Phase I model prediction is shown in Figure 38. Like the Test Article 1 model, there is an increased amount of deflection in the Phase II model due to capture of slipping between the steel frame and ply-metal panels. The impact of this slipping is significant but not as large as Test Article 1 because of the configuration of the ply-metal panels. Since Test Article 2 is spanning the transverse direction, each ply-metal panel covers the entire span. For Test Article 1, there are three individual panels across the unsupported span which amplifies the effects of the slippage. The predicted response of Test Article 2 from the Phase II model is similar to the experimental measurement until the onset of failure in the experiment. The Phase II model still did not predict failure of the assembly within the 60-minute exposure. This suggests the presence of another phenomenon, namely creep straining of the steel, which is contributed to the structural failure of the assembly. The addition of this phenomenon is discussed in the Phase III models in Section 6. While structural failure of the assembly was not predicted, significant buckling deformation of the transverse stiffeners was observed in the models as seen in Figure 39. This is consistent with the buckling behavior observed during the experiment due to the confinement and thermal expansion of the assembly in the transverse direction.

42
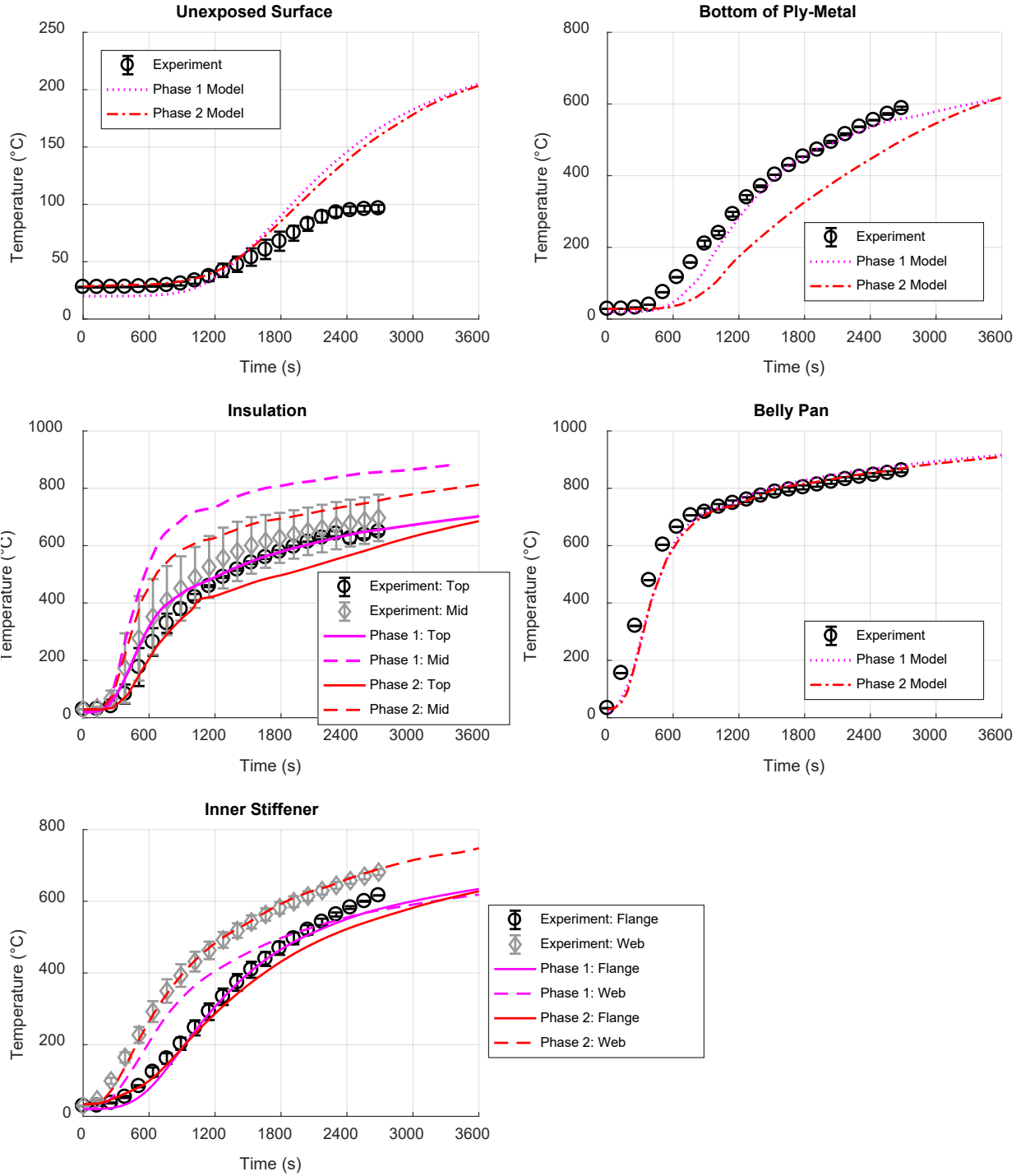
Figure 37. Comparison of measured thermal response of Test Article 2 and predicted response from Phase 1 and Phase 2 models
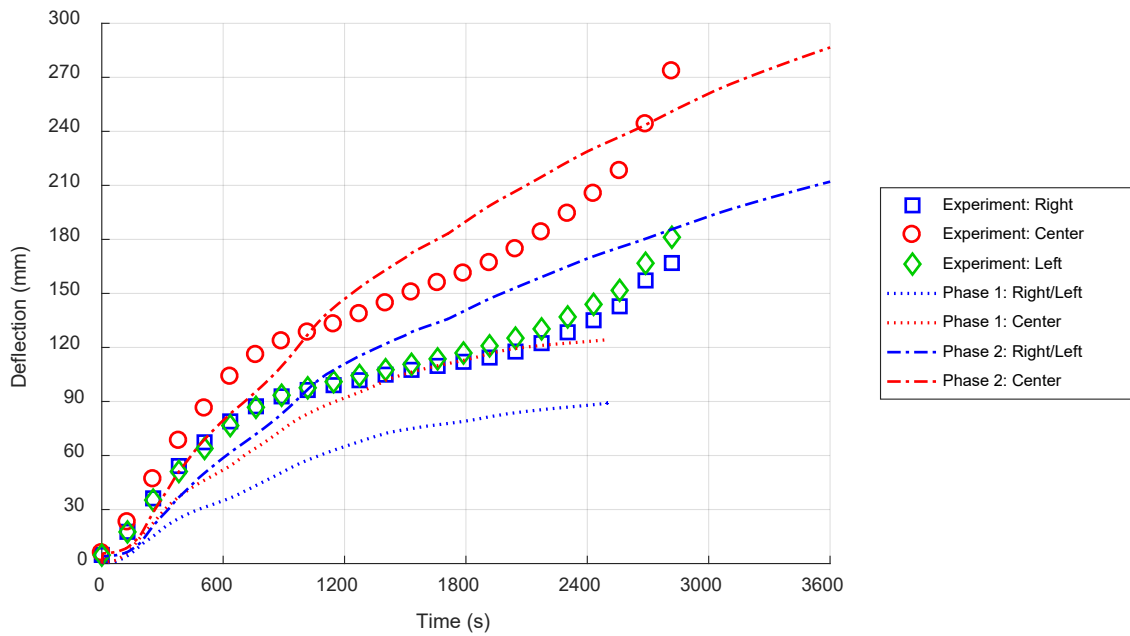
Figure 38. Comparison of measured structural response of Test Article 2 and predicted response from Phase 1 and Phase 2 models
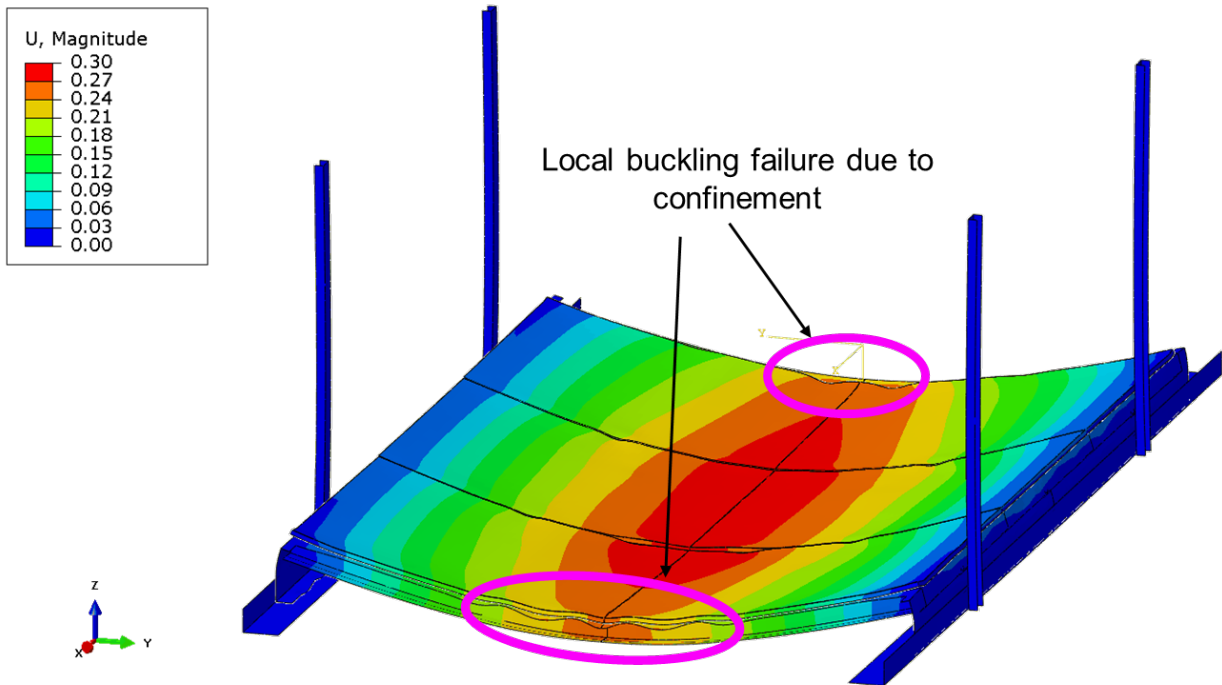
Figure 39. Predicted deformation of Test Article 2 following 60-minute ASTM E119 exposure showing localized buckling failure of transverse members

5.3　Test Article 3a: Reduced Scale Longitudinal Supports

Several updates to the model of Test Article 3a were implemented based on the observed experimental setup and results. The following sections describe the specific updates and their impact on the predicted thermal and structural response of the test article.

5.3.1　Model Definition Updates

Several changes to the model of Test Article 3a were made that were similar to changes made in Test Article 1 described in Section 5.1.1. The steel frame member thicknesses were updated from 3.18 mm (1.25 in.) to 3.0 mm (1.12 in.). Also, the contact between the floor panel and the underlying steel frame was modeled to allow for slippage as previously described.

The only unique update made to the Phase II model of Test Article 3a is the inclusion of some shielding of the unexposed surface. To properly seal the furnace opening around the test article, ceramic fiber blanket insulation was placed in such a manner that the transverse edges of the test sample were shielded from the furnace, as shown in Figure 17. The impact of this shielding on the test article behavior during the furnace exposure was not understood at the time of testing. To account for this shielding effect, the outer 200 mm (8 in.) of transverse ends of the test article belly pan were modeled as an insulated surface rather than exposed to the furnace conditions.

5.3.2　Updated Model Results

Updated predictions of the thermal response of Test Article 3a from the Phase II models are shown in Figure 40 compared to the Phase I predictions and experimental measurements. With the experimental temperature measurements of the unexposed surface extending through the full 60-minute exposure, the over-prediction of unexposed surface temperature due to moisture in the plywood core is evident. These thermal impacts of moisture content will be addressed in the Phase III models as described in Section 6. In general, the difference between the thermal predictions from the Phase I and Phase II models of Test Article 3a are similar to that of Test Articles 1 and 2.

A comparison of the predicted and measured structural response from the Phase I and Phase II models and the experiment is shown in Figure 41. The predicted deflection of the assembly from the Phase II model is not significantly higher than the Phase I model for Test Article 3a like it was for Test Articles 1 and 2. This is because the impact of the thermal shielding of the transverse ends was included in the model of Test Article 3a. This resulted in lower predicted temperature of the transverse stiffeners at the ends leading to lower amounts of material degradation and assembly deflection. There is generally good agreement between the predicted and measured deflection response for the Phase II model and the experiment. However, the model still does not exhibit the distinct pause in deflection between 1,200 and 2,400 seconds that was observed in the experiment. While space was left between the steel support frame and the test article to allow for some transverse expansion, it is possible that the sample did expand enough to interact with the wall of the support structure and some confinement effects are present. This is further discussed in Section 7.2.

45
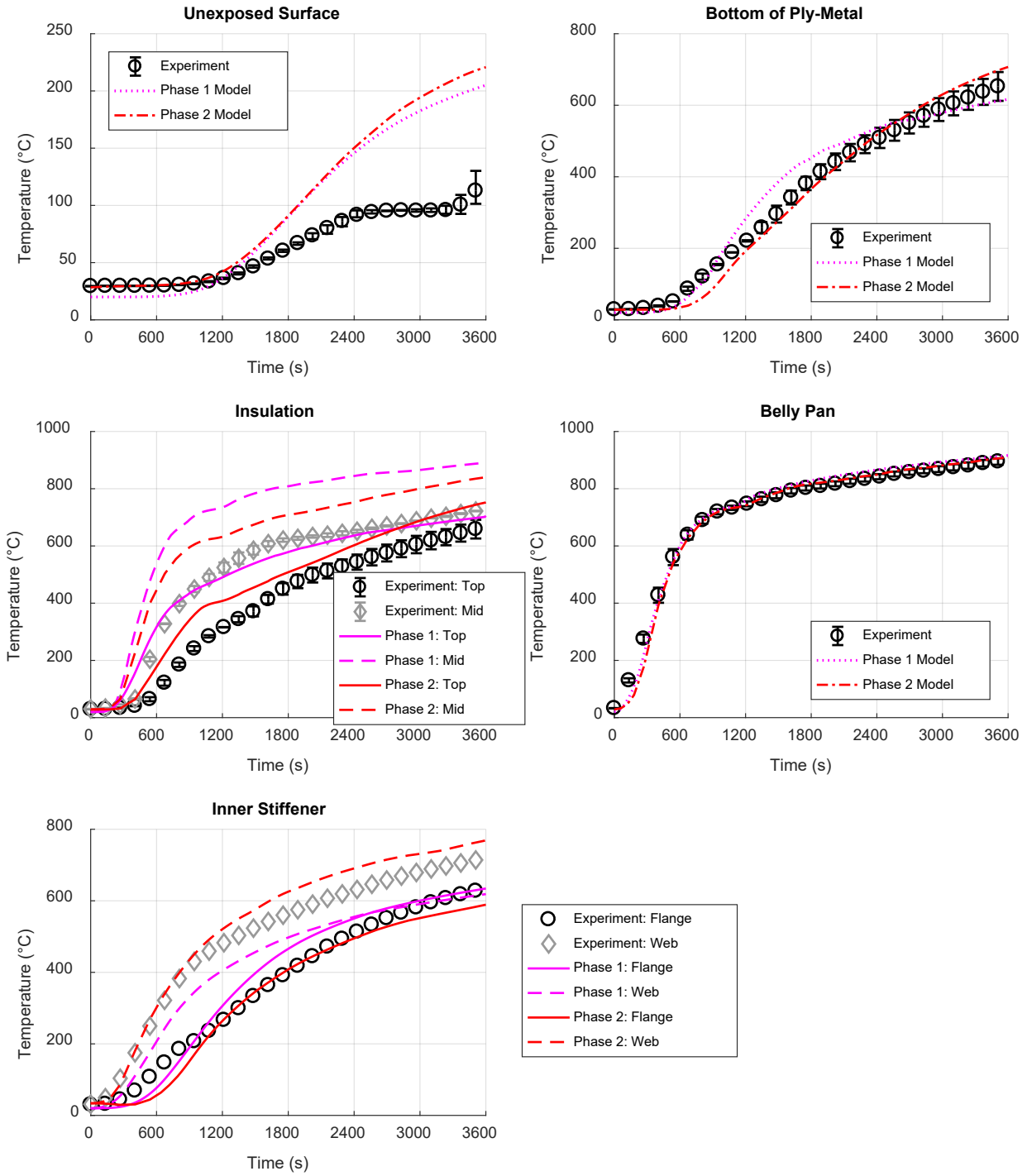
Figure 40. Comparison of measured thermal response of Test Article 3a and predicted response from Phase 1 and Phase 2 models
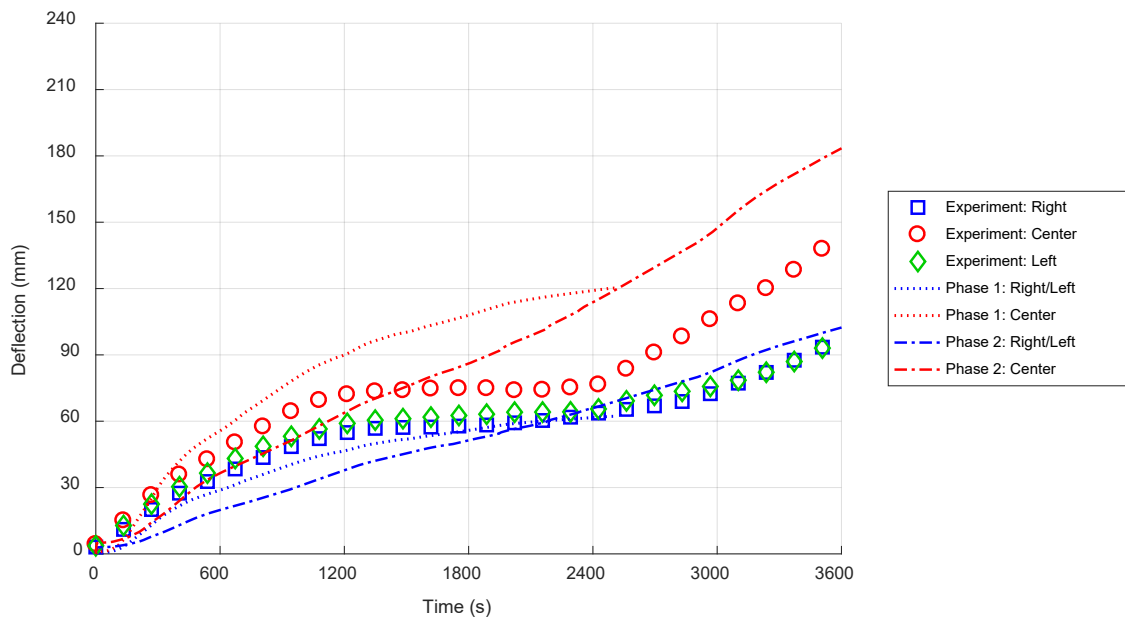
Figure 41. Comparison of measured structural response of Test Article 3a and predicted response from Phase 1 and Phase 2 models

5.4   Test Article 3b: Reduced Scale Alternative Design

Several updates to the model of Test Article 3b were implemented based on the observed experimental setup and results. The following sections describe the specific updates and their impact on the predicted thermal and structural response of the test article.

5.4.1 Model Definition Updates

Several updates to the simulation for Test Article 3b were made in the Phase II modeling effort. Like the other models, the connection method between the steel frame and the floor panel was modified to allow slippage between the frame and panel. Note that the floor panel for Test Article 3b is made of FRP/balsa and not ply-metal like the other three test articles.

The other major change to Test Article 3b model is the floor panel geometry at the hat channel. The frame for this floor assembly contained a 19 mm (0.75 in.) tall hat channel that was mounted to the top of the frame. It was recognized when creating the pre-test model that this hat channel would interfere with the floor panel above. However, it was not known how the manufacturer would reconcile this interference. The pre-test model assumed the floor panel would be cut at the hat channel and an additional piece of panel laid on top as shown in the diagram for the Phase I model in Figure 27. Upon receiving the assembly, it was found that the manufacturer had cut a 13 mm (0.5 in.) deep groove in the floor panel at the hat channel location. This still left 6 mm (0.25 in.) of interference between the steel frame and the floor panel. The floor panel was attached leaving a slightly uneven surface above the hat channel as a result of this interference. This design detail was implemented into the Phase II models as seen in Figure 42. Note that only half of the model geometry is shown to reveal the internal structure. In the simulation, the 13 mm (0.5 in.) groove in the floor panel was included. The floor panel was assumed to separate from the frame 200 mm (8 in.) from the hat channel to account for 6 mm (0.25 in.) of interference.

47

This distance was selected because it was the approximate distance to the nearest screw securing the panel to the frame.
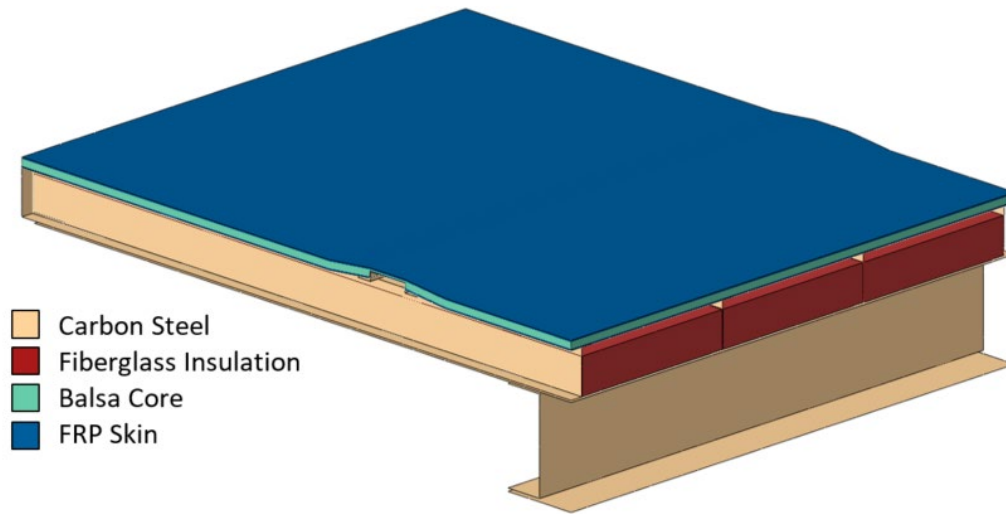
Figure 42. Phase II and Phase III model geometry and materials for Test Article 3b

5.4.2 Updated Model Results

The predicted thermal response of Test Article 3b from the Phase II models is shown in Figure 43 compared to the experimental measurements and Phase I model predictions. The unexposed surface temperature is significantly under-predicted from the models suggesting the thermal behavior of the FRP/balsa material is not well characterized by the literature data. Additionally, it was discovered after additional testing at a smaller scale that the thermocouple pads placed above the thermocouples on the unexposed surface were having a significant impact on the measured temperature when the unexposed surface temperatures were in excess of 200 °C. Because of this, the thermocouple pads were explicitly considered in the Phase III model of Test Article 3b as discussed in Section 6.4. These temperature levels were not obtained in the full-scale tests of Test Articles 1, 2, and 3a due to the apparent high levels of moisture within the plywood core. This means that the impact of the thermocouple pads on the measured response of the other test articles is not significant like on Test Article 3b. The predicted temperature at the bottom of the FRP/balsa and in the internal structural member was significantly below the measured values. This was attributed to the FRP/balsa being more insulative than captured by the manufacturer data such that more energy was captured below the composite panel.

The updated prediction of the structural response is shown in Figure 44. This is again compared to the Phase I model results and the experimental measurements. The Phase II models predicted less deformation than the Phase I models for Test Article 3b. While the slipping between the FRP/balsa panel and underlying steel frame was included in the Phase II model, the presence of the hat channel limited the impact of that change. The Phase II model of Test Article 3b also did not predict failure of the assembly during the 60-minute exposure which does not align with the experimental observation. Like the Test Article 2 prediction, this suggests another phenomenon, creep strain of the steel, that is contributing to the failure behavior. The addition of the steel creep behavior and its impact on the response is further discussed in Section 6.
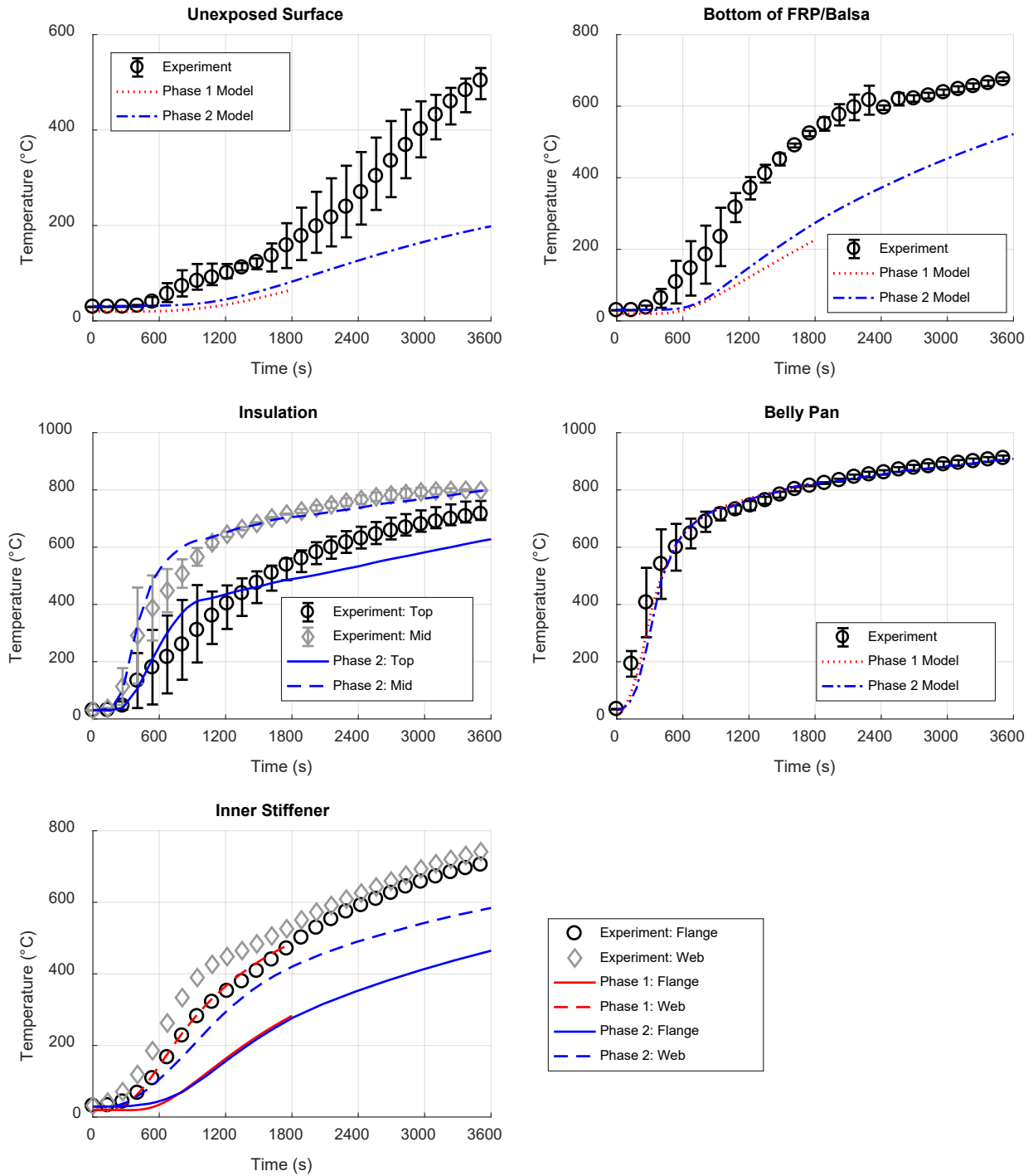
Figure 43. Comparison of measured thermal response of Test Article 3b and predicted response from Phase 1 and Phase 2 models
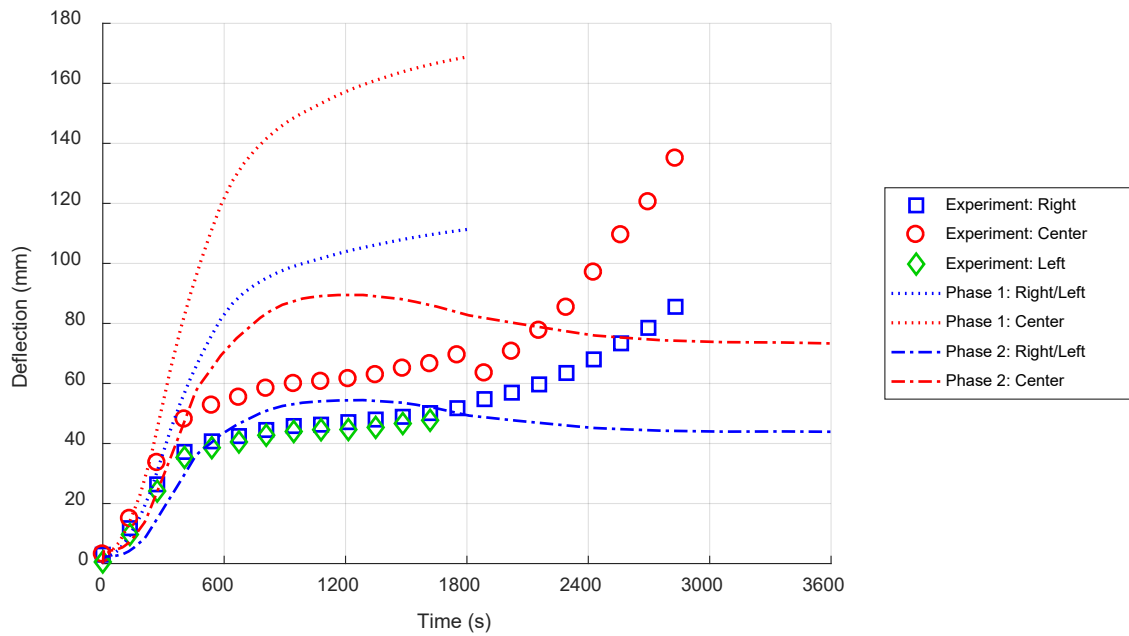
Figure 44. Comparison of measured structural response of Test Article 3b and predicted response from Phase 1 and Phase 2 models

6. Small and Intermediate Scale Material Testing

A series of small- and intermediate-scale thermal and mechanical tests were conducted on materials and sections present in the large-scale railcar floor assemblies. The purpose of these thermal and mechanical tests was to provide updated input and validation data for the material models used in the simulations of the large-scale tests. The testing program consisted of small-scale thermal tests conducted in a cone-calorimeter, intermediate-scale thermal tests conducted in a furnace, and small-scale mechanical tests conducted in a mechanical load frame. Thermal experiments were conducted at the Jensen Hughes laboratory in Baltimore, MD, while mechanical experiments were conducted at the Virginia Polytechnic Institute and State University (Virginia Tech) in Blacksburg, VA. The following sections describe the suite of experiments: the manner in which the tests were conducted, the measurements obtained during the test, and the processing of test data to develop and validate updated material models for use in the Phase III simulations.

6.1 Test Methods

Researchers used cone calorimeter, furnace, and mechanical testing, which are described below.

6.1.1 Cone Calorimeter Testing

The cone calorimeter test is considered to be an industry standard for measuring the response of materials exposed to constant radiant heating from a calibrated emission source. In this test a horizontally oriented specimen measuring 10 cm by 10 cm (4 in. by 4 in.) in area is positioned under the heater assembly, and its response to this simulated fire exposure is measured. The sample mount used in these exposures consisted of a 3.18 mm (0.125 in.) thick steel pan, with 51 mm (2 in.) of ceramic fiberboard insulation behind the sample. The sample was placed in the mount and surrounded with spun ceramic fiber insulation to minimize edge effects. The primary measurements from this test included the sample mass loss over time, sample exposed surface temperature measured via IR pyrometry of the exposed surface, and the sample unexposed surface measured via a thermocouple attached to the sample mount.

In this study, cone calorimeter tests were conducted on ply-metal composite, FRP skin, and FRP/balsa composite samples. The primary purpose of these cone calorimeter tests was to provide a controlled thermal exposure to generate test data for the calibration of material models. This calibration was done through multi-parameter optimization as described in Section 6.1.1.

6.1.1.1 Thermal Property Optimization

Cone calorimeter data was used to develop updated thermal properties for the plywood in the ply-metal composite as well as the FRP skins and balsa core of the FRP/balsa composite. Property development was conducted using a multi-parameter optimization algorithm called a shuffled complex evolution (SCE) algorithm. The SCE algorithm is a type of genetic algorithm (GA) designed to find global minimums in the presence of many local minima within a multi-parameter domain [6] [7]. The SCE algorithm has been shown to be capable of generating accurate material thermal properties based on small- and bench-scale test data [7] [8] [9].

Optimization was conducted using the one-dimensional heat transfer solver within Fire Dynamics Simulator (FDS). All the tested materials were expected to undergo multiple

decomposition reactions. Due to the limited data of the cone calorimeter tests and the large-scale simulations for which the properties were developed, the decomposition was simplified to a single effective nth order Arrhenius kinetic reaction.

Once properties were obtained as a function of the Arrhenius kinetic reaction, a heating rate of 5 °C/min was used to convert the properties into temperature dependent properties that can be utilized by Abaqus. 5 °C/min was selected because it is similar to the heating rates measured for the floor panels in the large-scale experiments.

6.1.2 Furnace Testing

Furnace tests were conducted on ply-metal, FRP/balsa, and fiberglass insulation samples. The primary purpose of the ply-metal and FRP/balsa tests was to validate properties determined from cone calorimeter test data and ensure applicability to the full-scale rail car floor assembly tests. The primary purpose of the fiberglass insulation tests was to determine the fiberglass deterioration properties.

The furnace that was used has internal dimensions measuring 3 ft by 3 ft by 4 ft tall. The furnace was heated via two natural gas burners, which are controlled so as to achieve the desired temperature-time profile based on measurements of gas temperature within the furnace. The top side of the furnace can support mounting of four samples, each measuring approximately 12 in. by 12 in., in the horizontal position (underside exposure).

A total of six samples were tested in the small-scale furnace as shown in Table 1. The furnace temperature was controlled to follow the time-temperature curve specified in ASTM E119, which is consistent with the large-scale tests performed at SwRI. Furnace tests were conducted for a duration of 1 hour. Temperature measurements of the samples were obtained during the entire duration of the exposure as well as at least 30 minutes of cooling to better establish the complete thermal history of the samples during the experiment.

Table 1. Small-scale furnace testing schedule

Sample Slot	Furnace Test #1	Furnace Test #2
1	Full rail car cross-section mock-up with ply-metal floor panel	Full rail car cross-section mock-up with FRP/balsa floor panel
2	Ply-metal panel on compressed insulation board	FRP/balsa floor panel on compressed insulation board
3	Not Used	Spin-Glas TC Insulation Degradation
4	Not Used	Alternate Supplier Insulation Degradation

IR thermography of the unexposed surfaces was conducted for all the furnace tests. Temperature measurements using IR thermography are a function of the measured surface's emissivity. Tests involving ply-metal and FRP/balsa composite panels included painting four 76 mm by 76 mm (3 in. x by 3 in.) squares on the unexposed surface with a well-characterized high-emissivity paint [10]. The surface emissivity of the unpainted region can be determined using the IR

measured temperature from the bare surface along with the painted surface and an estimate of the reflected temperature, which is taken as ambient as shown in Equation 1:

Equation 1. Calculation of bare surface emissivity based on thermography measurements

$$\varepsilon_{bare} = \varepsilon_{paint} \frac{T_{bare} - T_{refl}}{T_{paint} - T_{refl}}$$

This technique was used on the ply-metal and FRP/balsa panels to obtain updated estimates of surface emissivity for use in the Phase III models.

6.1.3 Mechanical Testing

Mechanical testing of the FRP/balsa composite panel was conducted to characterize the mechanical response of the FRP and balsa as well as investigate the compression and bending failure mechanisms of the combined composite. All mechanical testing was conducted at room temperature. Jensen Hughes supervised the testing at Virginia Tech. Testing was conducted on an Instron 5984 mechanical load frame.

6.1.3.1 Uniaxial Tensile Testing

Uniaxial tensile testing of the FRP skins was conducted. The purpose of this testing was to develop updated tensile stress-strain curves for input into the Phase III simulations of the large-scale tests. For the tensile testing, the FRP skin was separated from the balsa core using a saw. Tensile test specimens were fabricated and tested in accordance with ASTM D638: Standard Test Method for Tensile Properties of Plastics. Tensile specimens were cut with a 19 mm (0.75 in.) wide gauge section that was the full thickness of the 3.18 mm (0.125 in.) skin. The gauge section was 63.5 mm (2.5 in.) long. Tensile stress was calculated from load data recorded using a 50 kN load cell with 100 N accuracy. Strains were recorded using a 25 mm (1 in.) extensometer with a 0.05 mm (0.002 in.) accuracy.

6.1.3.2 Compression Testing

Compression testing was conducted on the entire sandwich composite cross-section including the FRP skin and balsa core. The compression tests had two primary purposes. The first was to investigate the compressive properties of the balsa core. The second was to investigate the compression failure mechanisms of the sandwich composite.

Compression test samples were 25 mm (1 in.) wide and the entire 19 mm (0.75 in.) thickness of the composite panel. Compression test samples were 200 mm (8 in.) long. Compressive load and strain were measured using the load cell and extensometer described in the previous section. Overall sample deflection was also measured using a linear variable differential transformer (LVDT) with an accuracy of 0.2 mm.

6.1.3.3 Bending Testing

Bending tests were conducted on the complete FRP/balsa composite section to provide validation data for the updated mechanical property inputs being used in the Phase III models and investigate the bending failure mechanisms of the composite. Bending test samples were 25 mm (1 in.) wide and 305 mm (12 in.) long. The support span for the bending tests was 254 mm

(10 in.) and the load span was 25 mm (1 in.). Bending loads and deflection were measured using the same load cell and LVDT described in the previous sections.

6.2   Fiberglass Insulation

Furnace testing was conducted on three different types of spun fiberglass insulation. The first insulation was Johns Manville Spin-Glas TC, the same nominal listed product as used in the large-scale testing at SwRI. It was discovered upon receipt of the material that the insulation manufacturer had changed the formulation for the binder used in the insulation. This was done to include a more environmentally friendly product without the use a formaldehyde. This change did not warrant the renaming of the product name because the new product possesses equivalent thermal properties below the listed operating temperature of 500 °C. However, it's performance above that temperature is not characterized by the manufacturer. It appeared based on the experimental data and observations described in the following sections that the new binder formulation performed worse above the listed operating temperature resulting in higher amounts of degradation than observed in the large-scale tests with the legacy product.

6.2.1   Furnace Testing Setup

A 0.36 m by 0.36 m (14 in. by 14 in.) section of Spin-Glas TC was tested to investigate its degradation behavior at temperatures above 500 °C. In this test, the insulation was placed on a 3.16 mm (0.125 in.) thick steel plate that was exposed to the furnace. Thermocouple measurements of the exposed plate and the unexposed surface of the insulation were obtained. Additionally, the deflection response of the insulation was measured using a laser distance measurement device mounted 0.9 m (3 ft) above the insulation. Deflection measurements were taken every 5 minutes during the experiment.

Additionally, two 0.15 m x 0.36 m (6 in. x 14 in.) sections of spun fiberglass insulation from other suppliers were also tested. These products were Knauf Eco-Batt and Owens Corning Eco-Touch. Like the Spin-Glas TC, thermocouple measurements of the unexposed surface of the insulation were obtained. Deflection measurements of the Owens Corning insulation material were also obtained using the same method described above.

6.2.2   Furnace Testing Results

Figure 45 provides the measured temperature and deflection response of the fiberglass insulation samples. While it appears the Spin-Glas TC product degraded faster and resulted in increased backside temperature rise, this is attributed to non-uniform heating of the test samples. The observed non-uniform degradation behavior from the alternate supplier tests is shown in Figure 46 with the center of the exposed area degrading at a faster rate than the edges. The difference in measured performance between the Spin-Glas TC and the other insulation samples is attributed to the difference in measurement location relative to the exposed area. Considering these non-uniform effects, the backside temperature of the three tested insulations was similar throughout the duration of the exposure despite some qualitative differences in the degradation behavior.

54
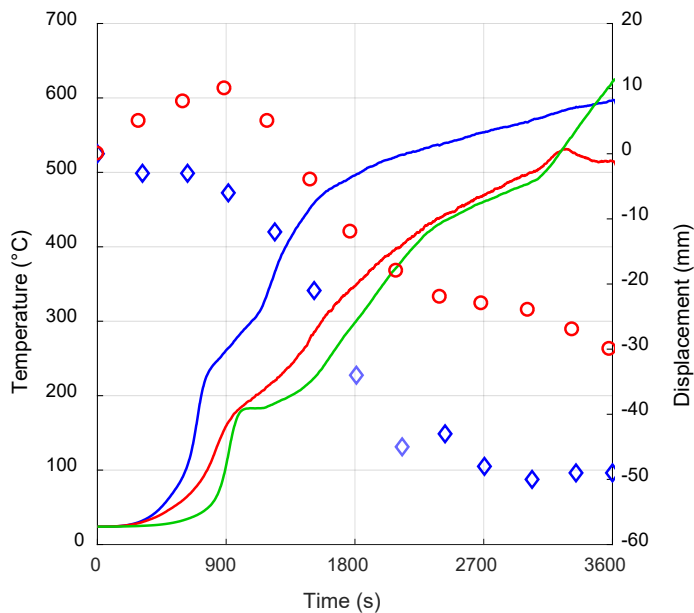
Figure 45. Measured thermal and deflection response of fiberglass insulation subjected to the ASTM E119 temperature profile
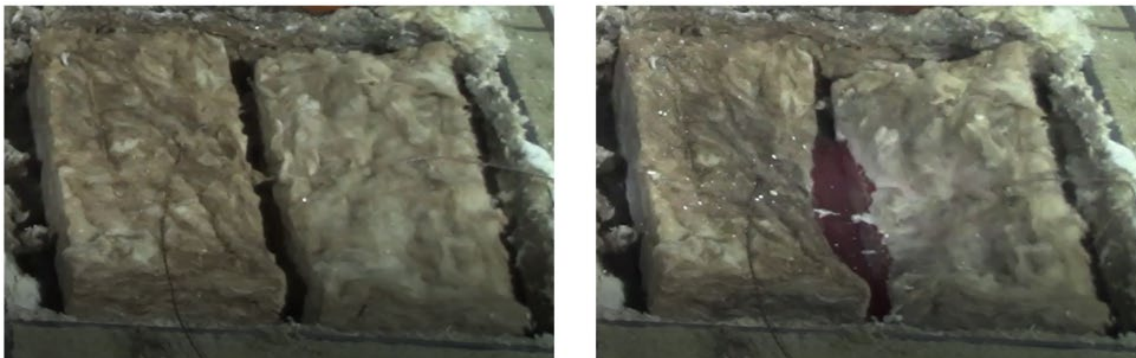
Figure 46. Images of the alternate supplier insulation samples (left) at the beginning of the furnace exposure and (right) after 50 minutes of ASTM E119 exposure

When conducting the furnace testing at Jensen Hughes, a discrepancy between the color of the Spin-Glas TC insulation obtained for the small-scale testing and that used in the large-scale testing was observed. It was discovered that in 2017, the insulation manufacturer changed the binder formulation of the fiberglass insulation for environmental purposes. The large-scale test articles which were fabricated in early 2019 utilized the legacy material manufactured before the switch in 2017. The performance of this new binder was experimentally tested by the manufacturer to ensure similar performance to the legacy material. However, these tests were only conducted up to the operating temperature of material of 510 °C (950 °F). Preliminary testing at Jensen Hughes suggested the performance of the material at temperatures above the operating temperature were different than the legacy material. Of importance, a faster degradation of the material was observed at temperatures above 550 °C. Working with the manufacturer and several distributors, it was determined that the legacy product could not be obtained so testing was conducted with the new product.

55

It is important to note that documented performance of the legacy and new products is identical. The intended use of the fiberglass insulation in the rail car floor assembly may be for acoustic and thermal insulation at low temperature for passenger comfort which is well within the operating temperature of the material. However, the insulation also plays a role in the fire resistance of the floor assembly which puts the insulation temperatures well outside the listed operating limits. Railcar manufacturers must consider that updated formulations to such a product might not result in changes in the published properties or performance of the material but can change the fire performance of the floor assembly in which they are being utilized.

6.3   Ply-Metal Composite

A series of cone calorimeter tests were used to develop an updated thermal material model for the ply-metal composite. These updated properties were calculated from one-dimensional models based on optimization of the cone-calorimeter data. The updated thermal material model was then validated using a pair of furnace experiments. The first furnace experiment consisted of the ply-metal panel protected by ceramic fiberboard insulation. The second furnace experiment was a mock-up of the large-scale railcar floor with the ply-metal panel protected by spun fiberglass insulation.

6.3.1   Ply-Metal Cone Calorimeter Testing

Ply-metal samples were tested in the cone calorimeter at five heat flux levels: 10, 15, 25, 35, and 45 kW/m^2. The two higher heat flux levels resulted in unpiloted ignition of the ply-metal, which was not desired. All ply-metal cone calorimeter samples were painted with high-emissivity, high-temperature paint on the exposed surface [10]. Ply-metal samples were also dried prior to testing to remove moisture within the plywood. This was done by placing the samples in an oven at 110 °C for at least 24 hours prior to testing. The moisture content of the samples was calculated using the mass of the sample before and after testing as shown in Equation 2:

Equation 2. Calculation using the mass of sample before and after testing

$$MC \, (\%) = \frac{m_{wet} - m_{dry}}{m_{dry}} * 100$$

The measured moisture content for nine samples was 5.4±0.6 percent. Note that these samples had been stored in a conditioned laboratory space prior to drying. The density of the virgin plywood was also calculated from the dry mass measurement to be 448±34 kg/m^3.

The measured mass and temperature of the samples during the cone calorimeter experiments is provided in Figure 47. At 10 kW/m^2, the samples underwent minimal mass loss during the 1-hour exposure duration and approached thermal steady state through the thickness of the sample. At 15 kW/m^2, the sample reached thermal steady state, but was still losing mass at the end of the 1-hour exposure duration. At 25 kW/m^2, but the temperature and mass loss of the sample had reached steady state by the end of the experiment. At 35 kW/m^2 and 45 kW/m^2 exposure levels, the time of ignition is shown in the center plot of Figure 47. The presence of ignition meant that these data could not explicitly be used in the multi-parameter optimization. However, the final mass measurement from these tests was used to explicitly determine the mass of the plywood char to be 168 kg/m^3.
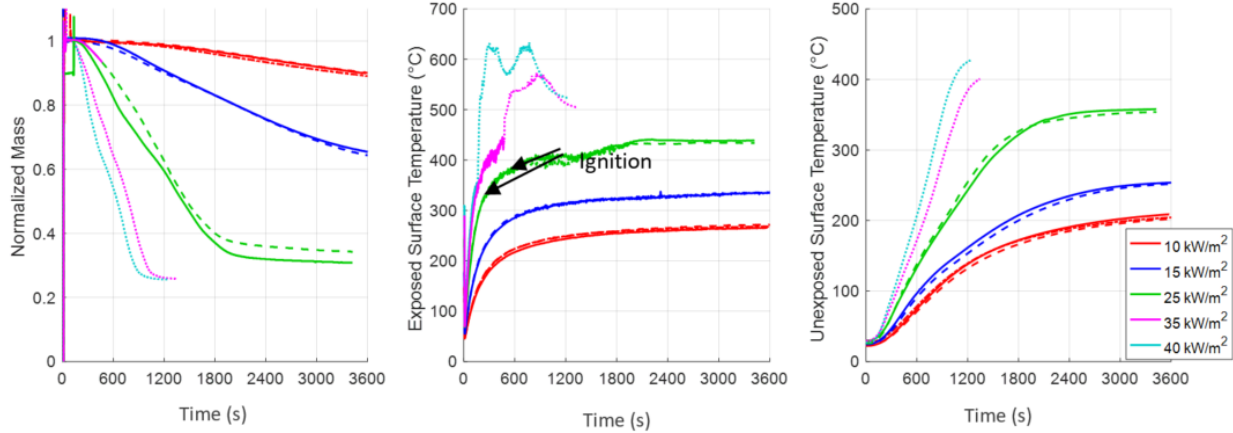
Figure 47. Normalized mass loss (left), exposed surface temperature (center), and backside surface temperature of ply-metal during cone calorimeter exposure (right)

Ply-Metal Cone Calorimeter Data Post-Processing

Optimization of the ply-wood thermal properties was handled slightly differently than the other materials. Initial attempts to utilize the SCE optimization algorithm with the one-dimensional heat transfer solver of FDS led to poor predictions of thermal response, especially the unexposed surface temperature. This was attributed to the possibility of an exothermic decomposition of the plywood glue that was not being considered in the multi-parameter optimization. With the presence of this additional reaction, it was unlikely that the SCE algorithm would produce reliable property inputs given the type and amount of experimental data used in the optimization due to the larger number of property inputs that need to be determined.

A more methodical approach of property determination was undertaken because the SCE algorithm was deemed unlikely to produce accurate property inputs. This involved, first, investigating material thermal conductivity using the steady-state temperature measurements from the end of the cone calorimeter experiments. The transient response and decomposition of the plywood glue was then investigated using the temperature measurements from the 10 kW/m^2 exposure because wood decomposition to char is not expected at the temperatures measured in test [12]. The transient response and decomposition of the wood was investigated using the temperature measurements from the 25 kW/m^2 exposure data. The effects of the exothermic decomposition is implemented using an effective specific heat capacity which is significantly lower than the actual specific heat capacity to account for the energy generated by the reaction. Lastly, the determined properties were benchmarked against the temperature data for the 15 kW/m^2 exposure. The effective temperature-dependent bulk properties are shown in Table 2.

Table 2. Effective temperature-dependent bulk thermal properties of dry plywood

Temperature Range (°C)	Thermal Conductivity k_{eff} (W/m-K)	Density (kg/m^3)	Specific Heat $c_{p,eff}$ (J/kg-K)
20–120	0.15	465	1,800
120–300	0.15	465	0.05
300+	0.13	148	950

The predicted temperature response from all the tested exposures is compared to the experimental data in Figure 48. The developed properties accurately capture the exposed surface temperature response at all the tested exposure levels. The unexposed surface temperature response is well predicted at the lower heat flux levels of 10 kW/m^2 and 15 kW/m^2 but under-predicted at higher temperatures of the highest tested heat flux level. It is possible that there is an additional exothermic reaction occurring at temperatures above 350 °C that is not currently being captured by the simplified property model adopted in this work. However, the unexposed surface temperature of the large-scale test assemblies does not reach these temperatures so this is not expected to impact the accuracy of the large-scale models.
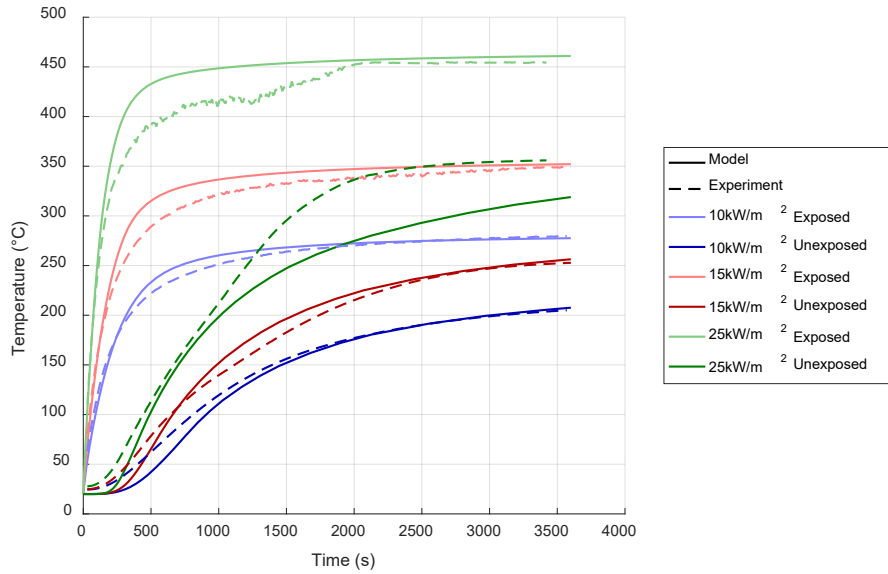
Figure 48. Measured and predicted temperature response of ply-metal under cone calorimeter exposure using optimized thermal properties

The final aspect of material property determination that is not covered by the cone calorimeter tests is the inclusion of the effects of moisture content on the thermal properties. Moisture content in the wood effects the effective bulk thermal conductivity and specific heat capacity of the wood below 100 °C. In this work, the bulk thermal conductivity of the wood below 100 °C was calculated based on a mass average of dry wood and water using the moisture content as shown in Equation 3:

Equation 3. Calculation of effective thermal conductivity of wood including moisture

$$k_{wet} = (100 - MC)k_{dry} + MC * k_{water}$$

The effective specific heat capacity of wet wood was calculated by adding the specific heat capacity of the moisture in the wood to the specific heat capacity of the dry wood as shown in Equation 4:

Equation 4. Calculation of effective specific heat capacity of wood including moisture

$$c_{p,wet} = c_{p,dry} + \frac{\rho_{water}}{\rho_{dry}} \frac{MC}{100} c_{p,water}$$

Note that the specific heat of water needs to be normalized to the relative density of wood and water to obtain the proper effective total thermal mass of the wet plywood. Moisture in the wood also causes a significant endothermic reaction around 100 °C as the moisture is changed to steam. This is accounted for by a large increase in the effective specific heat capacity of the wet plywood between 100 and 120 °C. The magnitude of this increase in determined from the heat of evaporation of water as shown in Equation 5:

Equation 5. Calculation of effective specific heat to include the heat of evaporation of moisture within the wood

$$\int_{100°C}^{120°C} c_{p,eff}dT - \int_{100°C}^{120°C} c_{p,dry}dT = \frac{\rho_{water}}{\rho_{dry}} \frac{MC}{100} \Delta H_{evap}$$

These modifications to the plywood thermal properties are made for each simulation that includes wet plywood.

6.3.2 Ply-Metal Furnace Testing

Two small-scale furnace tests were conducted using the ply-metal composite panels. The purpose of these tests was to verify the material models for the plywood and fiberglass insulation and develop an estimate of the panel surface emissivity using the method described in Section 6.1.2.

6.3.2.1 Ply-Metal Furnace Testing Setup Details

The first ply-metal furnace test consisted of a ply-metal panel shielded by 6.5 mm (0.25 in.) of ceramic fiberboard insulation and a 1.58 mm (0.063 in.) steel plate. This cross-section is shown in Figure 49. Note that the temperature measurement locations are indicated by red circles. The purpose of the insulation was to provide a heating rate similar to that observed in the large-scale exemplar railcar floor test using an insulation material that is inert and whose properties are well documented up to the temperature observed in a 60-minute ASTM E119 exposure. Temperature measurements were obtained on the back side of the exposed plate on the bottom of the ply-metal and the unexposed surface of the ply-metal. IR thermography was also obtained on the unexposed surface.

19 mm Ply-metal
6.5 mm Ceramic Fiberboard Insulation
1.5 mm Sheet Steel
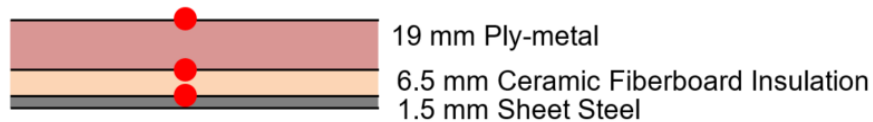
Figure 49. Cross-sectional details for insulated ply-metal panel test

The second ply-metal furnace tests consisted of a one-dimensional mock-up of the exemplar railcar floor assembly. This included a 1.58 mm (0.063 in.) steel plate on the exposed surface. Above that was 76 mm (3 in.) of fiberglass insulation and the ply-metal panel. The ply-metal panel was supported in the corners to allow the fiberglass insulation of degrade in the same manner observed in the large-scale tests. This cross-section is shown in Figure 50 and the temperature measurement locations are indicated by red circles.
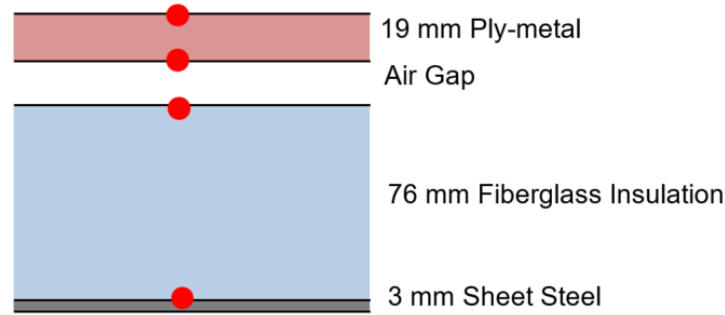
Figure 50. Cross-sectional details for full rail car floor mock-up with ply-metal panel

A one-dimensional model of each of the furnace tests was constructed to validate the properties developed using the cone calorimeter tests and ensure consistency with the large-scale tests conducted at SwRI. The model layouts and meshes are shown in Figure 51. These simulations used the updated material thermal properties for ply-metal determined from the cone calorimeter tests including the effects of 5.8 percent moisture content. The boundary conditions applied to these models were consistent with those applied to the simulations of the large-scale tests.
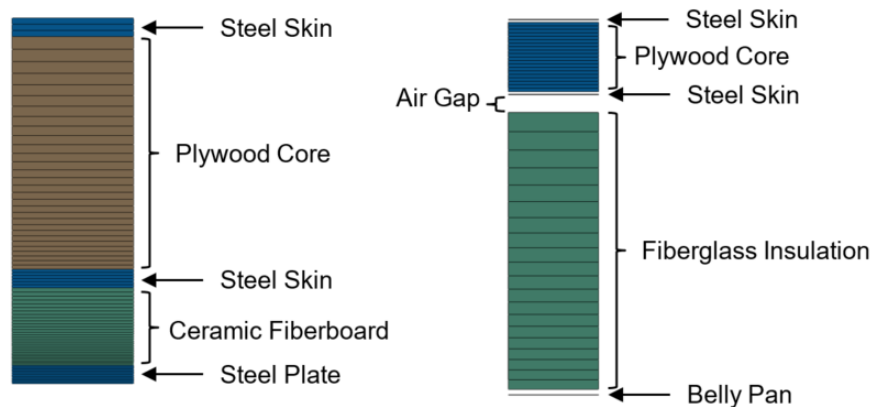
Figure 51. One-dimensional models of ply-metal furnace tests (left) panel protected by 6.35 mm (0.25 in.) of ceramic fiberboard insulation and (right) exemplar floor assembly mock-up

6.3.2.2 Ply-Metal Furnace Testing Results

The measured and predicted temperatures of the ply-metal panel shielded by the ceramic fiberboard insulation are provided in Figure 52. The prediction of the exposed surface temperature generally within 50 °C of experimental measurement except for the short period of extremely rapid heating at the beginning of the test. Like the Phase I and Phase II models of the test articles, this shows that the exposed surface boundary conditions used in the simulations of the furnace exposures accurately capture the temperature exchange at the surface. The temperature prediction of the bottom surface of the ply-metal panel slightly higher than then experimental measurement but still within 100 °C. This slight over-prediction could be due to the perfect representation of the contact between the ply-metal panel and the ceramic fiberboard underneath. The predicted temperature at the unexposed surface followed the same trend as the experimental measurement. Predicted heating rates up to 30 minutes were slightly higher than measured, and temperatures beyond 45 minutes were slightly lower. This is likely because the

temperature at the bottom of the plywood core was reaching char oxidation temperatures beyond 45 minutes causing energy generation within the core leading to an increase in unexposed surface temperature.
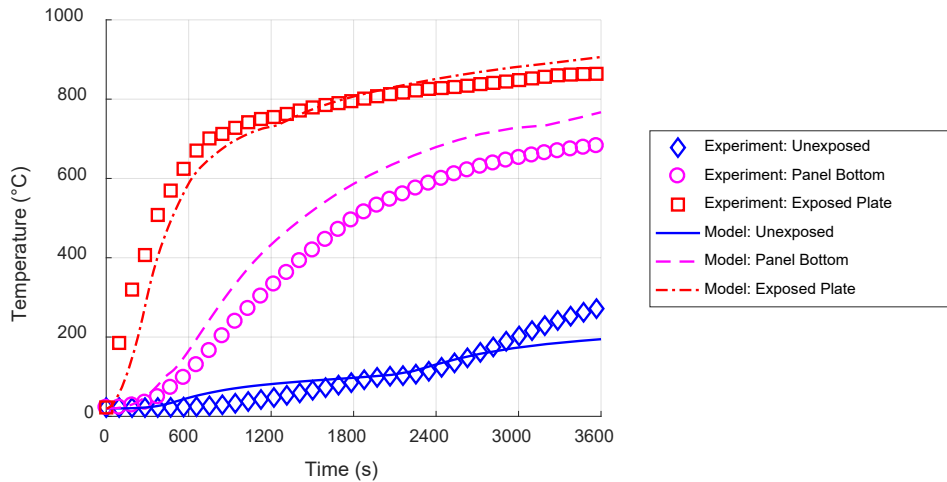
Figure 52. Measured and predicted temperatures of ply-metal panel protected by 6 mm (0.25 in.) of ceramic fiberboard insulation

The measured and predicted temperature response for the floor assembly mock-up is shown in Figure 53. Temperature predictions for the first 30 minutes generally agree with the measured values. In the second half of the experiment, the measured temperature of the exposed surface, top of the insulation, and bottom of the ply-metal panel begin to converge to the same value at approximately 800 °C. This is because the new insulation material was fully degraded by the end of the exposure resulting in the thermocouple measuring the temperature at the top of the insulation resting on the exposed plate and radiation exchange directly between the exposed plate and the ply-metal panel. This further highlights the difference in the decomposition behavior above the operating temperature between the legacy material used in the SwRI experiments and the updated material listed as the same product. The unexposed surface temperature of the ply-metal panel was measured above 350 °C at the end of the 60-minute exposure. The rapid increase in temperature in the last 15 minutes of exposure is partly attributed to the faster decomposition of the insulation when compared to the measured unexposed surface temperature response from the SwRI experiments shown in Figure 6 through Figure 9. It also suggests that the ply-metal panel at the time of the SwRI experiments had a higher moisture content than the panels tested at Jensen Hughes. This resulted in a longer delay of heating at 100 °C in the SwRI experiment.
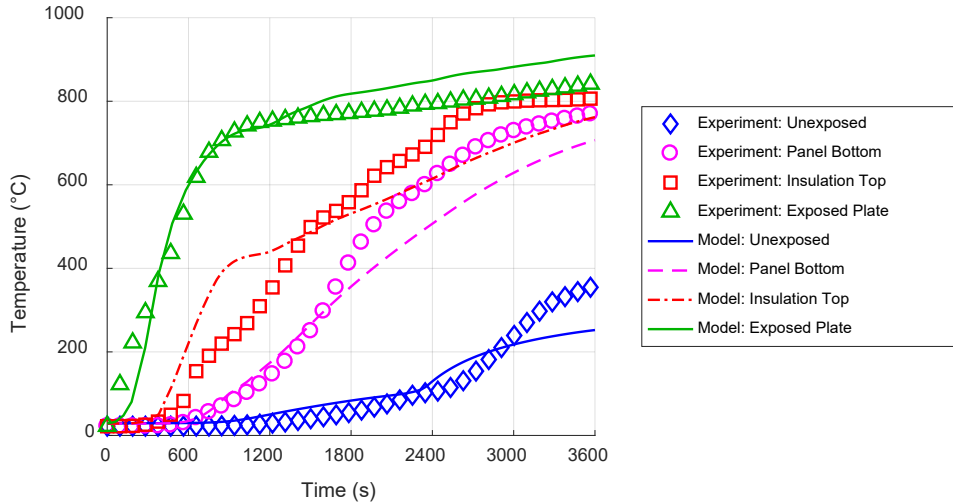
Figure 53. Measured and predicted temperatures of exemplar floor assembly mock-up, including belly pan, fiberglass insulation, and ply-metal panel

6.4 FRP Skins

Thermal and mechanical testing of the FRP skins was conducted to obtain more accurate material input data for the Test Article 3b simulation. The thermal tests consisted of cone calorimeter tests which were used with multi-parameter optimization to develop updated thermal properties. Tensile testing was also conducted at room temperature to better understand the mechanical behavior of the FRP skins. The FRP skins were also used in thermal and mechanical testing of the entire FRP/balsa sandwich composite. Those tests and results are discussed in Section 3.5.

6.4.1 Cone Calorimeter Testing

FRP skin test samples were tested in the cone calorimeter at four heat flux levels: 15, 20, 30, and 45 kW/m^2. None of the cone calorimeter tests resulted in ignition of the test sample. Unlike the ply-metal cone test samples, the FRP skin samples were not painted with high-emissivity paint. This was done to better understand the radiation parameters of the bare FRP skin.

The measured mass loss, exposed surface temperature, and unexposed surface temperature is provided in Figure 54. Note that different line styles denote repeats of nominally identical tests. Increasing amounts of mass loss were measured at higher heat flux levels as expected. The measured mass loss also did not decrease toward zero because while the polymer matrix decomposes at these exposure levels, the glass fibers are not affected. The temperature measurement at both the exposed and unexposed surface temperature exhibit a spike in temperature at higher heat flux levels. This indicates a relatively rapid exothermic reaction that occurs in the polymer decomposition. This can be clearly seen in the temperature results at the 30 kW/m^2 and 45 kW/m^2 heat flux levels while the onset of this reaction can be seen in the 20 kW/m^2 exposed surface temperature data.
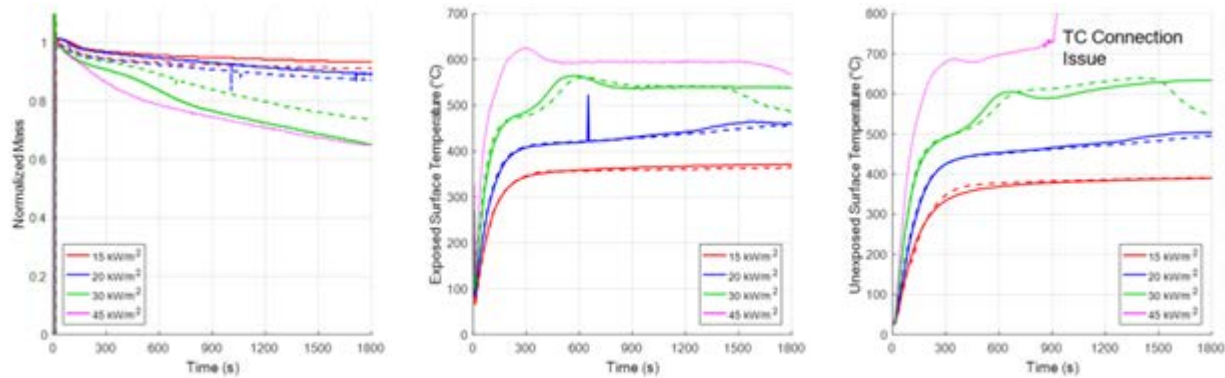
Figure 54. Measurements from cone calorimeter test of FRP skins. Normalized sample mass (left), sample exposed surface temperature (center), and unexposed surface temperature (right)

6.4.1.1 Data Post-Processing

Optimization of the thermal properties of the FRP skins was conducted as discussed in Section 6.1.1.1. Note that the properties developed here are not intended for use above the temperature ranges observed in the cone calorimeter tests. This is because these properties represent the equivalent homogenized properties of the fiberglass and polymer matrix and do not necessarily capture all the decomposition physics applicable to all temperatures and heating rates.

The bulk properties of the virgin and char materials as well as the kinetic reaction parameter to convert virgin material to char is provided in Table 3. The thermal conductivity values obtained from the optimization are approximately one order of magnitude smaller than the properties used in the Phase I models. Similarly, the specific heat capacity value for virgin material is approximately three times smaller than the Phase I value and the effective specific heat of the char is approximately seven times smaller than Phase I when considering the char density.

Table 3. Optimized thermal properties of FRP skin material

Phase Property	Virgin	Char	Reaction Property	Value
Density (kg/m3)	900	416	A (/s)	7.07E13
Conductivity (W/m-K)	1.25	0.45	E (kJ/mol)	180
Specific Heat (J/kg-K)	1,597	1,226	n	1.95

The measured and predicted exposed and unexposed surface temperatures for the cone calorimeter tests of the FRP skins is provided in Figure 55. The optimized material properties generate accurate predictions of heat rate on both the exposed and unexposed surfaces. The predicted exposed and unexposed surface temperatures are generally within 50 °C of the experimental values when considering that the optimization did not attempt to capture short spikes in temperature due to the exothermic reactions.

63
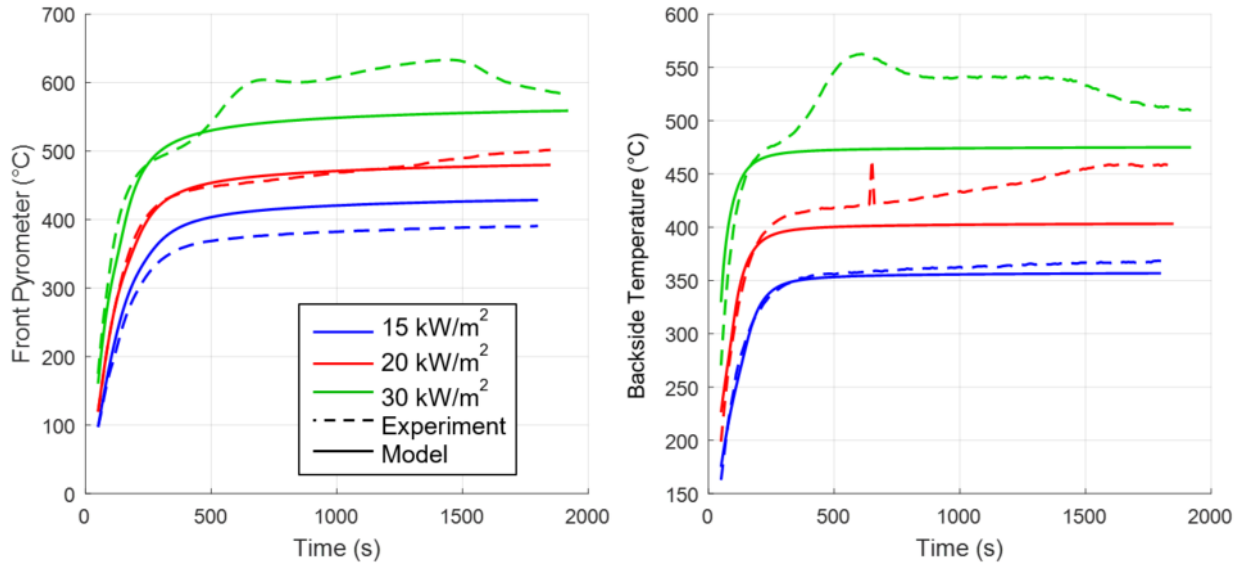
Figure 55. Predicted temperature response of FRP skins using optimized material properties from SCE optimization algorithm

The properties shown in Table 3 were used with a linear heating rate of 5 °C/min to develop equivalent temperature dependent thermal properties for the FRP skin that could be implemented in the simulation of Test Article 3b. The temperature dependent thermal conductivity and effective specific heat are provided in Figure 56.
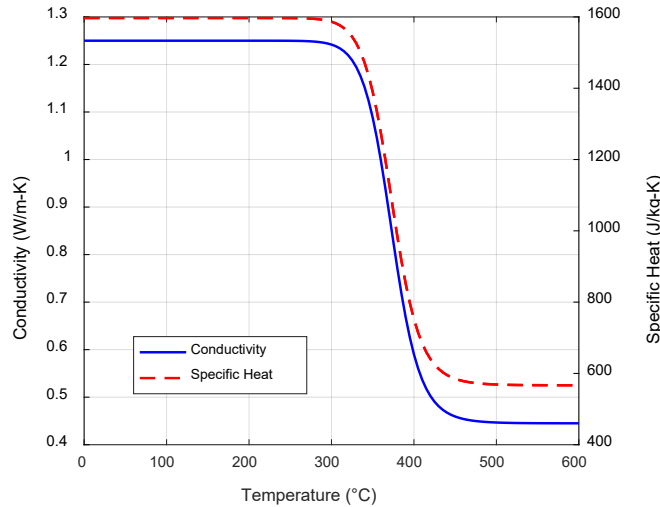
Figure 56. Effective temperature dependent thermal properties of FRP skin

6.4.2 Mechanical Tensile Testing

Uniaxial tensile testing of the FRP skins was conducted to develop updated strain-strain input data for the Phase III models. A detailed description of the testing parameters is provided in Section 6.1.3.1. A total of six tensile tests were conducted at room temperature. Photos of the test setup are shown in Figure 57.
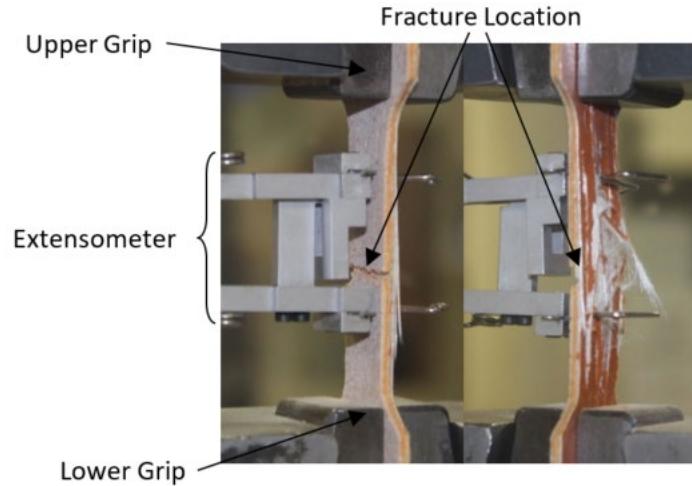
Figure 57. FRP skin tensile test setup and fracture test specimen

The measured stress-strain response of the FRP skin from the extensometer and load cell is provided in Figure 58. The elastic modulus was calculated to be 7.4 ± 0.9 GPa (1.07 ± 0.14 Msi). This is similar but slightly higher than the value of 7.0 GPa (1.02 Msi) used in the Phase I and Phase II models.
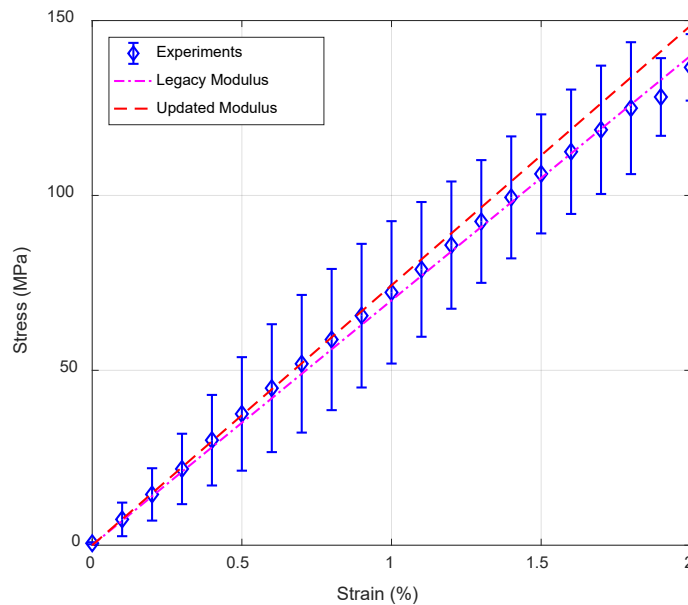
Figure 58. Measured stress-strain behavior of the FRP skins at room temperature along with predictions using legacy and updated material property values

6.5   FRP/Balsa Composite

Thermal and mechanical testing of the entire FRP/balsa sandwich composite was conducted to further develop and validate updated material models for the FRP skins and balsa core. Cone calorimeter testing was used to determine appropriate moisture content values for the balsa core and verify the balsa thermal properties. Furnace testing was used to verify the thermal properties of the FRP skin and balsa core as well as benchmark the material used in small-scale testing

65

against the large-scale testing conducted at SwRI. Lastly, mechanical testing of the entire sandwich composite was conducted at room temperature to develop updated mechanical properties for the balsa core.

6.5.1 Cone Calorimeter Testing

Cone calorimeter testing of the complete FRP/balsa composite was used to validate the thermal material model used for the balsa core. Like the ply-metal samples, the FRP/balsa samples were dried prior to testing by placing them in a 110 ºC oven for at least 24 hours prior to testing. The mass of the samples was measured before and after drying to obtain the moisture content of the balsa core. The measured moisture content of the balsa core was 13.2±2.3 percent. FRP/balsa samples were tested at four heat flux levels: 15, 20, 30, and 45 kW/m². No ignition occurred at any of the tested heat flux levels. The measured mass and thermal response from the cone calorimeter tests are provided in Figure 59. Note that different line styles denote repeats of nominally identical tests.
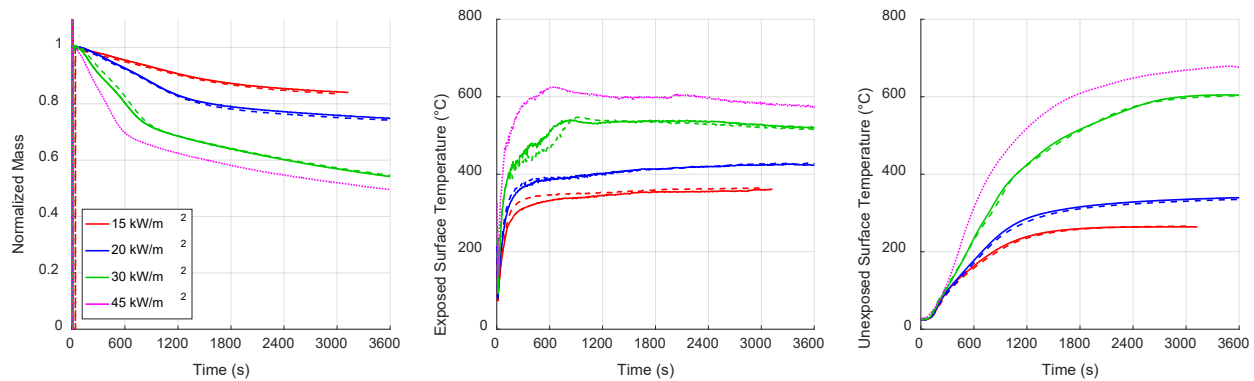
Figure 59. Measurements from cone calorimeter tests of FRP/balsa sandwich composite. Normalized sample mass (left), exposed surface temperature (center), and backside surface temperature (right)

The cone calorimeter experiments of the FRP/balsa composite were modeled using a one-dimensional heat transfer model in Abaqus. The thermal properties of the FRP skins discussed in Section 6.4.1.1 were applied to the model. The balsa core thermal properties obtained from the literature [5] and used in the pre-test models were used in this validation. The measured and predicted thermal response of the sandwich composite is shown in Figure 60. The model agrees well with the experimental data for the 15 kW/m² and 20 kW/m² exposures. The higher exposure models predict the exposed surface temperature well but under-predict the unexposed surface temperatures. The temperatures measured at these higher exposures are in excess of 500 °C.

At these temperatures, oxidation of the char begins to occur, which is a highly exothermic reaction. This energy generation within the core heats the unexposed surface to temperatures hotter than the exposed surface. This causes under-prediction of the unexposed surface temperature because energy generation within the core is not being accounted for in the model. These temperatures are not achieved in the large-scale experiments until near the end of the test duration. Because of this, the char oxidation reaction is not included in the current thermal material model being used to limit the model's complexity.

66
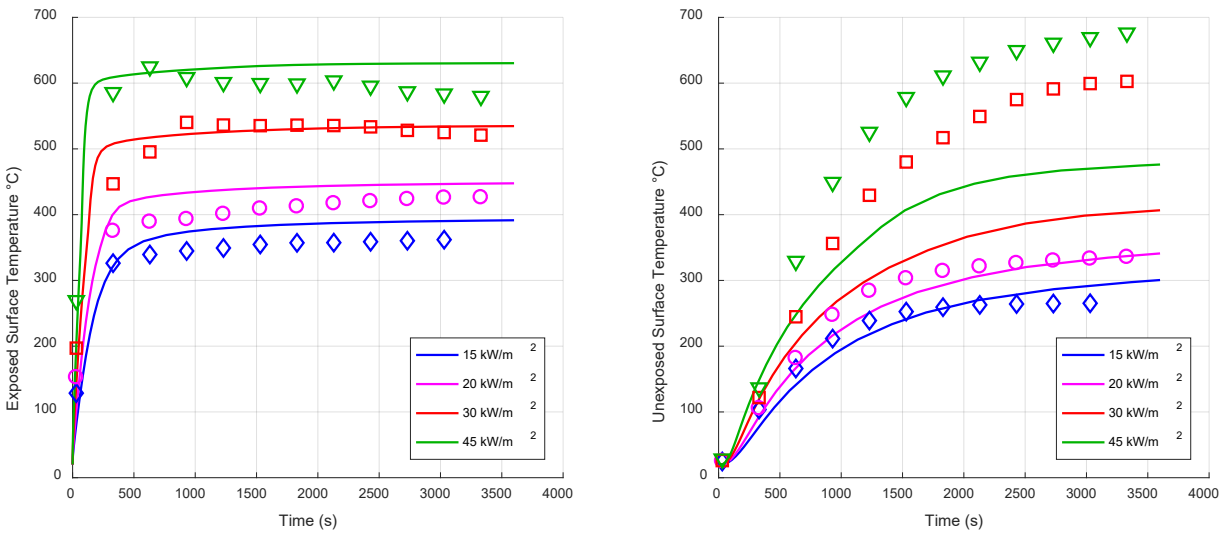
Figure 60. Predicted exposed surface (left) and backside temperature response of FRP/balsa sandwich composite under constant heat flux from cone calorimeter (right)

6.5.2 Furnace Testing

Two small-scale furnace tests were conducted using the FRP/balsa sandwich composite panels. Like, the ply-metal furnace tests, the purpose of these tests was to verify the material models for the FRP skin, balsa core, and fiberglass insulation as well as develop an estimate of the FRP skin surface emissivity using the method described in Section 6.1.2.

6.5.2.1 FRP/Balsa Furnace Testing Setup Details

The furnace tests conducted on the FRP/balsa composite panels were similar to those of the ply-metal panels described in Section 6.3.2. The first FRP/balsa furnace test consisted of an FRP/balsa panel shielded by 6.5 mm (0.25 in.) of ceramic fiberboard insulation and a 1.58 mm (0.063 in.) steel plate. This cross-section is shown in Figure 61. Temperature measurements were obtained on the back side of the exposed plate, the bottom of the ply-metal and the unexposed surface of the ply-metal. Note that temperature measurement locations are indicated by red circles in the figure. IR thermography was also obtained on the unexposed surface.
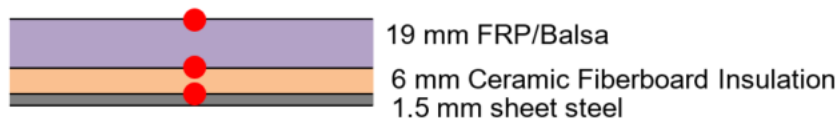
Figure 61. Cross-sectional details for insulated FRP/balsa panel test

The second FRP/balsa furnace test consisted of a one-dimensional mock-up of the alternative design railcar floor assembly tested at SwRI. This included a 1.58 mm (0.063 in.) steel plate on the exposed surface. Above that was 102 mm (4 in.) of fiberglass insulation and the FRP/balsa panel. The ply-metal panel was supported in the corners to allow the fiberglass insulation of degrade in the same manner observed in the large-scale tests. This cross-sectional detail is shown in Figure 62. Note that temperature measurement locations are indicated by red circles.
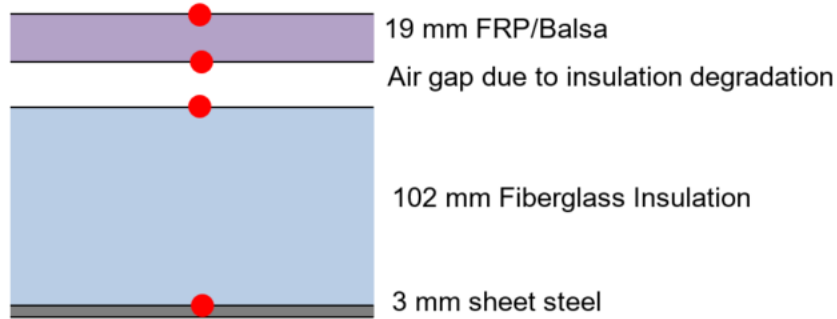
Figure 62. Cross-sectional details for full rail car floor alternative design mock-up with FRP/balsa panel

Like the ply-metal furnace experiments, one-dimensional models of the FRP/balsa experiments were also developed to validate the thermal properties developed using the cone calorimeter data and ensure consistency with the large-scale tests conducted at SwRI. The model layouts and meshes are shown in Figure 63. These simulations used the updated thermal properties of the FRP skins and the effects of the 13.2 percent moisture content on the thermal properties of the balsa core. The boundary conditions applied to these models were consistent with those applied to the simulations of Test Article 3b discussed in Section 4.4.
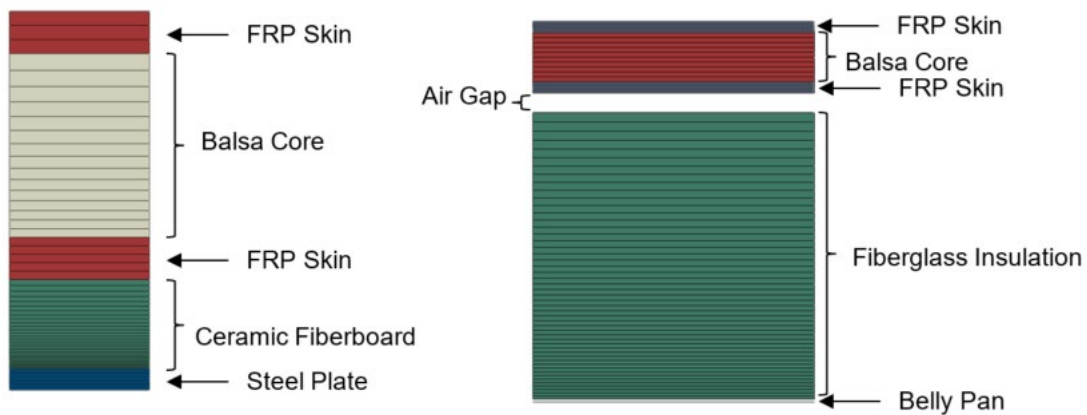
Figure 63. One-dimensional models of FRP/balsa furnace tests for panel protected by 6.35 mm (0.25 in.) of ceramic fiberboard insulation (left) and alternative design (Test Article 3b) mock-up (right)

6.5.2.2 FRP/Balsa Furnace Testing Results

The measured and predicted temperatures of the FRP/balsa panel shielded by the ceramic fiberboard insulation are provided in Figure 64. The temperature predictions at all three locations within the cross-section agree well with the experimental results. The predicted temperature rise of the unexposed surface of the FRP/balsa panel above 100 °C occurs approximately 400 seconds before the experimental measurement. This is likely because the moisture content in the tested panel was slightly higher than the 13.2 percent used in the simulation.
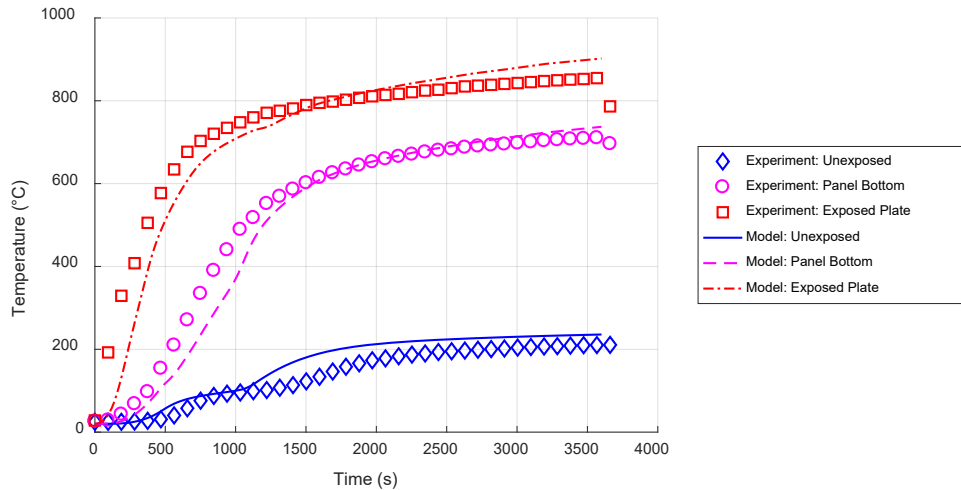
Figure 64. Measured and predicted temperatures of FRP/balsa composite panel protected by 6 mm (0.25 in.) of ceramic fiberboard insulation

The measured and predicted temperature response of the floor assembly mock-up of Test Article 3b is provided in Figure 65. Temperature prediction at the exposed surface agrees well with experimental measurements as expected from all the previously discussed models. The predicted temperature of the top surface of the insulation and the bottom of the FRP/balsa panel agree with experimental measurements for the first 20 minutes of exposure. Beyond 20 minutes, the temperature at these locations is generally under-predicted due to the known discrepancy between the legacy fiberglass insulation material used in the SwRI experiments and the updated material used in the Jensen Hughes experiment. However, these under-predictions did not have much impact on the unexposed surface temperature prediction. The accuracy of the unexposed surface temperature prediction indicates that the moisture content of 13.2 percent used in the simulation was accurate for this panel. This difference in moisture content between the two panels tested in the Jensen Hughes furnace is likely because the test samples were received already cut by the manufacturer and possibly came from two different fabricated panels.
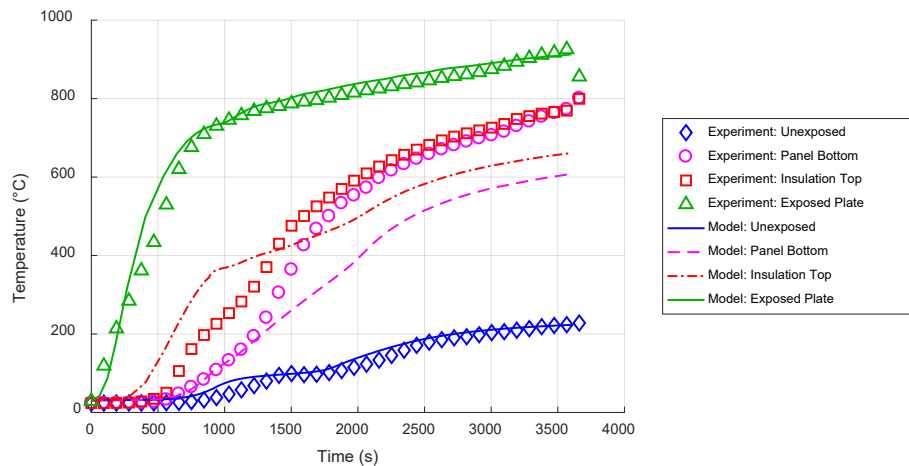
Figure 65. Measured and predicted temperatures of alternative design assembly mock-up including belly pan, fiberglass insulation, and FRP/balsa panel

69

6.5.3 Mechanical Compression Testing

Compression testing of the entire FRP/balsa sandwich composite cross-section was conducted to verify and possibly update the mechanical properties of the balsa core. Several iterations of the experiments were conducted resulting in four tests that produced acceptable quality results. The measured compression response from the experiments in provided in Figure 66. The measured bulk compressive modulus of the cross-section was 2.54 ± 0.25 GPa with compression failure loads ranging from 8–12 kN which equated to 17–25 MPa of compressive stress. This occurred at compressive strains of approximately 0.75 percent.
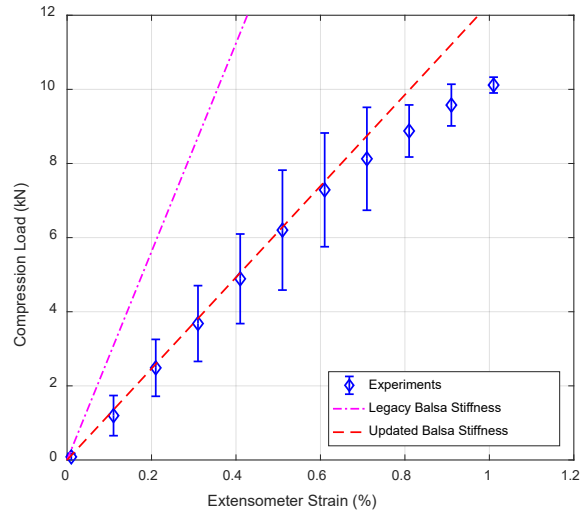
Figure 66. Measured and predicted compression behavior of FRP/balsa panel at room temperature

To verify the mechanical properties, a small FE model of the compression tests was created. The model included the geometry of the compression test sample represented in solid, three-dimensional elements. The geometry was meshed with 5 elements across the sample width and 50 elements along the length. Three elements were used through the thickness of each FRP skin and eight elements were used through the thickness of the balsa core. The compressive response was first predicted using the legacy balsa stiffness of 0.682 GPa is in the plane of the panel. This resulted in an over-prediction of the bulk stiffness as seen in Figure 66. The balsa stiffness was reduced to 0.23 GPa in the plane of the panel to bring the predicted compressive response in line with the measured values. A stiffness of 0.682 GPa across the grain of the balsa is in line with published values for high density balsa wood while a value of 0.23 GPa is in line with published values for low density balsa wood. According to the mass measurements taken for the cone calorimeter experiments, the density of the balsa used in this composite is approximately 150 kg/m^3 which is consistent with a low density balsa wood.

6.5.4 Mechanical Bending Testing

Bending testing of the full FRP/balsa composite cross-section was conducted to benchmark the updated mechanical properties for the FRP skin and balsa core. The measured bending response of the sandwich composite section is provided in Figure 67.
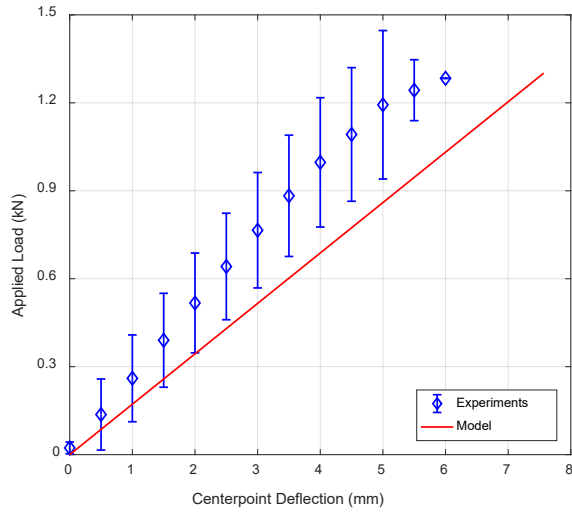
Figure 67. Measured and predicted bending behavior of FRP/balsa panel at room temperature

7.   Updated Material Modeling (Phase III Models)

The material models developed using the small- and intermediate-scale testing discussed in the previous section were implemented into the simulations of the large-scale tests at SwRI for the Phase III models. Additionally, the Phase III models included creep of the steel components within the floor assemblies. This included the steel frame and ply-metal skins of Test Articles 1, 2, and 3a along with the steel frame of Test Article 3b. A strain-hardening, primary and secondary creep model was implemented into the Phase III models based on published data and creep model parameters [13]. The following section discusses which material model updates were applied to each simulation and the resulting impact on the predicted thermal and mechanical response of the floor assembly compared to the experimental measurements.

7.1   Test Article 1: Full-Scale Transverse Supports

The Phase III model for Test Article 1 implemented the updated thermal material model for the plywood core of the ply-metal composite. Also, the updated model included the creep behavior of the steel frame and ply-metal skins. These two material model updates are the only changes between the Phase II and Phase III models of Test Article 1.

7.1.1   Updated Model Results

A comparison of the measured thermal response of Test Article 1 to the predictions of all three phases of modeling is shown in Figure 68. The impact of the updated plywood thermal model can clearly be observed in the unexposed surface temperature. This suggests the actual moisture content in plywood was lower than the assumed value of 15 percent because the higher assumed moisture content results in higher thermal conductivity below 100 °C. The updated temperature prediction at the bottom of the ply-metal is lower than the experiment. This is attributed to how the moisture in the plywood is modeled. In the actual test article as moisture at the bottom of the plywood core evaporates, the steam travels away from the heated surface lowering the specific heat capacity at the bottom of the core. This phenomenon is not captured using effective thermal properties, which result in a predicted short pause in heating at 100 °C that is not observed in the experimental measurement. The predicted temperatures in the insulation, belly pan, and internal structural members from the Phase III model is similar to the Phase II models. This is expected as no changes to the material thermal models of steel and fiberglass were made.

The predicted mechanical response of Test Article 1 from all three modeling phases is shown in Figure 69 along with the experimental measurements. The predicted response from the Phase III model is similar to the Phase II model. This is expected because the predicted thermal response from these two phases of modeling is similar over the first 1,800 seconds of exposure. Thus, the property degradation response is similar. While Phase III models also include steel creep, temperatures in the structural elements have not experienced high enough temperatures for a long enough duration to generate significant creep strains. Note that the small discontinuity in the predicted structural response from the Phase III model at 730 seconds is the result of a bifurcation event in the belly pan. The small discontinuities between 1,300 and 1,400 seconds are a result of local deformation of the ends of the side sill at the support locations. The rapid nature of these events is an artifact of the idealized nature of modeling and would be expected to occur over longer periods during an experiment.
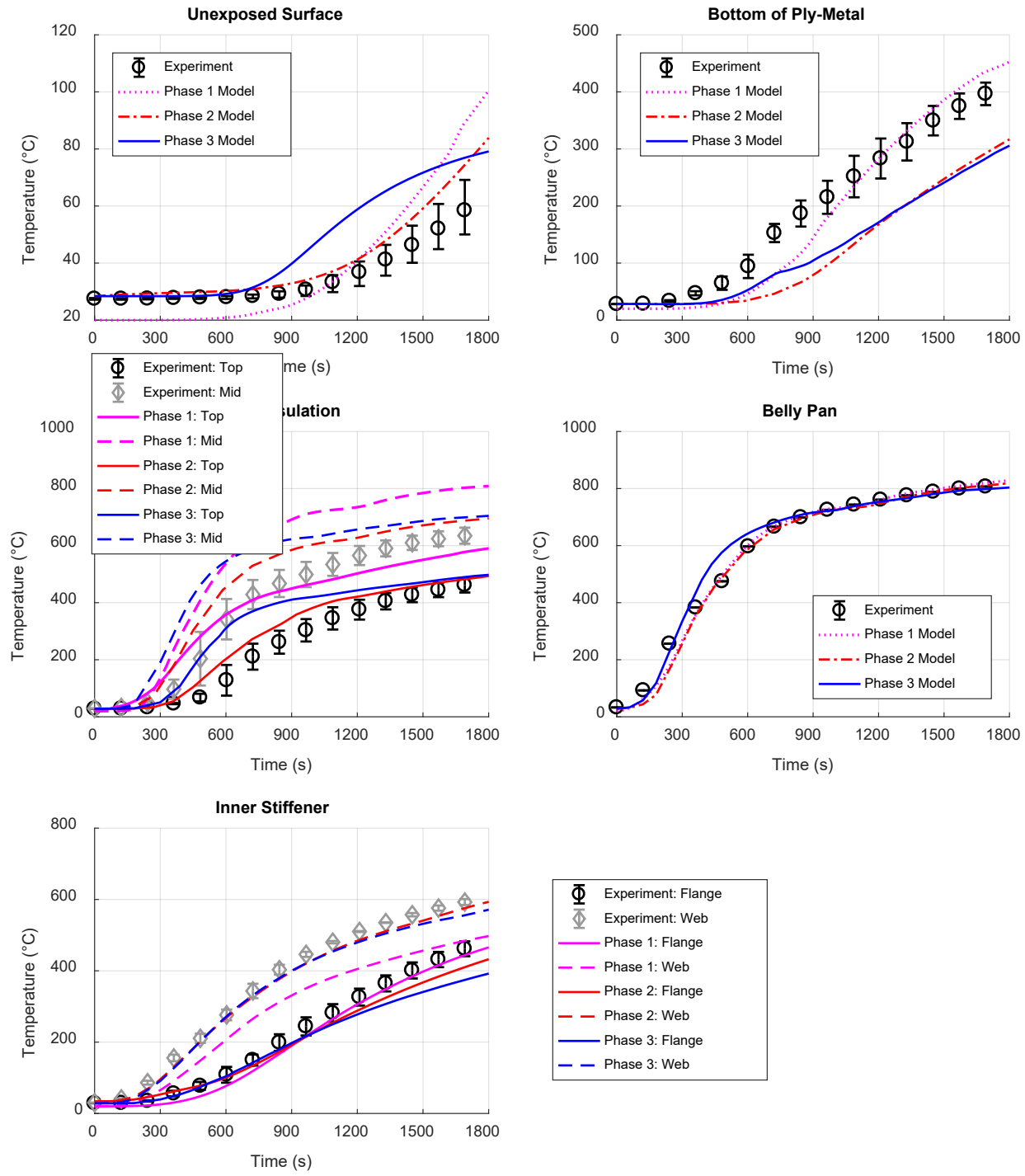
Figure 68. Measured thermal response of Test Article 1 under ASTM E119 exposure conditions as well as predicted thermal response from all three phases of models

73
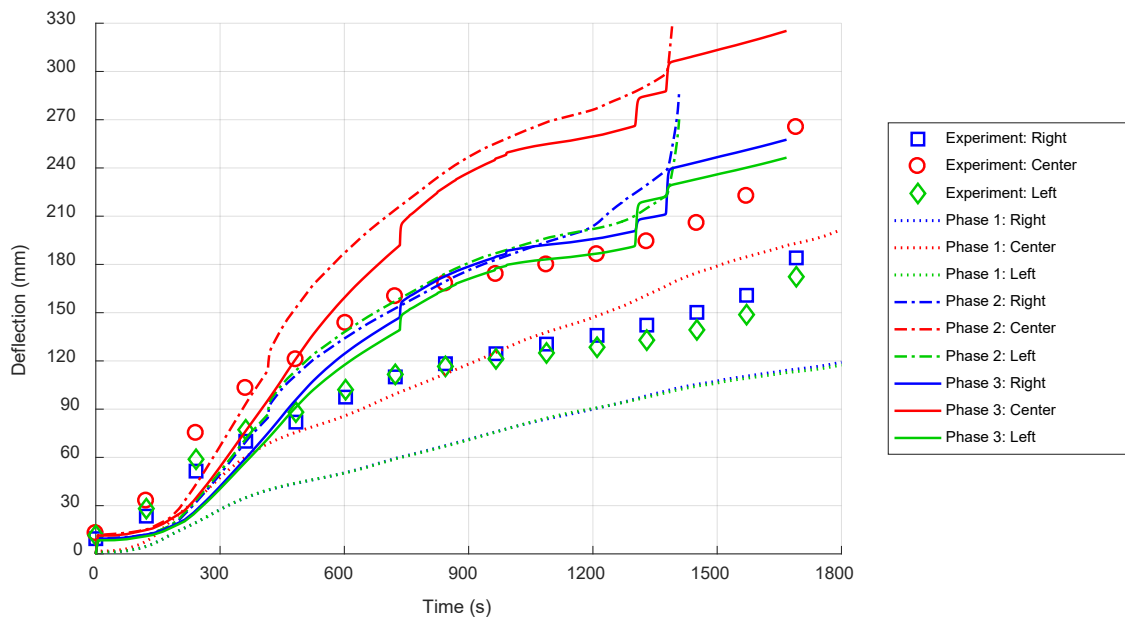
Figure 69. Measured structural response of Test Article 1 under ASTM E119 exposure conditions as well as predicted thermal response from all three phases of models

7.2   Test Article 2: Full-Scale Longitudinal Supports

The Phase III model for Test Article 2 implemented the updated thermal material model for the plywood core of the ply-metal composite. Also, the updated model included the creep behavior of the steel frame and ply-metal skins. These two material model updates are the only changes between the Phase II and Phase III models of Test Article 2.

7.2.1 Updated Model Results

The updated thermal prediction of Test Article 2 is shown in Figure 70 in comparison to the previous modeling phases and the experimental measurements. Like in Test Article 1, the impact of the moisture content in the plywood can clearly be seen in the predicted unexposed surface temperature. With this inclusion, the predicted thermal behavior of the unexposed surface agrees with the experimental observation. This also suggests that the assumed 15 percent moisture content was appropriate for Test Article 2. The predicted temperature at the bottom of the ply-metal is lower than measurement due to effective property approach to capture the moisture content as described in Section 6.1.1. Like the models for Test Article 1, the predicted insulation, belly pan, and inner structural member temperature response from the Phase III model is similar to the Phase II model since no changes were made to the material thermal models for the fiberglass insulation and steel.

A comparison of the measured deflection and the predicted deflection from all three modeling phases is shown in Figure 71. The deflection response is generally slightly under-predicted by the Phase III model when compared to the experimental measurement. This is attributed to the general under-prediction of the bottom of the ply-metal and top of the internal transverse stiffeners. The Phase III prediction does, however, exhibit the initial increase in deflection followed by a reduction in the deflection rate around 1,200 seconds and then an increase in

74

deflection at the onset of failure. The predicted deflection is shown to 3,450 seconds at which time structural failure of the assembly was predicted. At 3,450 seconds, the simulation was unable to converge to a solution indicating that the assembly has lost its ability to carry the applied load. This is consistent with the observed structural failure of the assembly at 2,750 seconds in the large-scale experiment.
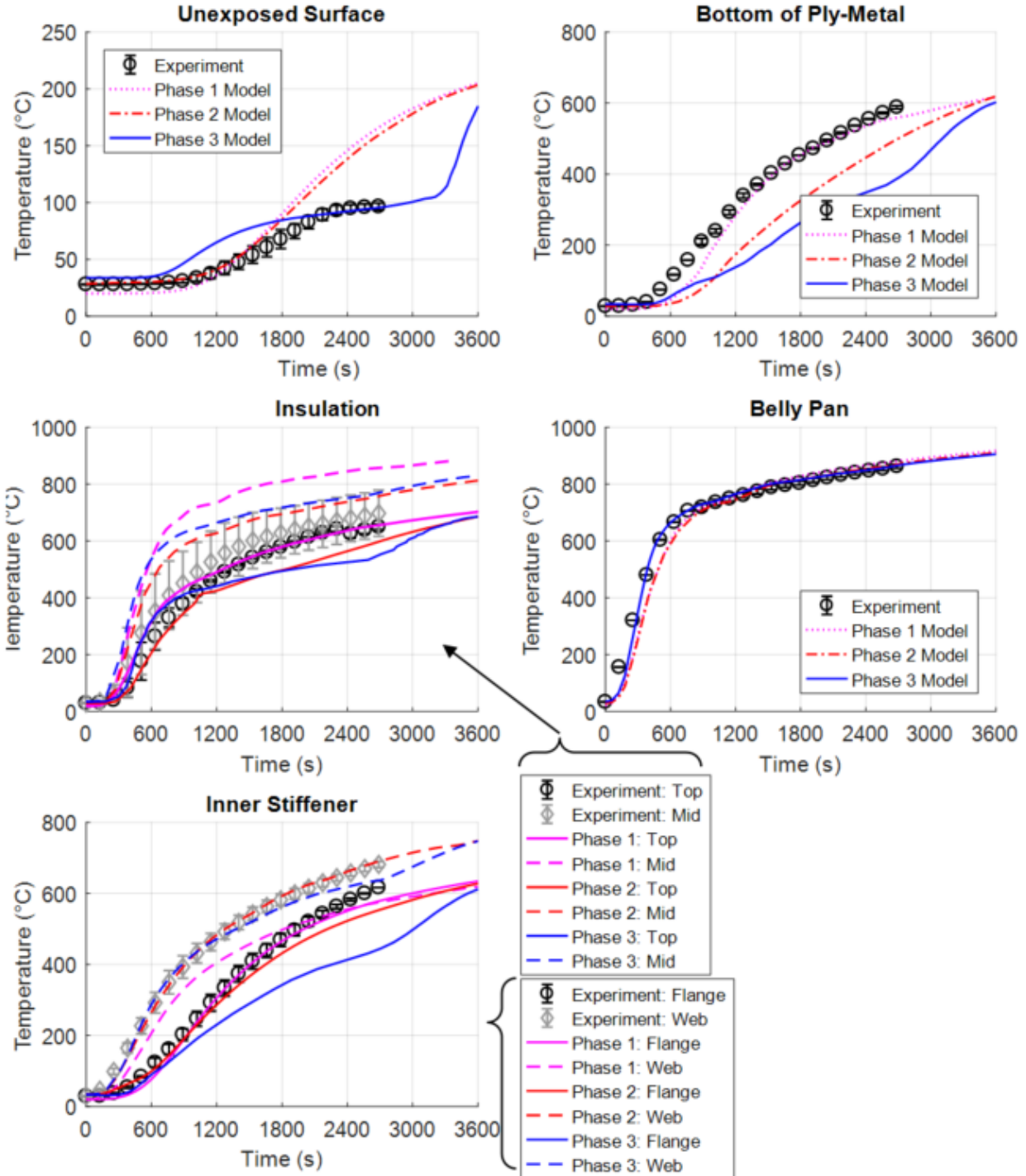
Figure 70. Measured thermal response of Test Article 2 under ASTM E119 exposure conditions as well as predicted thermal response from all three phases of models
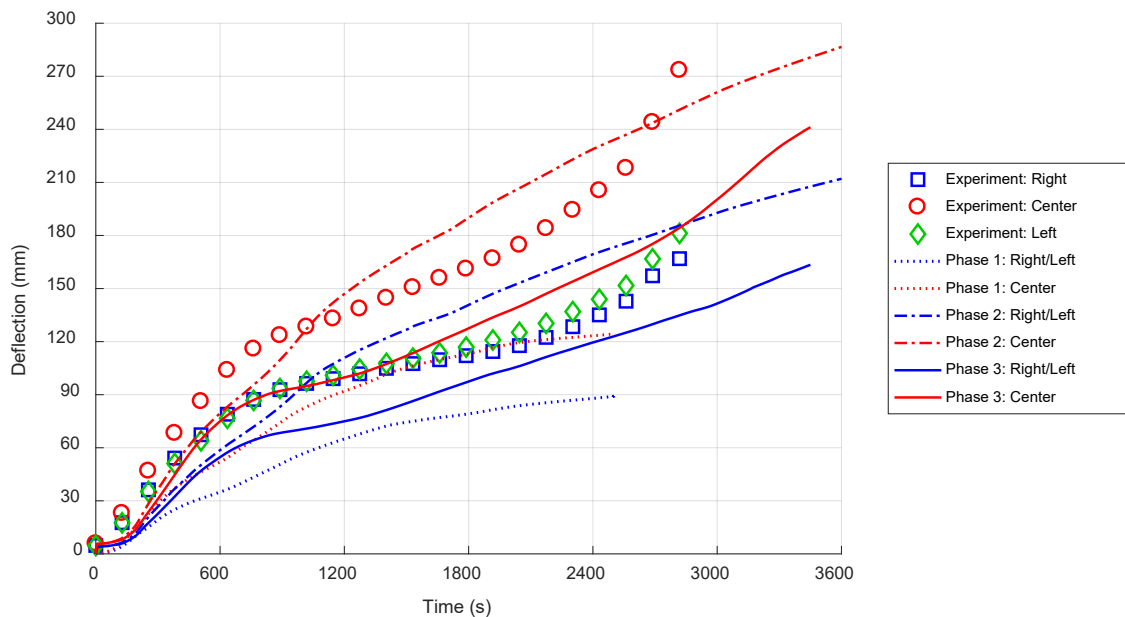
Figure 71. Measured structural response of Test Article 2 under ASTM E119 exposure conditions as well as predicted thermal response from all three phases of models

7.3   Test Article 3a: Reduced Scale Longitudinal Supports

The Phase III model for Test Article 3a implemented the updated thermal material model for the plywood core of the ply-metal composite. Also, the updated model included the creep behavior of the steel frame and ply-metal skins. These two material model updates are the only changes between the Phase II and Phase III models of Test Article 3a.

7.3.1   Updated Model Results

The predicted thermal response of Test Article 3a from all three phases of modeling is shown in Figure 72 along with the experimental measurements. The predicted thermal response of the unexposed surface from the Phase III model generally agrees with the experimental measurement with a long pause in heating at 100 °C with the onset of a rapid heating phase within the last 300 seconds of the 60-minute exposure. Like the predictions for Test Articles 1 and 2, the temperature of the bottom surface of the ply-metal panel is underpredicted and the temperature predictions in the insulation, belly pan, and steel frame from the Phase III model are similar to the Phase II model predictions.

A comparison between the predicted deflection response of Test Article 3a and the measured values is provided in Figure 73. The predicted deflection behavior from the Phase III model is similar to the Phase II model for the first 2,400 seconds. The differences up to 2,400 seconds are attributed to the difference in the predicted thermal response of the ply-metal panel. Beyond 2,400 seconds, the Phase III model predicts an increase in deflection rate that is not observed in the Phase II model prediction. This is attributed to the inclusion of the creep strains in the steel frame in the Phase III model. This increase is also consistent with the experimental measurements and indicative of the onset of structural failure of the test article as observed in the experiments for Test Articles 1, 2, and 3b.

76
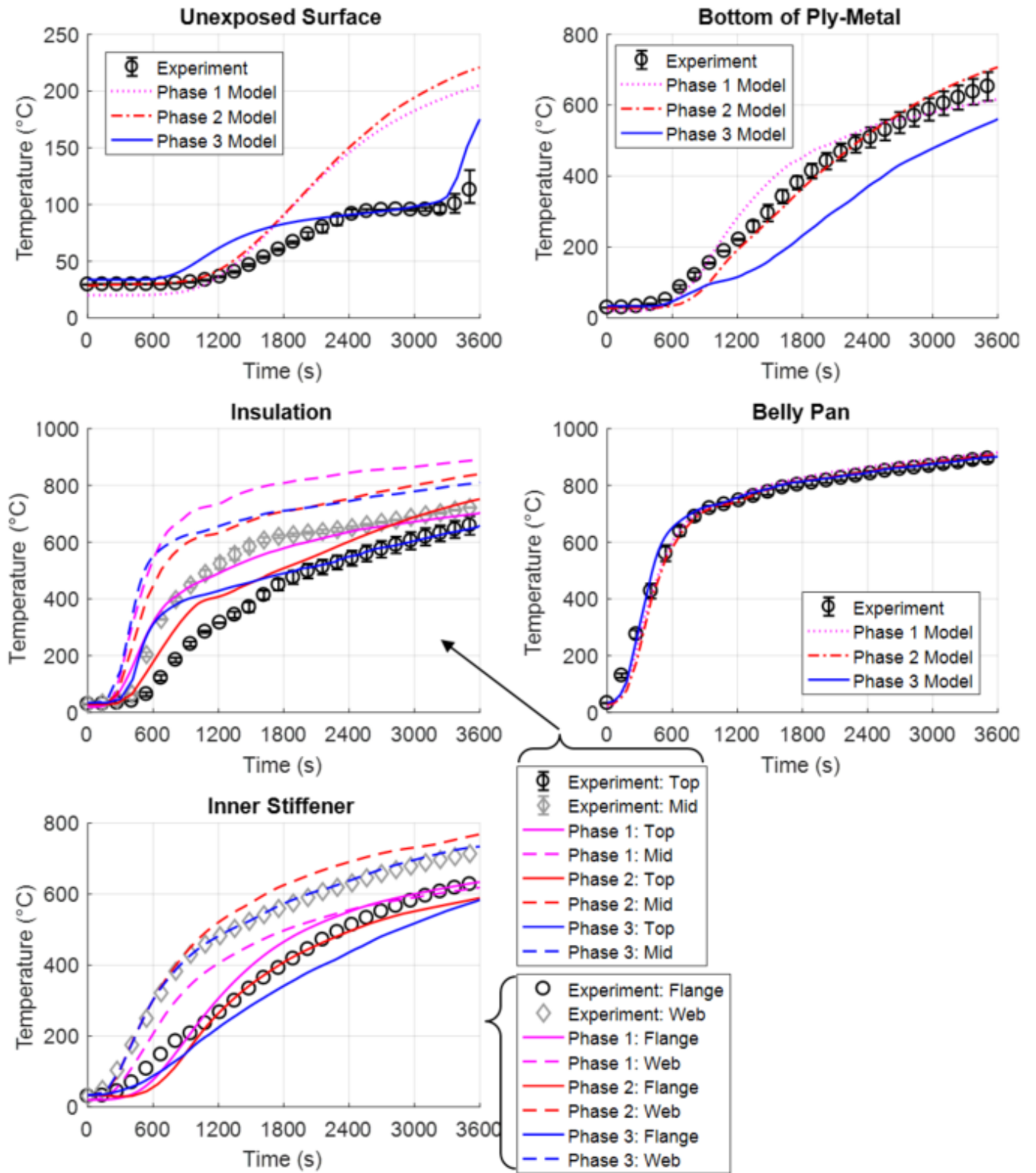
Figure 72. Measured thermal response of Test Article 3a under ASTM E119 exposure conditions as well as predicted thermal response from all three phases of models
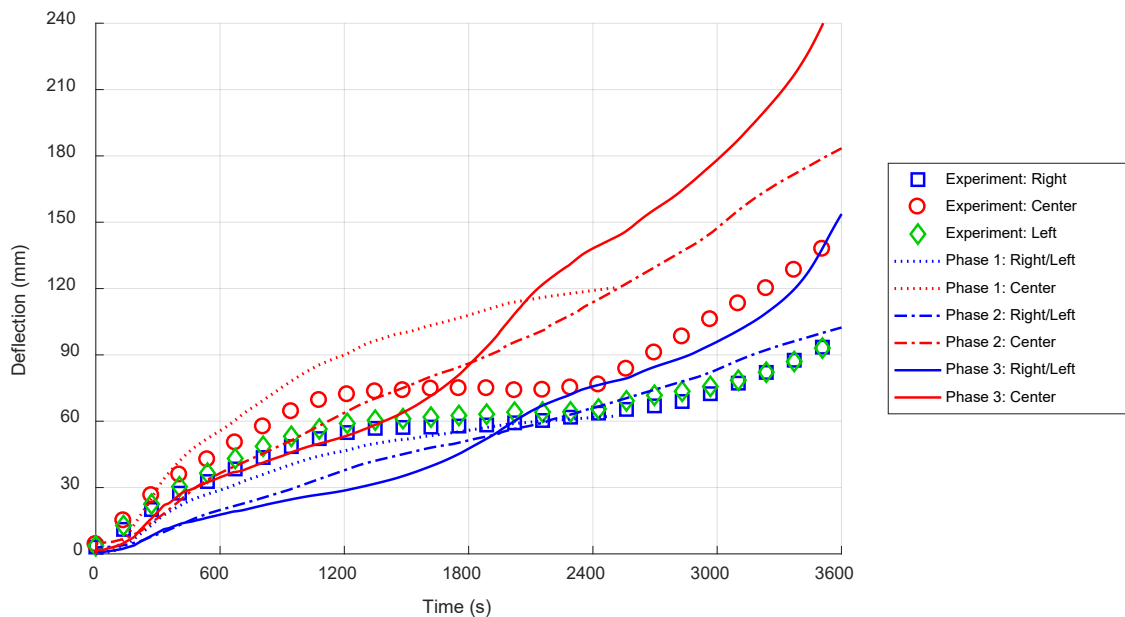
Figure 73. Measured structural response of Test Article 3a under ASTM E119 exposure conditions as well as predicted thermal response from all three phases of models

7.4 Test Article 3b: Reduced Scale Alternative Design

The Phase III model for Test Article 3b implemented several updated material models. The first is the updated thermal material model for the FRP skin of the FRP/balsa composite panel. The thermal material model for the balsa core was modified to include the effects of moisture content. The mechanical material model for the FRP skin was also updated to include a more accurate modulus. The mechanical material model for the balsa core of the FRP/balsa composite was also updated. Note that the mechanical material models for the FRP and balsa still did not include non-linear behavior beyond the onset of failure. However, the stresses in the Phase III models were compared to failure stresses measured during the small-scale experiments to validate when mechanical failure of the panels was expected. The material model for the underlying steel frame was updated to include the effects of creep strains at high temperatures. Lastly, Phase III model of Test Article 3b included the impact of thermocouple pads on the unexposed surface temperature. This effect is significant for the Test Article 3b unexposed surface temperature measurement because the unexposed surface temperature was significantly higher at the time of failure than the other test articles. However, it does not impact the structural response because only a small area of the floor panel is covered by the thermocouple pads.

7.4.1 Updated Model Results

A comparison of the measured thermal response of Test Article 3b to the predicted response at all three phases of modeling is provided in Figure 74. The unexposed surface temperature prediction from the Phase III model is significantly more accurate than the earlier phases when compared to the measured response. The most influential factor to this change in predicted response is the inclusion of the moisture content effects in the balsa core. These effects caused the increased heating rate for the first 20 minutes of exposure and the pause in heating at 100 °C as the moisture within the core evaporated. Also, inclusion of the thermocouple pad effects

78

contributed to an increase in predicted temperature beyond 40 minutes when the unexposed surface temperature was above 300 °C. The peak unexposed surface temperature of the other test articles was less than 150 °C so the thermocouple pads did not need to be explicitly included to accurately model the thermal response at the thermocouple locations.

The predicted temperature at the bottom of the FRP/balsa panel was still below the experimentally measured value. This under-prediction is due to the necessary simplification of the moisture content effects in the balsa core. In the experimental exposure, bulk movement of water vapor from the exposure surface to the unexposed surface allows the exposed surface to dry and heat more rapidly. While the representation of the moisture content using effective conductivity and specific heat values can capture the moisture content effects to a degree, it cannot capture this phenomenon. Temperature predictions within the insulation and at the belly pan of the assembly were consistent between all three phases of models. This is expected as no significant change was made to the thermal material models for the steel frame and fiberglass insulation.

Temperature predictions of the internal steel member web and flange were higher for Phase III models and more similar to experimental measurements. The updated conductivity and specific heat capacity of the FRP skin made the skin more insulating at the contact between the steel frame and the FRP/balsa panel. This increased degree of insulation at the top of the internal steel stiffeners resulting in higher predicted steel temperatures.

The predicted structural response for all three phases of models for Test Article 3b is shown in Figure 75. The predicted structural response is similar for the Phase II and Phase III models for the first 20 minutes of exposure. This signifies that the changes in the material mechanical models for the FRP skins and balsa core did not have significant impact on the predicted structural response. Beyond 20 minutes, the predicted structural response diverges with the Phase III models predicted failure at approximately 30 minutes. This is approximately 33 percent faster than the experimentally observed failure times. Upon review of photographs taken of the underside of Test Article 3b within the SwRI furnace, it was determined that some shielding of the transverse ends of the test article occurred similar to that of Test Article 3a. The impact of that shield was explored and is discussed in Section 5.3.
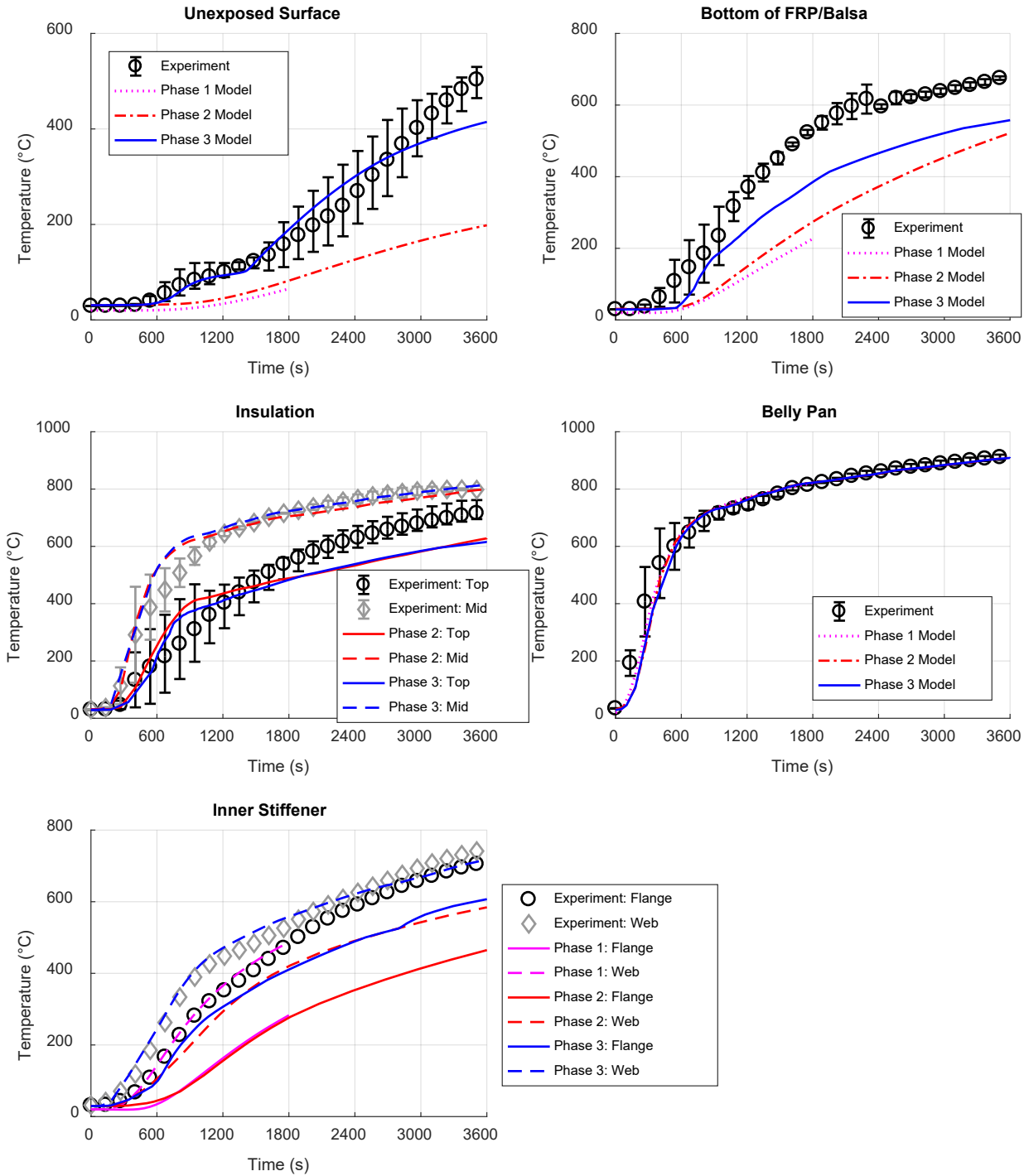
Figure 74. Measured thermal response of Test Article 3b under ASTM E119 exposure conditions as well as predicted thermal response from all three phases of models
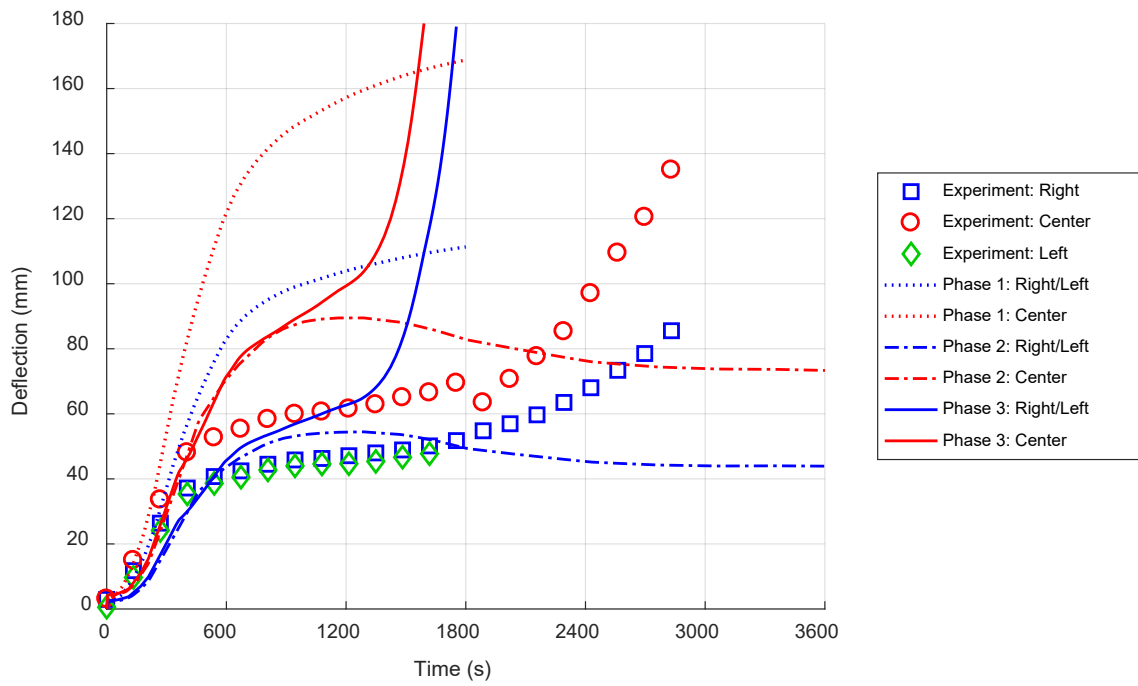
Figure 75. Measured structural response of Test Article 3b under ASTM E119 exposure and loading conditions as well as predicted structural response from all three phases of models

8. Discussion

Test Articles 2 and 3a contained identical structures across the longitudinal span of the floor assembly. The primary difference was that the Test Article 2 (full-scale test article) contained three repetitions of the structural frame, while Test Article 3a (reduced-scale test article) only contained a single repetition. Previous modeling of a nearly identical floor assembly suggested that the reduction in the structural repetitions between Test Article 2 and Test Article 3a should not have impacted the thermal response and subsequent structural response of the test assemblies. The measured thermal responses of these two test articles were similar. However, the measured structural response of the assemblies was significantly different, with Test Article 2 undergoing structural failure after approximately 45 minutes of exposure while Test Article 3a did not structurally fail during the 60-minute exposure. The below sections discuss two of the primary difference between the boundary conditions of these two tests that contributed to the difference in the structural responses.

8.1 Test Article Shielding Effects

One of the primary contributors to the difference between the experimentally observed deflection behavior of Test Articles 2 and 3a was attributed to the thermal shielding of the transverse ends of the test articles. When the longitudinal size of the test article is reduced, the mechanical response of the test article becomes more sensitive to edge effects. The impacts of this thermal shielding were observed in both Test Articles 3a and 3b. The impact of this shielding is best observed through a sensitivity analysis of Test Article 3b.

Figure 76 contains the predicted structural response of the Test Article 3b with varying amounts of thermal shielding at the transverse ends of the test article. Without any shielding of the transverse ends, failure of the test article is predicted to occur at approximately 1,800 seconds. If the outer 51 mm (2 in.) of the transverse ends of the test article are shielded from the furnace exposure, the predicted failure time increases to approximately 2,000 seconds. Further increasing the shielding to 102 mm (4 in.) increases the predicted failure time to approximately 3,300 seconds. The large difference between the predicted failure times for 51 mm (2 in.) of shielding and 102 mm (4 in.) of shielding is because the webs of the transverse stiffeners at the transverse ends are 51 mm (2 in.) from the end to the test article. Based on these results, it appears that the shielding of Test Article 3b in the large-scale experiment was equivalent to 76–102 mm (3–4 in.) at the transverse ends. This is reasonable given the configuration of the shielding for this test article shown in Figure 77. Transverse ends can be seen on the left side of the image at the center sill.

82
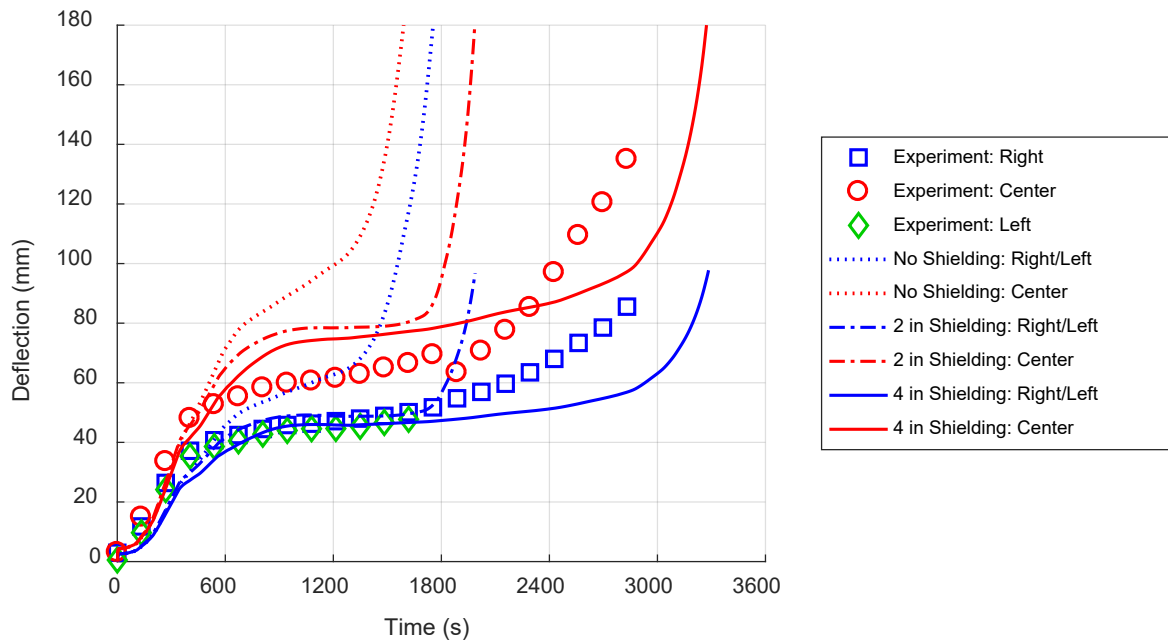
Figure 76. Effects of thermal shielding at the transverse ends of Test Article 3b on the predicted structural performance during an ASTM E119 test

Figure 77. Exposed surface of Test Article 3b just prior to testing

8.2   Test Article Confinement Effects

The second contributor to the difference between the observed behavior of Test Articles 2 and 3a is the transverse confinement caused by the steel support frame. When supporting the test article, care must be taken to ensure that confinement of the test article is not generated. This is simple when the test article is simply supported by the furnace structure. If a built-up frame is used to support the test article, ensuring confinement from thermal expansion does not occur can be more difficult. Confinement of the test article at scale tested in this work has a significant impact on the mechanical response of the test article. Permanent deformation profiles for the nominally

identical test article with and without transverse confinement is shown in Figure 78 following 1,800 seconds of exposure ASTM E119. Note that only half the test article is shown in this figure for clarity. The locations with the largest difference between the unconfined and confined response is at the transverse ends of the transverse stiffeners. Significant plastic strain is generated at these locations with the test article is confined. Additional plastic strain is also generated at the center of the transverse members due to the confinement. It is this increased plastic strain, which is a result of increased compressive stresses in these members, that caused the structural failure of Test Article 2 as seen in Figure 10.
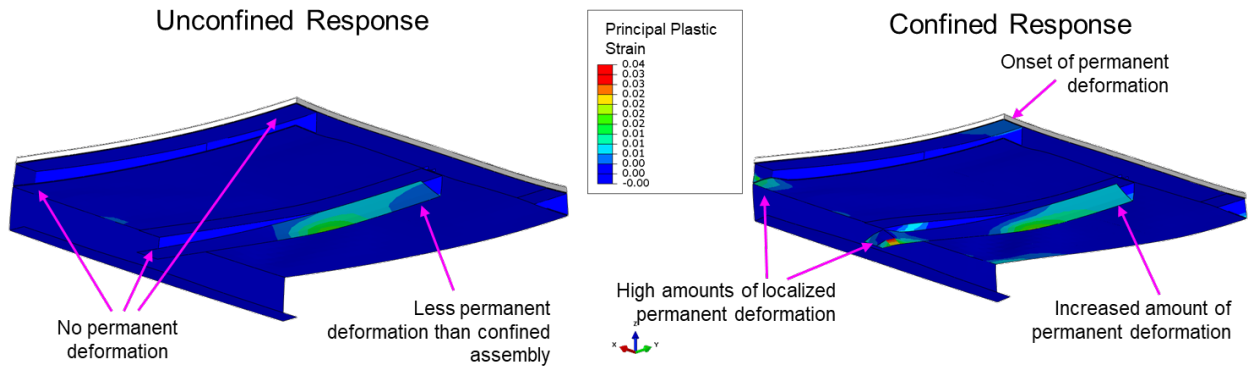
Figure 78. Permanent deformation profiles of unconfined and transverse confined test articles following 1,800 seconds of ASTM E119 thermal exposure with applied structural load

9. Conclusion

This research is part of a continuing effort to explore the feasibility of reducing the size requirements for large-scale fire resistance testing required by NFPA 130. A previous phase of this research developed a methodology to reduce the longitudinal size of test articles. This methodology was based solely on thermal and mechanical computer simulations of rail car floor assemblies ranging from full rail cars to reduced-scale test articles. This effort developed and executed a large-scale test series to help validate and further investigate the feasibility of the previously developed methodology. It then expanded on the preliminary modeling effort to explore the sensitivity of the thermo-structural response of test articles to the size reduction methodology.

9.1 Findings

The experimental methodology consisted of four test articles tested in three experiments: Two individually tested full-scale test articles which met the size requirements of NFPA 130 and two reduced-scale which were concurrently tested in the same furnace. The thermal performance of the test articles was as expected at the measurement locations near the center. However, the mechanical performance was not as expected due to a combination of unintended shielding at the transverse ends of the test articles and unintended confinement in the transverse direction caused by the assembly support frame.

A series of three iterations of simulations were developed for each of the tested assemblies. The first, pre-test, simulations were unaffected by the test results and contained discrepancies between the theoretical assemblies and the actual constructed versions. These discrepancies resulted in several differences between the predicted and measured results. A second iteration of models was developed to address these discrepancies and include phenomena that were observed during the experiments. Continued differences between the models and experiments were attributed to uncertainty in the material models used for the fiberglass insulation, plywood core, FRP skins, and balsa core.

Small- and intermediate-scale experiments designed to obtain more accurate thermal and mechanical material properties for the floor assembly materials were then conducted. These tests highlighted an undocumented change in fiberglass insulation material made in 2017 that impacted the fire performance of the floor assemblies. They also resulted in updated thermal and mechanical property inputs for several of the materials used in the floor assemblies.

The final iteration of simulations included the updated material property data obtained from the small- and intermediate-scale tests. These models generally predicted the thermal and structural response of the large-scale test assemblies well. These models were also used to explore the impact of thermal shielding at the edge of the test assembly and transverse confinement of the expected thermal and structural response of the reduced-scale floor assembly. In general, this work highlighted challenges with the execution of reduced-scale testing but did not find any fundamental problems with the previously developed methodology for reducing the physical size of the fire resistance test articles.

9.2   Recommendations

Given that the research did not discover underlying flaws with the previously developed size reduction methodology, there are two primary tasks that would provide confidence in the application of the methodology within the rail car industry. The first of these tasks is to successfully apply the scaling methodology to a more diverse range of rail car floor structures. The actual design of railcar floors can have different configurations of primary and secondary longitudinal and transverse structures. The scaling methodology aims to more realistically capture the end-use boundary conditions of the test articles in the full rail car. The alternative boundary conditions used to scale the floor assembly were able to represent this well for the exemplar rail car used for the first three test articles. The end-use conditions were not captured as well for the alternative design. A larger array of typical rail car floor structure configurations would provide confidence that the reduced-scale test articles can represent the end-use structural boundary conditions across the array of designs used in industry.

The second recommended task is to conduct additional reduced-scale testing. This would further validate and benchmark the scaling methodology and continue to identify and address challenges in obtaining reduced-scale test performance that is indicative of full-scale test articles and, ultimately, end-use conditions. The large-scale tests conducted so far as part of this research have identified two challenges with executing the reduced-scale tests. First is ensuring that confinement of the test article is not created by any support frame used to provide physical support of the test article. Second is ensuring that the transverse ends of the test article remain fully exposed to the furnace interior while maintaining a seal around the edges to prevent smoke and hot gases from escaping around the test article. Additional reduced-scale testing will provide recommendations on mitigating these difficulties and possibly uncover other difficulties and associated mitigations.

10. References

[1] Kapahi, A. et al., "Evaluation of Rail Car Floor Fire Resistance Exposure and Test Article Scaling," U.S. Department of Transportation, Federal Railroad Administration, Technical Report No. DOT/FRA/ORD-18/38, Washington, DC, 2018.

[2] The European Union: Edict of Government, "EurocodE 3: Design of steel structures - Part 1-2: General rules - Structural fire design [Authority: The European Union Per Regulation 305/2011, Directive 98/34/EC, Directive 2004/18/EC]," EN 1993-1-2, The European Union, 2005.

[3] Fateh, T., Rogaume, T., & Richard, F., "Multi-scale modeling of the thermal decomposition of fire retardant plywood," *Fire Safety Journal,* vol. 64, p. 36–47, 2014.

[4] The European Union: Edict of Government, "Eurocode 1: Actions on structures - Part 1-2: General actions - Actions on structures exposed to fire [Authority: The European Union Per Regulation 305/2011, Directive 98/34/EC, Directive 2004/18/EC]," EN 1991-1-2, The European Union, 2002.

[5] Couchman, L. S., & Mouritz, A. P., Modeling of naval composite structures in fire, Melbourne, Australia: U.S. States Naval Academy, Cooperative Research Centre for Advanced Composite Structures, 2006.

[6] Duan, Q. Y., Gupta, V. K., & Sorooshian, S., "Shuffled complex evolution approach for effective and efficient global minimization," *Journal of Optimization Theory and Applications,* vol. 76, p. 501–521, 1993.

[7] Duan, Q., Sorooshian, S., & Gupta, V. K., "Optimal use of the SCE-UA global optimization method for calibrating watershed models," *Journal of Hydrology,* vol. 158, p. 265–284, 1994.

[8] Yang, F., Rippe, C., Hodges, J., & Lattimer, B., "Methodology for material property determination," *Fire and Materials,* vol. 43, no. 1, 2019.

[9] Chaos, M., Khan, M. M., Krishnamoorthy, N., de Ris, J. L., & Dorofeev, S. B., "Evaluation of optimization schemes and determination of solid fuel properties for CFD fire models using bench-scale pyrolysis tests," in *The Combustion Institute*, 2011.

[10] Ding, Y., Wang, C., Chaos, M., & Chen R., "Estimation of beech pyrolysis kinetic parameters by Shuffled Complex Evolution," *Bioresource Technology,* vol. 200, p. 658–665, 2015.

[11] Cholewa, N., Summers, P. T., Feih, S., Mouritz, A. P., Lattimer, B. Y., & Case, S. W., "A Technique for Coupled Thermomechanical Response Measurement Using Infrared Thermography and Digital Image Correlation (TDIC)," *Experimental Mechanics,* vol. 56, p. 145–164, 2016.

[12] Richter, F., & Rein, G., "Pyrolysis kinetics and multi-objective inverse modelling of cellulose at the microscale," *Fire Safety Journal,* vol. 91, 2017.

[13] Fields, B. A., & Fields, R. J., "Elevated Temperature Deformation of Structural Steel," U.S. Department of Commerce, National Institute of Standards and Technology, Metallurgy Division, Gaithersburg, MD, 1989.

Appendix A.
Simulation Material Models

A1. Carbon Steel

The density of carbon steel used for all models was 7,850 kg/m³.
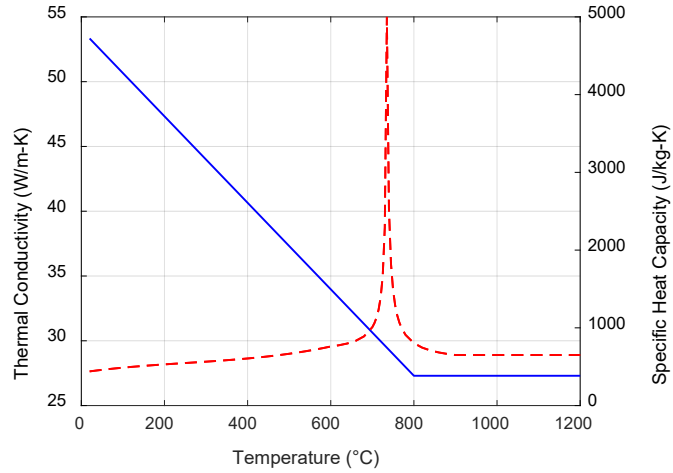
Figure A1. Temperature dependent thermal properties of carbon steel
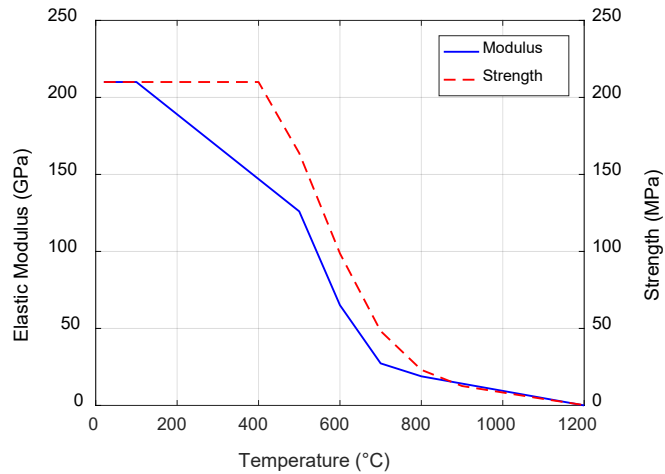
Figure A2. Temperature dependent mechanical properties of carbon steel

Table A1. Creep parameters for carbon steel

Temperature (°C)	Coefficient (/s)	Time Exponent	Stress Exponent
350	1.00E-99	1	1
400	1.61E-43	4.66	0.3
450	2.64E-46	4.98	0.475
500	4.03E-49	5.3	0.65
550	3.40E-51	5.62	0.825
600	2.86E-53	5.94	1
650	2.42E-55	6.26	1.175

A2. Plywood

The density of plywood used for all models was 480 kg/m^3.
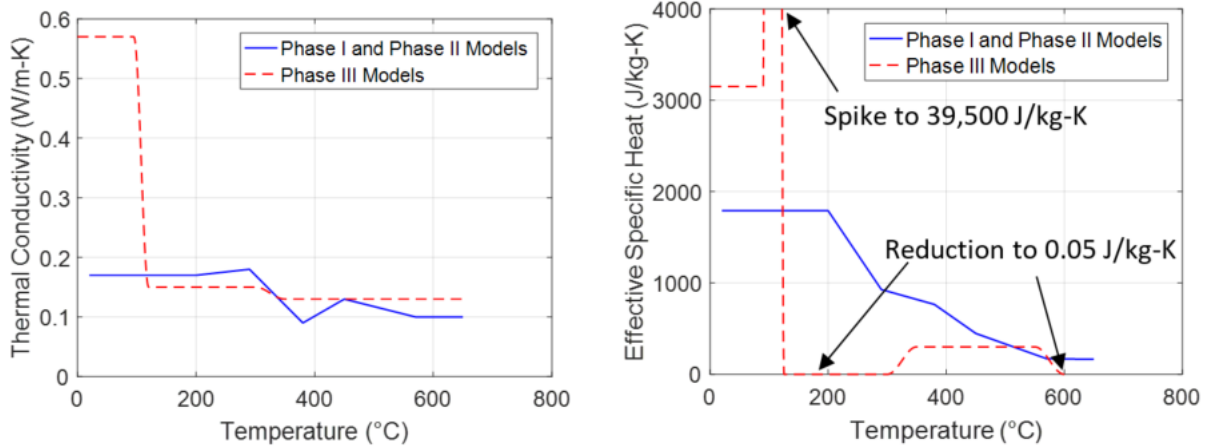
Figure A3. (left) Effective thermal conductivity and (right) effective specific heat capacity of plywood

Notes: The spike in the effective specific heat value near 100 °C represents the heat of evaporation of the moisture within the virgin material. The reduction in the effective specific heat value between 100°C and 350 °C along with the reduction above 600 °C represent exothermic decomposition reactions occurring within the plywood in these temperature ranges.
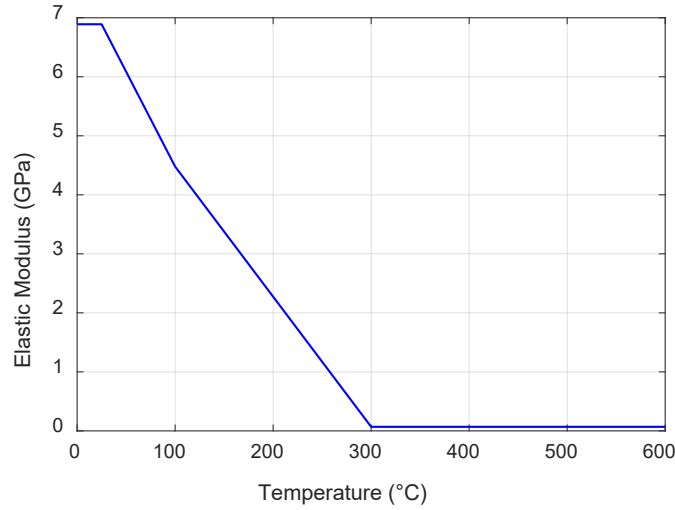
Figure A4. Temperature dependent elastic modulus of plywood

A3. Fiber Reinforced Polymer (FRP)

Table A2. Density of FRP

Model Phase	Density (kg/m³)
Phase I and Phase II	1,400
Phase III	900
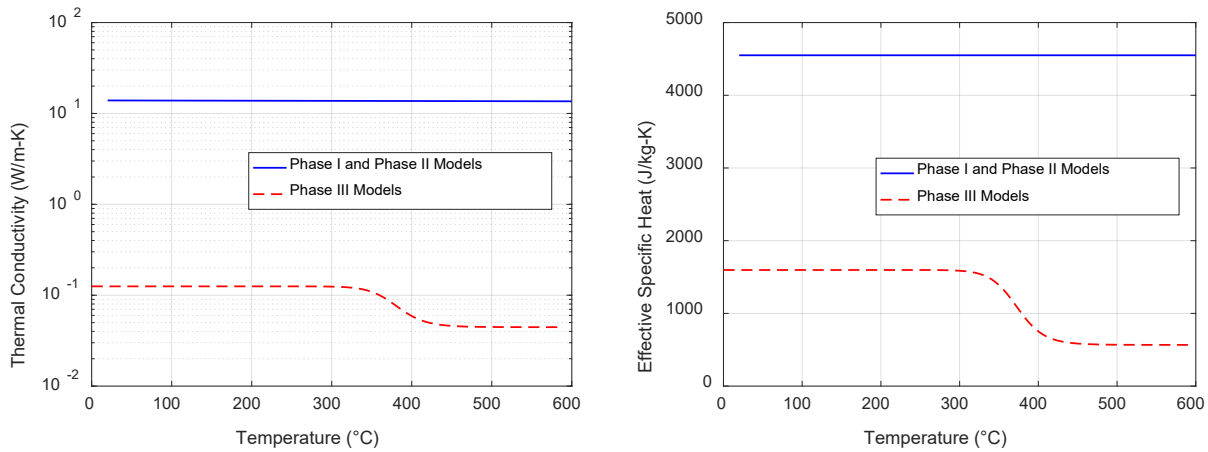
Figure A5. (left) Effective thermal conductivity and (right) effective specific heat capacity of FRP
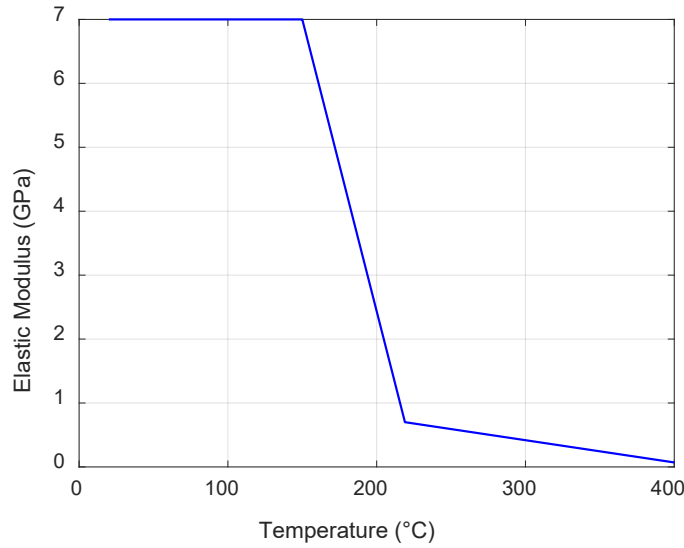
Figure A6. Temperature dependent elastic modulus of FRP

A4. End Grain Balsa

An effective density of balsa used for all models was 36 kg/m^3. Note this is approximated as the char density and effective specific heat values of virgin material were compensated to produce the correct thermal mass.
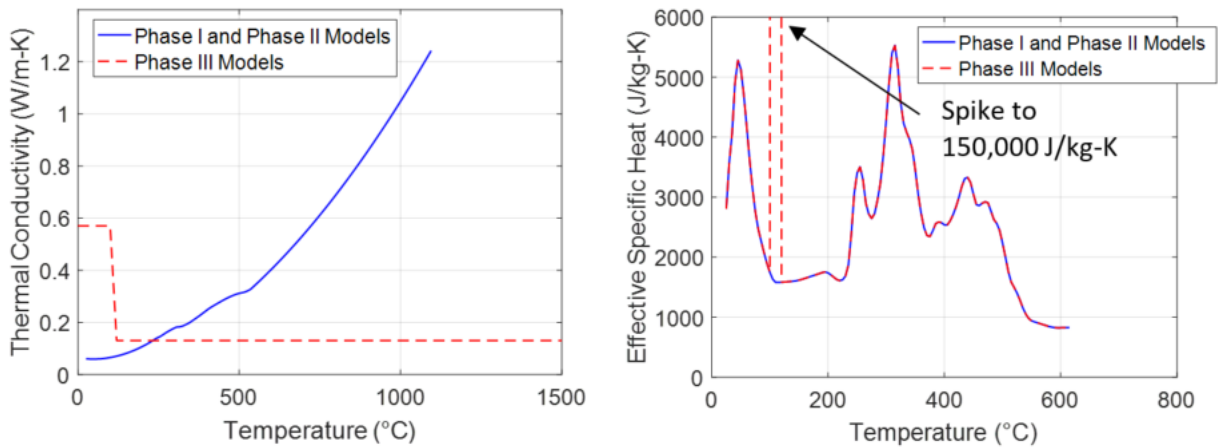
Figure A7. (left) Effective thermal conductivity and (right) effective specific heat capacity of end grain balsa
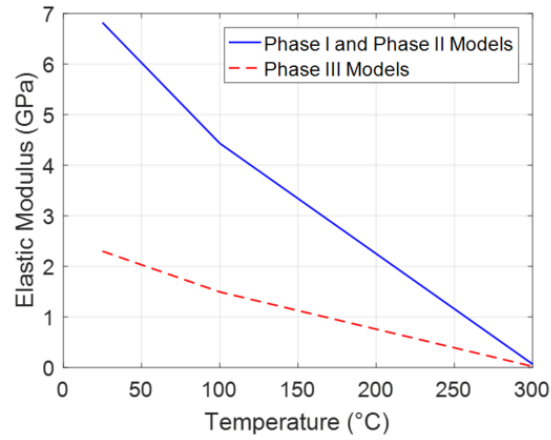
Figure A8. Temperature dependent elastic modulus of end grain balsa

A5. Fiberglass Insulation

The density of fiberglass insulation used for all models was 16 kg/m^3.
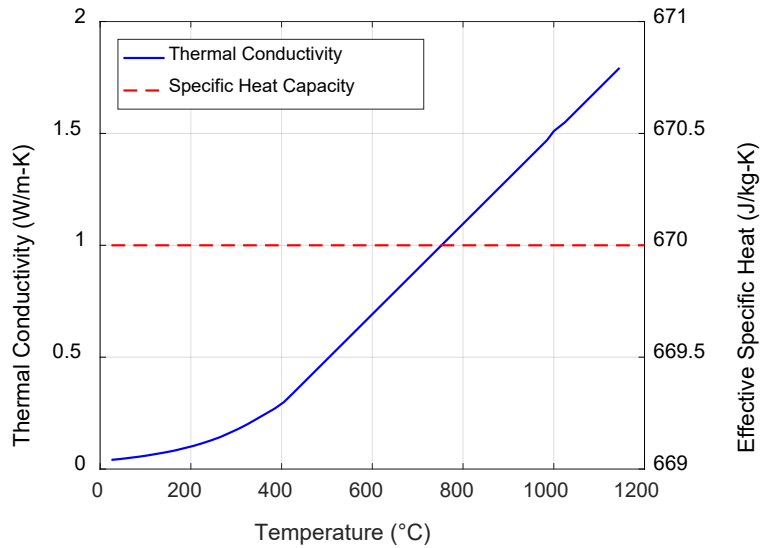
Figure A9. Thermal conductivity and effective specific heat capacity of fiberglass insulation
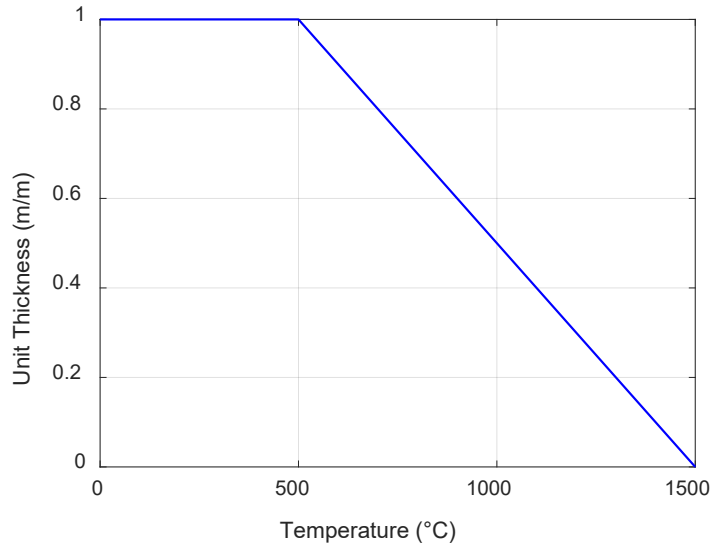
Figure A10. Mechanical degradation behavior of fiberglass insulation

A6.   Ceramic fiberboard Insulation

The density of ceramic fiberboard insulation used for all models was 258 kg/m^3.
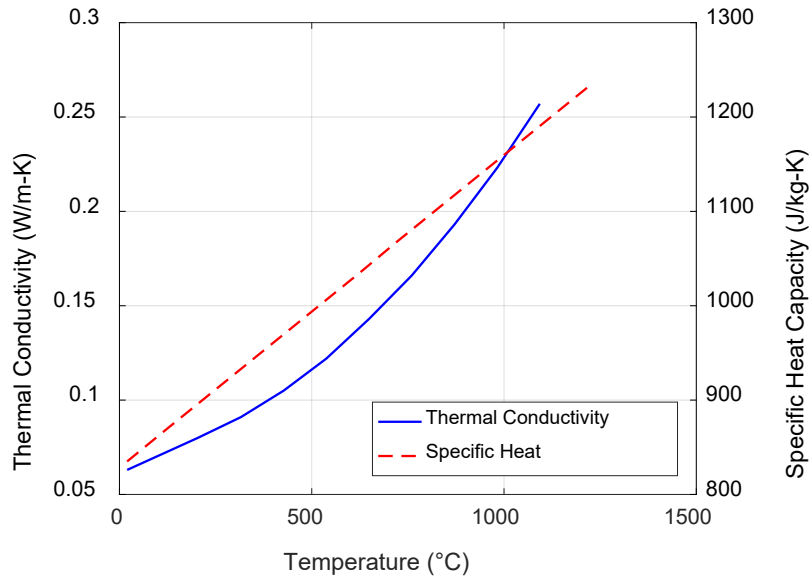
Figure A11. Temperature dependent thermal properties of ceramic fiberboard insulation

Appendix B.
Test Article Drawings

B1. Test Article 1, Full Scale, Transverse Ends Support (NFPA 130)

Figure B1. Test Article 1 assembly drawing sheet 1

1. Lower transverse channels and end channels welded onto Long channels.
2. Steel sheet on lower transverse channels and welded to channels and L-Angle members.
3. Stiffeners welded to steel sheet.
4. Upper transverse channels welded to longitudinal channels, steel sheet, and L-Angle members.
5. Longitudinal members (not shown) welded to steel sheet, transverse members, and stiffeners.
6. Fiberglass insulation (not shown) inserted on steel sheet, under plymetal floor.
7. Plymetal floor screwed to upper transverse members - use self tapping screws similar to #12 self drilling screw, 1-1/2" OAL, flat head, phillips drive, #3 point. Predrill plymetal panels with through-holes. Locate in upper transverse channels every 8 inches.

Location for transverse channels (3x4) welded to L-Angle members shown in Section C-C. Stiffener location is shown in Detail D.

End channel—

—Long channel

A — A

10.00

3.50 ± .05
8.13 ± .05

155.00 ± .25
48.00 ± .05
B

48.00 ± .05
End channel

20.00 ± .05

SECTION A-A
SCALE 0.03 : 1

2.00 —Plymetal panel
Stiffener—

1.25

—Upper transverse channel
4.00

14 gauge steel sheet

—Lower transverse channel

DETAIL B
SCALE 0.1 : 1

DRAWN Stefan Kraft	1/29/2019	JENSEN HUGHES		
CHECKED				
QA				
MFG		TITLE		
APPROVED		Railcar Floor Assembly - Full Scale and Reduced Scale		
All dimensions in inches. Tolerances 0.05" unless otherwise prescribed.		SIZE A	DWG NO FloorAssemblyDetailedDrawings_rev2	REV
		SCALE 0.022 : 1		SHEET 2 OF 9

Figure B2. Test Article 1 assembly drawing sheet 2

44.00 ± .05   Longitudinal member   Stiffener

21.25 ± .05

8.00

33.00 ± .05

B   B

Upper
transverse
member

108.24 ± .12

#12 self-tapping
screws

33.00 ± .05

2.00

SECTION C-C
SCALE 0.04 : 1

C   C

Section A-A shows the frame construction
between the plymetal floor and steel sheet.
Insulation will fill this space, tucked into
the longitudinal and upper transverse channels.

DRAWN Stefan Kraft	1/29/2019	JENSEN HUGHES		
CHECKED				
QA		TITLE		
MFG		Railcar Floor Assembly - Full Scale and Reduced Scale		
APPROVED				
All dimensions in inches. Tolerances 0.05" unless otherwise prescribed.		SIZE A	DWG NO FloorAssemblyDetailedDrawings	REV rev2
		SCALE 0.04 : 1		SHEET 3 OF 9

A   A

Figure B3. Test Article 1 assembly drawing sheet 3

End channel

Plymetal panel 48"x108"

#12 self tapping screws located every 8", predrill plymetal

108.00

Panels centered longitudinally on frame.

All edges of plymetal panels will be sealed with firestop caulk. Total 60 lineal feet. Gaps should be less than 1/4 in.

Caulk applied after thermocouples on plymetal underside installed, ready to test.

48.00

155.00 ± .25

Caulk seams

.75

Long channel

DRAWN Stefan Kraft	1/29/2019	JENSEN HUGHES			
CHECKED					
QA					
MFG		TITLE			
APPROVED		Railcar Floor Assembly - Full Scale and Reduced Scale			
All dimensions in inches. Tolerances 0.05" unless otherwise prescribed.		SIZE A	DWG NO FloorAssemblyDetailedDrawings_rev2		REV
		SCALE 0.04 : 1		SHEET 4 OF 9	

Figure B4. Test Article 1 assembly drawing sheet 4

4.00 ± .05

108.00 ± .05

3.00 +.00 / -.02

0.120" bend radius

Transverse channel, upper, lower, and end

9 total in full scale assembly
3 total in reduced scale assembly

DRAWN Stefan Kraft	1/29/2019	JENSEN HUGHES		
CHECKED				
QA		TITLE		
MFG		Railcar Floor Assembly - Full Scale and Reduced Scale		
APPROVED				
All dimensions in inches. Tolerances 0.05" unless otherwise prescribed.		SIZE A	DWG NO FloorAssemblyDetailedDrawings_rev2	REV
		SCALE 0.05 : 1	SHEET 5 OF 9	

Figure B5. Test Article 1 assembly drawing sheet 5

Cut for transverse stiffener
No contact,
weld to stiffener

.50 +.08 / -.00

1.50 +.10 / -.00

DETAIL D

47.88 ± .05

D

3.90 ± .05

21.25 ± .05

2.50 ± .05

Cut for fitting
into upper
transverse
channel

2.88 +.00 / -.02

0.120" bend radius

As drawn, for one side of frame assembly
For other side bend in opposite direction

DRAWN Stefan Kraft	1/29/2019	JENSEN HUGHES	
CHECKED			
QA		TITLE	
MFG		Railcar Floor Assembly - Full Scale and Reduced Scale	
APPROVED			

All dimensions in inches.
Tolerances 0.05" unless
otherwise prescribed.

SIZE A	DWG NO FloorAssemblyDetailedDrawings	REV rev2
SCALE 0.5 : 1		SHEET 6 OF 9

Figure B6. Test Article 1 assembly drawing sheet 6

Figure B7. Test Article 1 assembly drawing sheet 7

B2. Test Article 2, Full Scale, Longitudinal Ends Support

Figure B8. Test Article 2 assembly drawing sheet 1

1. Lower transverse channels and end channels welded onto Long channels.
2. Steel sheet on lower transverse channels and welded to channels and L-Angle members.
3. Stiffeners welded to steel sheet.
4. Upper transverse channels welded to longitudinal channels, steel sheet, and L-Angle members.
5. Longitudinal members (not shown) welded to steel sheet, transverse members, and stiffeners.
6. Fiberglass insulation (not shown) inserted on steel sheet, under plymetal floor.
7. Plymetal floor screwed to upper transverse members - use self tapping screws similar to #12 self drilling screw, 1-1/2" OAL, flat head, phillips drive, #3 point. Predrill plymetal panels with through-holes. Locate in upper transverse channels every 8 inches.

148.00
24.00   24.00   24.00
24.00
24.00   24.00

SECTION G-G
SCALE 0.03 : 1

108.24

2.00
Upper Transverse Channel
Plymetal
Stiffener
Bottom Steel Sheet
1.25
Lower Transverse Channel

DETAIL H
SCALE 0.08 : 1

DRAWN Stefan Kraft	2/27/2019		JENSEN HUGHES	
CHECKED				
QA		TITLE		
MFG				
APPROVED		Railcar Floor Assembly - Full Scale Longitudinal BC		

All dimensions in inches. Tolerances 0.05" unless otherwise prescribed.	SIZE A	DWG NO FloorAssemblyDetailedDrawings_longitudin	REV
	SCALE 0.03 : 1		SHEET 2 OF 7

Figure B9. Test Article 2 assembly drawing sheet 2

SECTION J-J
SCALE 0.040 : 1

Long Channel/Main Support

Stiffener

Steel Sheet

Longitudinal Channel

Upper Transverse Channel
(Lower not shown, below
steel sheet under stiffener)

#12 screw for plymetal

12.0

1.50

8.0

33

21.25

37 108 ± .25

33

48.00

48.00

J

J

Section J-J shows the frame construction
between the plymetal floor and steel sheet.
Insulation will fill this space, tucked into
the longitudinal and upper transverse channels.

DRAWN Stefan Kraft	2/27/2019	JENSEN HUGHES
CHECKED		
QA		TITLE
MFG		Railcar Floor Assembly - Full Scale Longitudinal BC
APPROVED		

All dimensions in inches.
Tolerances 0.05" unless
otherwise prescribed.

SIZE A	DWG NO FloorAssemblyDetailedDrawings_longitudin	REV
SCALE 0.040 : 1		SHEET 3 OF 7

Figure B10. Test Article 2 assembly drawing sheet 3

Predrill plymetal
locations, if needed.
Screw into upper
transverse channel and
main longitudinal
channel with self
tapping screws.

108.00

48.00

Caulk Seam

8.00

12.00

Panels centered
longitudinally on
frame.

All edges of plymetal
panels will be sealed
with firestop caulk.
Total 60 lineal feet.
Gaps should be less
than 1/4 in.

Caulk applied after
thermocouples on
plymetal underside
installed, ready to test.

Plymetal panel

DRAWN Stefan Kraft	2/27/2019	JENSEN HUGHES		
CHECKED				
QA		TITLE		
MFG		Railcar Floor Assembly - Full Scale Longitudinal BC		
APPROVED				
All dimensions in inches. Tolerances 0.05" unless otherwise prescribed.		SIZE A	DWG NO FloorAssemblyDetailedDrawings_longitudin	REV
		SCALE 0.05 : 1		SHEET 4 OF 7

Figure B11. Test Article 2 assembly drawing sheet 4

2

1

B

4.00 ± .05

B

108.00 ± .05

3.00 $^{+.00}_{-.02}$

0.120" bend radius

Transverse channel, upper and lower

7 total in assembly

DRAWN Stefan Kraft	2/27/2019	JENSEN HUGHES		
CHECKED				
QA		TITLE		
MFG				
APPROVED		Railcar Floor Assembly - Full Scale Longitudinal BC		

A

A

All dimensions in inches.
Tolerances 0.05" unless
otherwise prescribed.

SIZE A	DWG NO FloorAssemblyDetailedDrawings_longitudin	REV
SCALE 0.05 : 1	SHEET 5 OF 7	

2

1

Figure B12. Test Article 2 assembly drawing sheet 5

Cut for transverse stiffener
No contact,
weld to stiffener

$.50 ^{+.08}_{-.00}$

$1.50 ^{+.10}_{-.00}$

DETAIL D

47.88 ± .05

D

3.90 ± .05

21.25 ± .05

2.50 ± .05

Cut for fitting
into upper
transverse
channel

$2.88 ^{+.00}_{-.02}$

0.120" bend radius

As drawn, for one side of frame assembly
For other side bend in opposite direction

DRAWN		JENSEN HUGHES	
Stefan Kraft	2/27/2019		
CHECKED			
QA		TITLE	
MFG		Railcar Floor Assembly - Full Scale Longitudinal BC	
APPROVED			
All dimensions in inches. Tolerances 0.05" unless otherwise prescribed.		SIZE A	DWG NO FloorAssemblyDetailedDrawings_longitudin	REV
		SCALE 0.5 : 1	SHEET 6 OF 7

Figure B13. Test Article 2 assembly drawing sheet 6

107

1.50 ± .05

0.120"
bend
radius

.50 ± .05

108.00 ± .05

Transverse Stiffener - Welded to
steel sheet on top of lower transverse
channel

B

L Angle - Main Longitudinal Support
148.00" length

Cutouts to fit 4" transverse channels

Bottom leg main channel

Cutout in top leg

Top leg main channel

1.50 ± .10

9.25 ± .05

4.00

44.00   44.00   44.00

4.00 →| |← 4.00 →| |← 4.00 →| 4.00 →|

0.120" bend radius

2.75 ± .10

DRAWN Stefan Kraft	2/27/2019	JENSEN HUGHES	
CHECKED			
QA		TITLE	
MFG		Railcar Floor Assembly - Full Scale Longitudinal BC	
APPROVED			

All dimensions in inches.
Tolerances 0.05" unless
otherwise prescribed.

SIZE A	DWG NO FloorAssemblyDetailedDrawings_longitudin	REV
SCALE 0.04 : 1	SHEET 7 OF 7	

Figure B14. Test Article 2 assembly drawing sheet 7

Figure B15. Test Article 3a assembly drawing sheet 1

Top view - Plymetal panels cut from 48x108 sheet bolted to upper transverse channels with #12 self-tapping screws every 7.5"

Use firestop caulk on seams

Caulk seams

1.5

1.5

52.00

7.5

34.25   39.50   34.25

Stiffener

Upper transverse channel

Longitudinal channel

Steel sheet (11 gauge)

21.25 ± .05

33.00

108.24 ± .05

33.00

SECTION F-F

Insert fiberglass insulation between steel sheet and plymetal covering.

F   F

Long channel

Steel sheet (underside)

Bottom transverse channel

Bottom view

52.00

24.00 ± .05

DRAWN Stefan Kraft	1/29/2019
CHECKED	
QA	
MFG	
APPROVED	

JENSEN HUGHES

TITLE

Railcar Floor Assembly - Full Scale and Reduced Scale

All dimensions in inches.
Tolerances 0.05" unless otherwise prescribed.

| SIZE A | DWG NO FloorAssemblyDetailedDrawings_rev2 | REV |
| SCALE 0.03 : 1 | SHEET 9 OF 9 | |

Figure B16. Test Article 3a assembly drawing sheet 2

2   1

B   B

4.00 ± .05

108.00 ± .05

3.00 +.00 / -.02

0.120" bend radius

Transverse channel, upper, lower, and end

9 total in full scale assembly
3 total in reduced scale assembly

DRAWN Stefan Kraft	1/29/2019	JENSEN HUGHES		
CHECKED				
QA		TITLE		
MFG		Railcar Floor Assembly - Full Scale and Reduced Scale		
APPROVED				
All dimensions in inches. Tolerances 0.05" unless otherwise prescribed.		SIZE A	DWG NO FloorAssemblyDetailedDrawings_rev2	REV
		SCALE 0.05 : 1		SHEET 5 OF 9

A   A

2   1

Figure B17. Test Article 3a assembly drawing sheet 3

Cut for transverse stiffener
No contact,
weld to stiffener

.50 +.08 / -.00

1.50 +.10 / -.00

DETAIL D

47.88 ± .05

D

3.90 ± .05

21.25 ± .05

2.50 ± .05

Cut for fitting
into upper
transverse
channel

2.88 +.00 / -.02

0.120" bend radius

As drawn, for one side of frame assembly
For other side bend in opposite direction

DRAWN Stefan Kraft	1/29/2019	JENSEN HUGHES		
CHECKED				
QA		TITLE		
MFG		Railcar Floor Assembly - Full Scale and Reduced Scale		
APPROVED				

All dimensions in inches.
Tolerances 0.05" unless
otherwise prescribed.

SIZE A	DWG NO FloorAssemblyDetailedDrawings_rev2	REV
SCALE 0.5 : 1	SHEET 6 OF 9	

2

1

Figure B18. Test Article 3a assembly drawing sheet 4

1.50 ± .05

0.120" bend radius

.50 ± .05

108.00 ± .05

Transverse Stiffener - Welded to steel sheet on top of lower transverse channel

L Angle - Main Longitudinal Support
180.00" length for full scale frame
52.00" for reduced scale frame

Cutouts to fit 4" transverse channels

52.00

4.00   4.00

1.50 ± .10

9.25 ± .05

180.00 ± .25

16.00   48.00   48.00   48.00

4.00   4.00   4.00   4.00

0.120" bend radius

2.75 ± .10

DRAWN Stefan Kraft	1/29/2019	JENSEN HUGHES		
CHECKED				
QA		TITLE		
MFG		Railcar Floor Assembly - Full Scale and Reduced Scale		
APPROVED				

All dimensions in inches. Tolerances 0.05" unless otherwise prescribed.	SIZE A	DWG NO FloorAssemblyDetailedDrawings	REV rev2
	SCALE 0.04 : 1		SHEET 7 OF 9

Figure B19. Test Article 3a assembly drawing sheet 5

B4. Test Article 3b, Alternative Design, Longitudinal Ends Support

Figure B20. Test Article 3b assembly drawing sheet 1

Parts List:

	Steel Thickness (gauge)	Count
Center Sill Channel	0.25"	2
Center Sill Bottom Plate	0.25"	1
Z-Channel	0.060" (16 gauge)	4
Z-Channel Gusset	0.060" (16 gauge)	8
Side Sill Channel	0.25"	2
Side Sill Cap	0.060" (16 gauge)	4
Hat Channel	0.060" (16 gauge)	2
Bottom Sheet	0.060" (16 gauge)	1
Fiberfrax*	0.25"	4
Composite Panel	0.75"	1

*Installed at test lab

Assembly Steps:

1. Center Sill Channels to Bottom Plate (weld)
2. Steel sheet to Center Sill Channels (tack weld for placement)
3. Z Channels to Center Sill Channels and steel sheet (weld)
4. Hat Channels to Z Channels (weld)
5. Z Channel Gussets to Z Channels (weld)
6. Side Sill Channels to Z Channel Gussets (weld)
7. Insert Fiberglass Insulation on top of steel sheet
8. Insert Fiberfrax between Hat Channels and Z Channels
9. Place 3/8 in thick Fiberfrax on panel screw surface where metal will contact composite panel
10. Composite panel to Z Channels (screws)

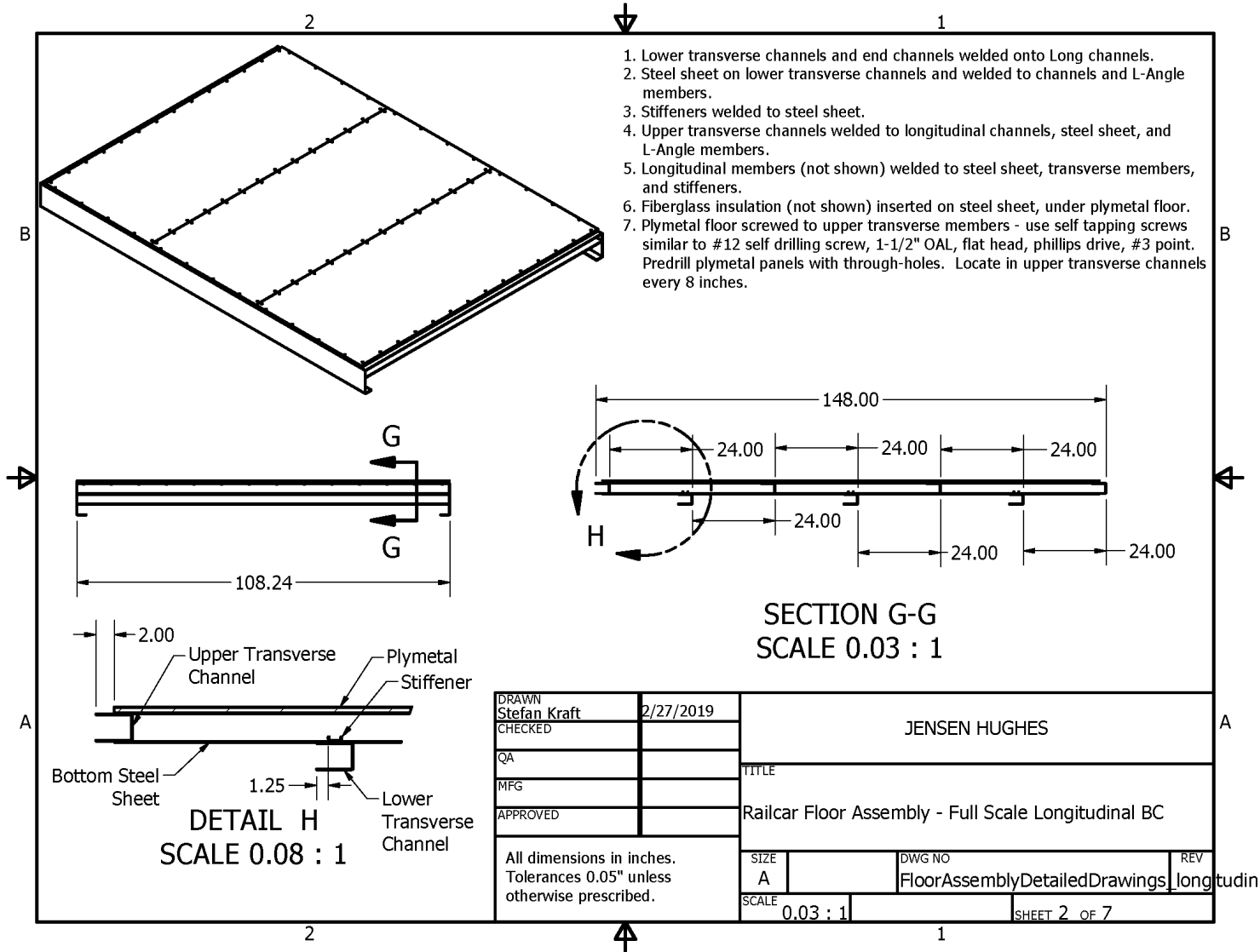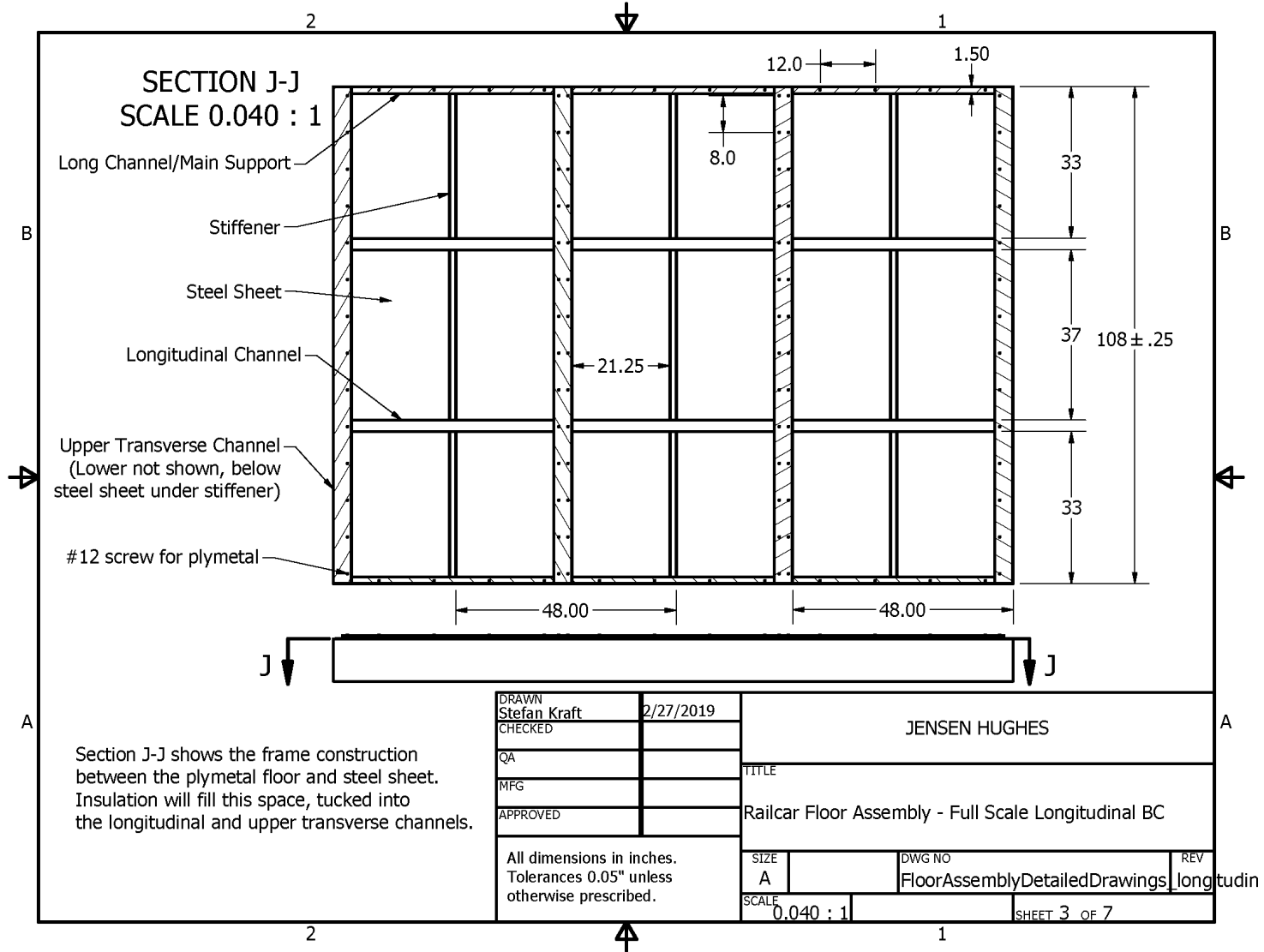| DRAWN Stefan Kraft	2/28/2019	JENSEN HUGHES		
CHECKED				
QA		TITLE		
MFG		Reduced Scale Assembly Design 2		
APPROVED				
		SIZE A	DWG NO AssemblyDesign2-1	REV
		SCALE 1 /15		SHEET 2 OF 11

Figure B21. Test Article 3b assembly drawing sheet 2

115
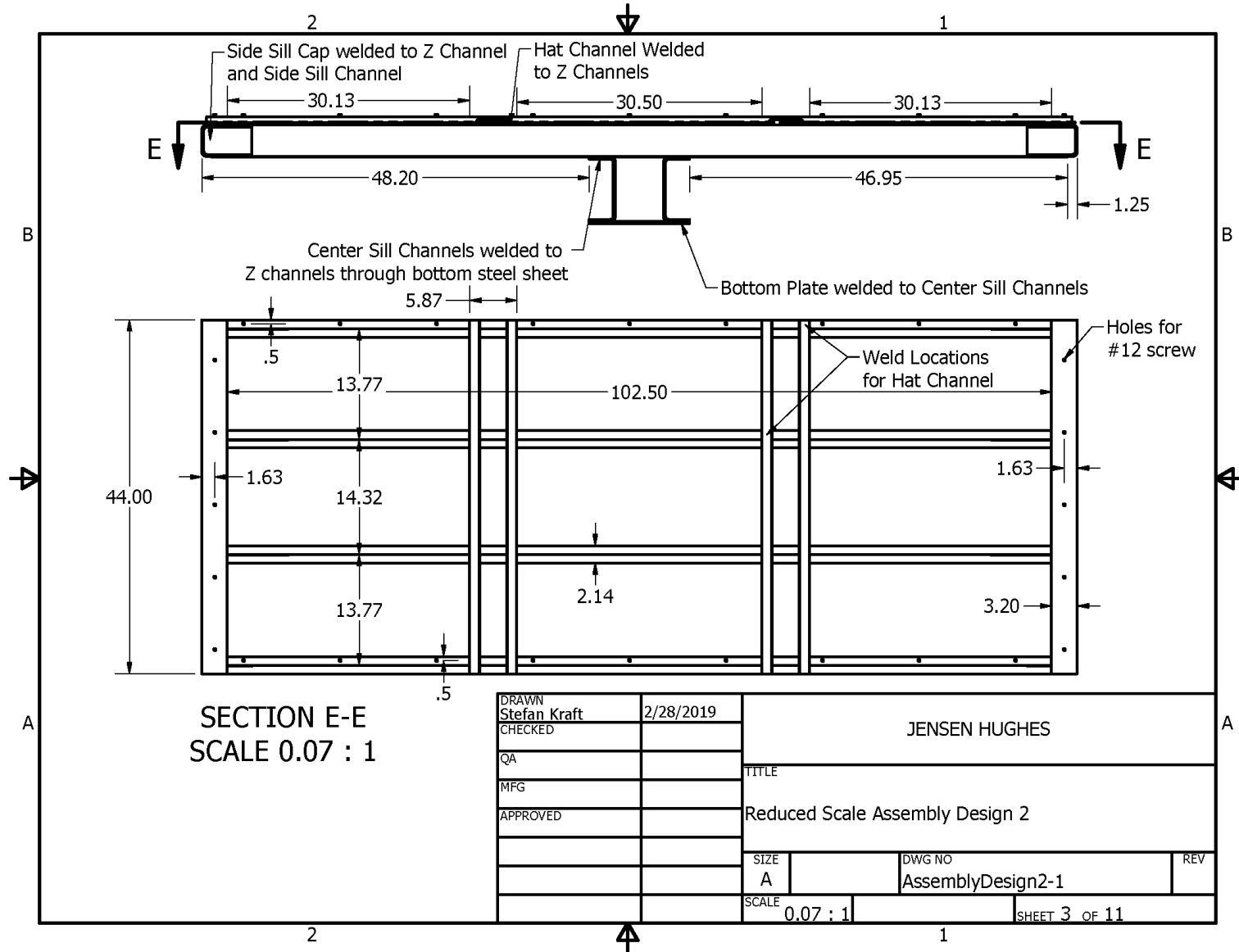
Figure B22. Test Article 3b assembly drawing sheet 3
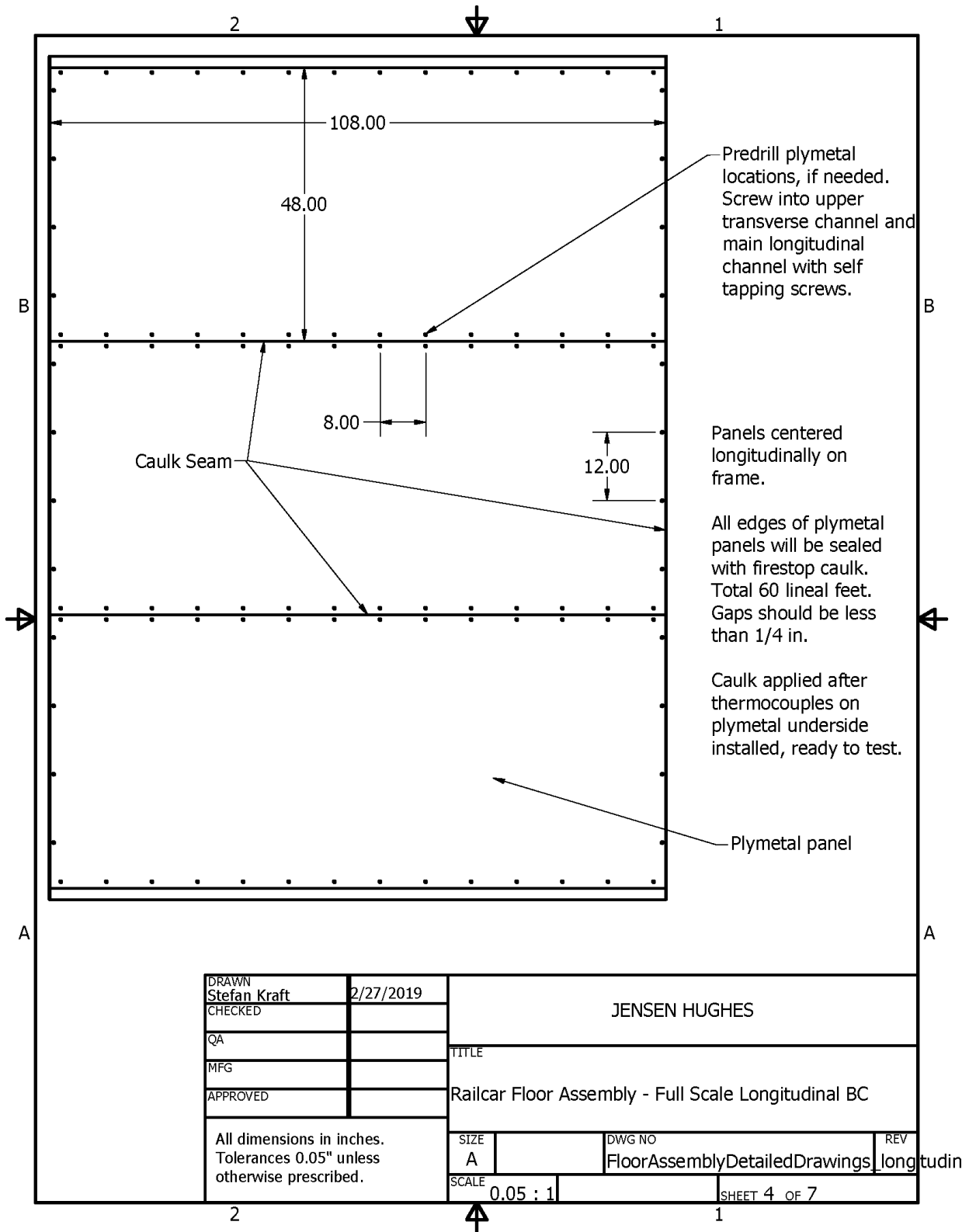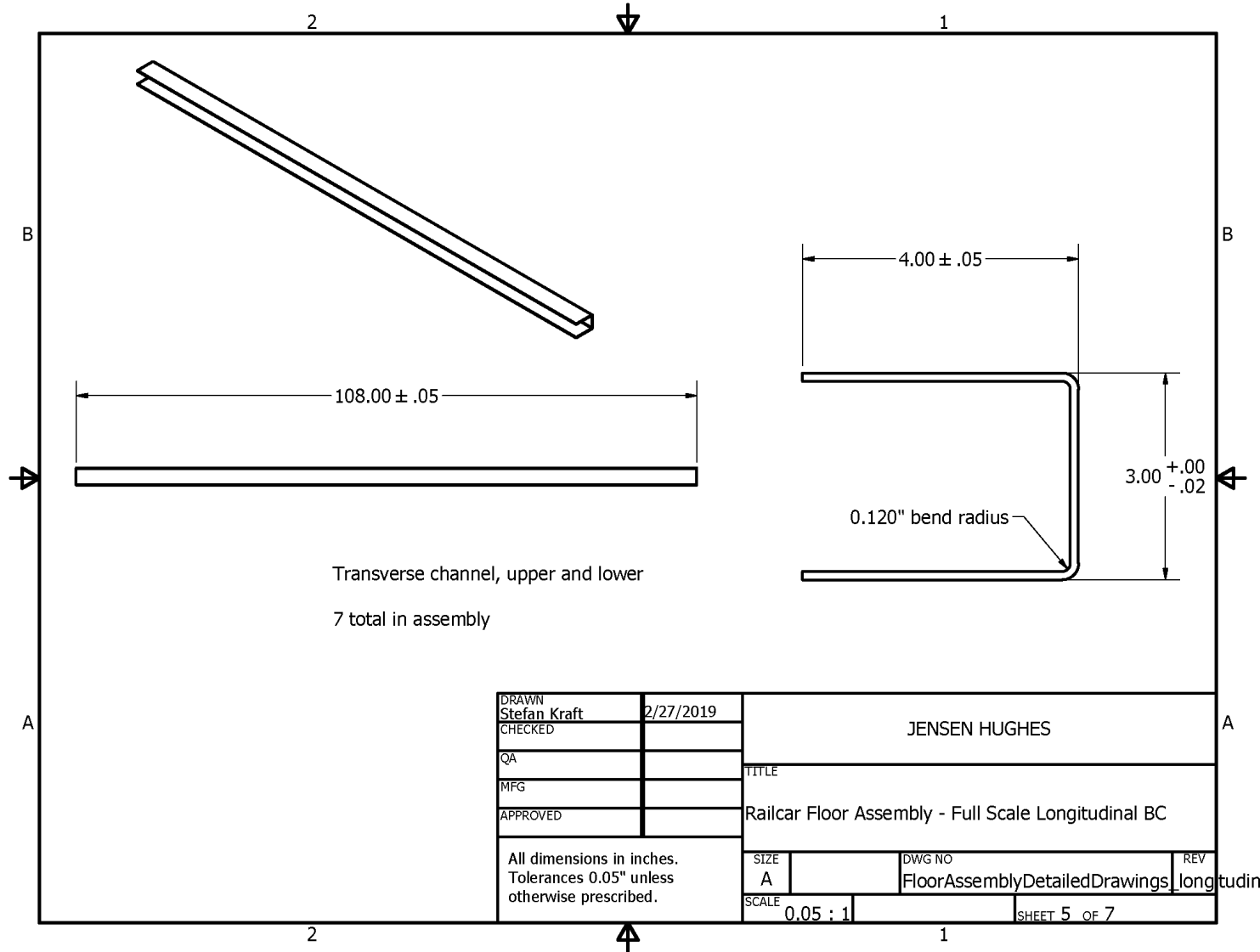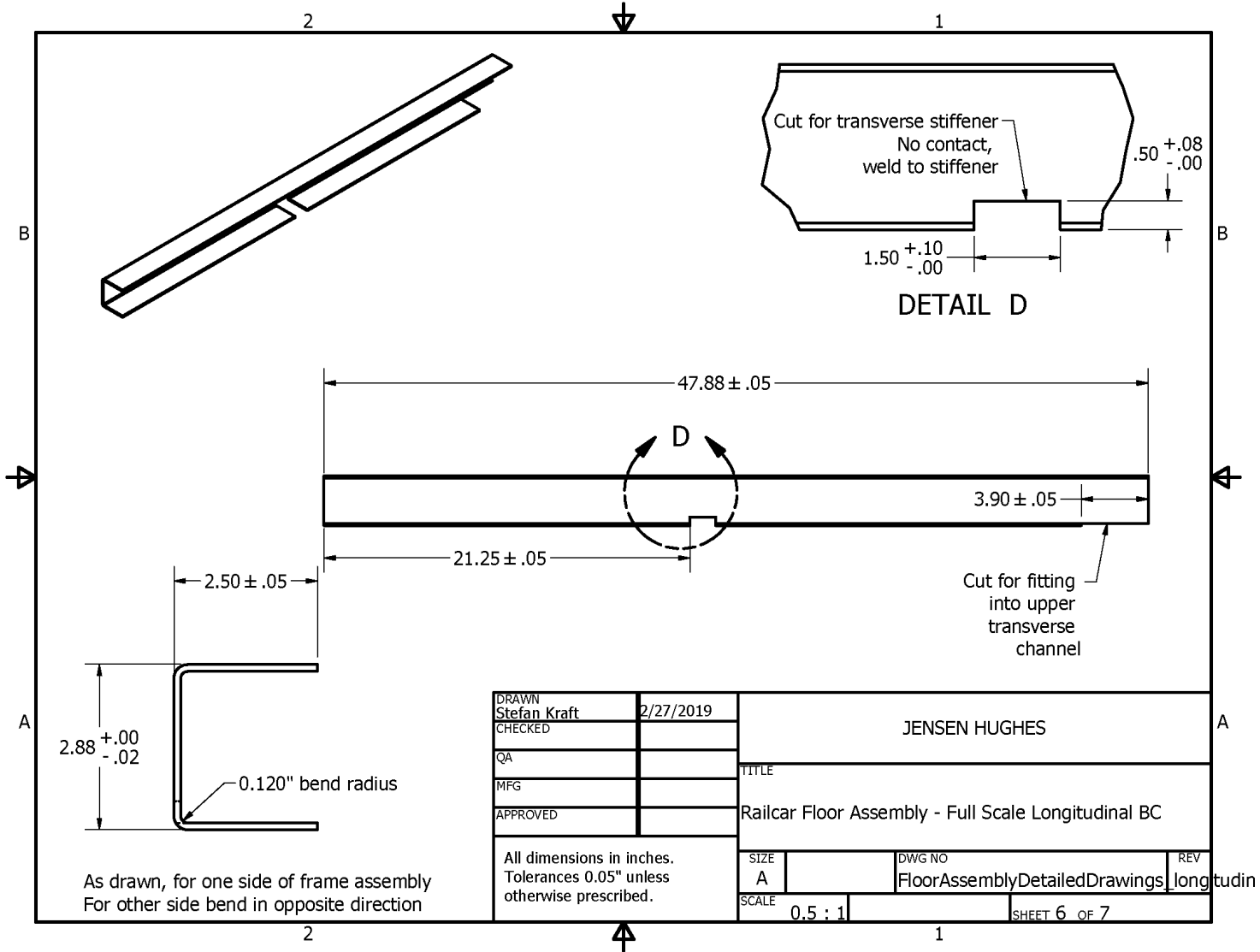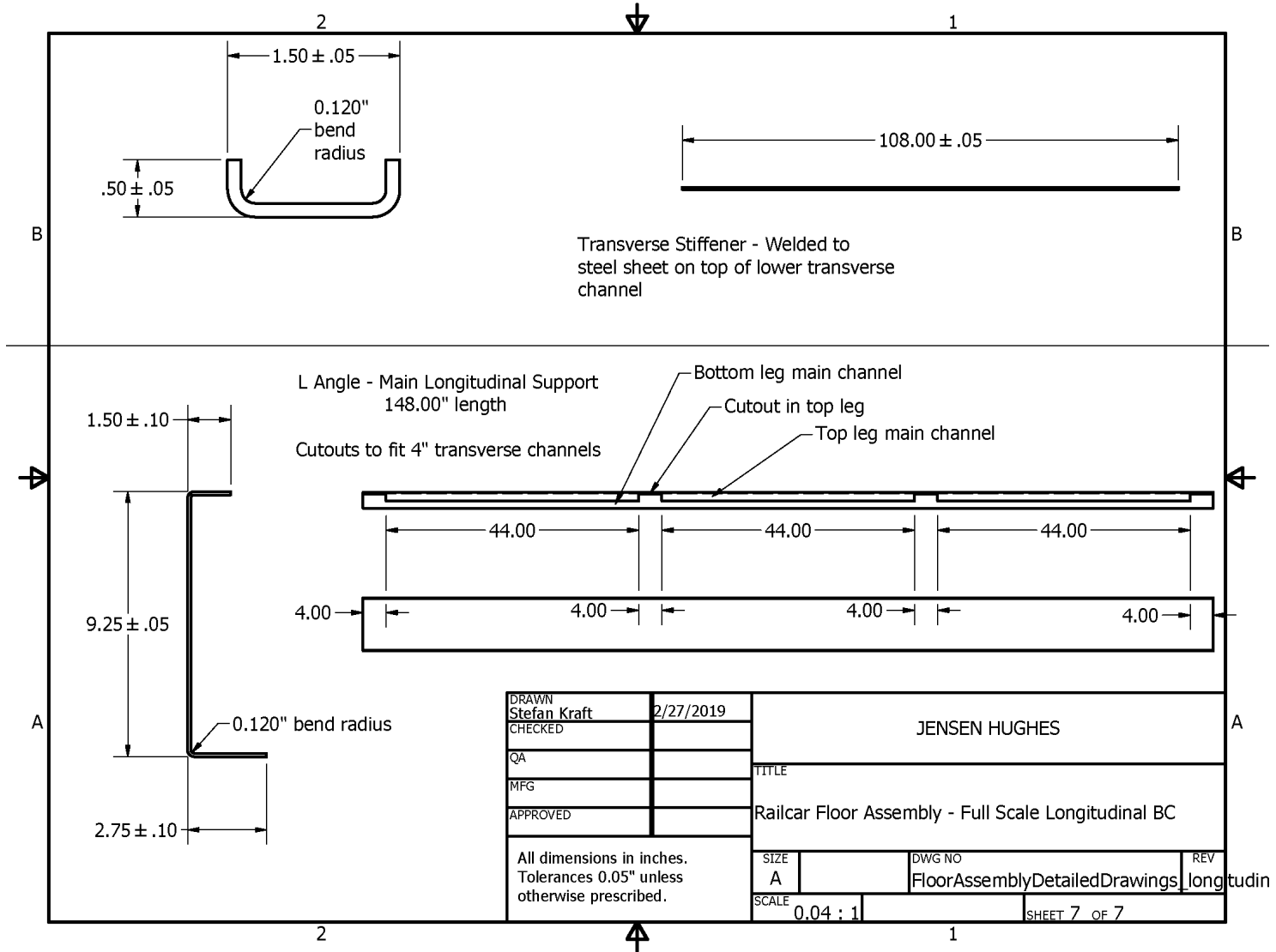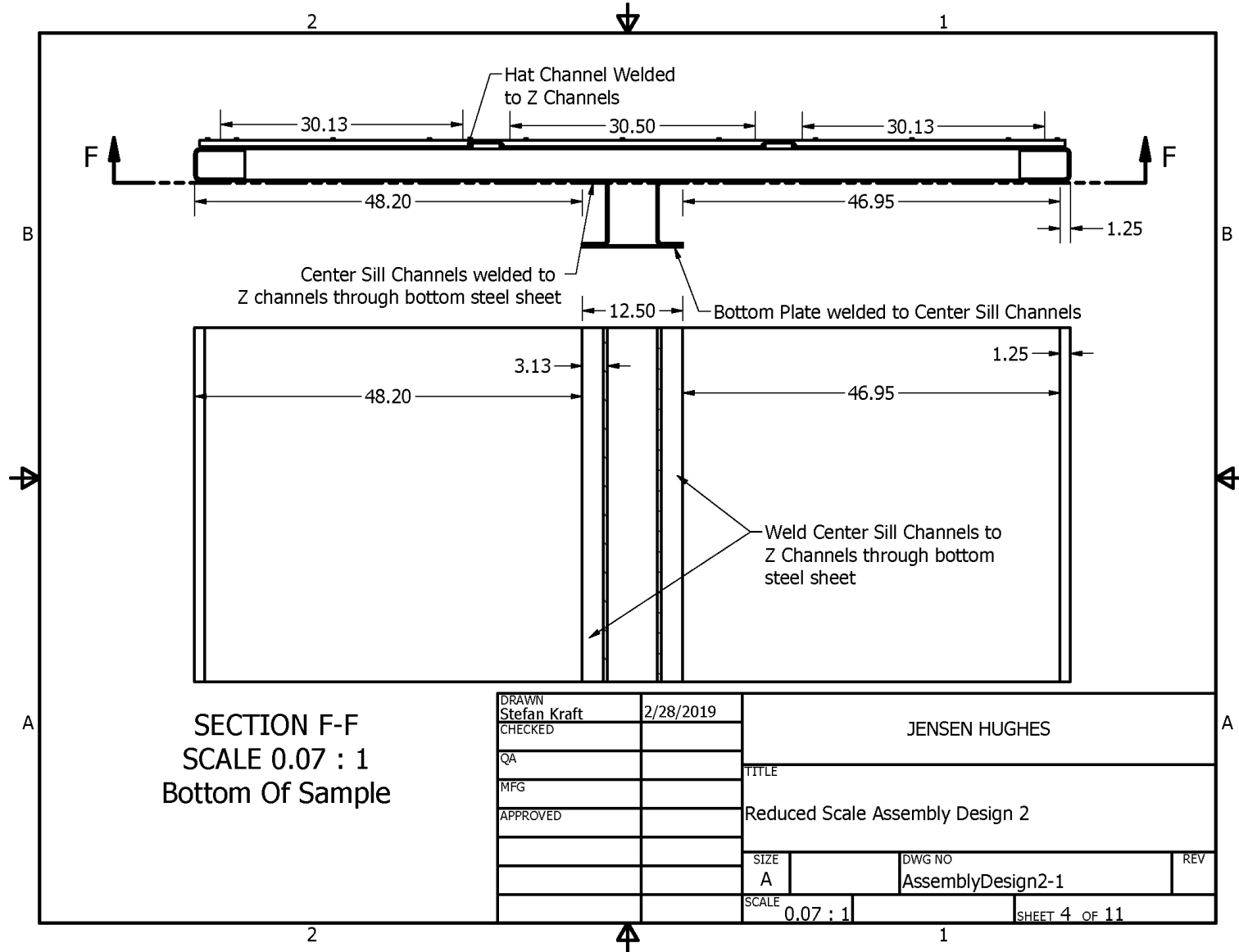
Figure B23. Test Article 3b assembly drawing sheet 4

Fiberfrax to fill gap
between composite
panel and steel (3/8")

.28

DETAIL L
SCALE 0.14 : 1

2

30.13

30.50

30.13

L

J J

48.20

1.25

Insert Fiberfrax
in between Hat Channel
and Z Channel cavity

Center Sill Channels welded to
Z channels through bottom steel sheet

Bottom Plate welded to Center Sill Channels

Z Channel Gusset welded to
Z Channel and Side Sill Channel

Side Sill Channel
inside edge

Side Sill Cap

Side Sill Channel

Z Channel

Z Channel Gusset

Side Sill Cap welded to Z Channel
and Side Sill to seal assembly

DETAIL K
SCALE 0.3: 1

K

SECTION J-J
SCALE 0.07 : 1

DRAWN Stefan Kraft	2/28/2019	JENSEN HUGHES	
CHECKED			
QA		TITLE	
MFG			
APPROVED		Reduced Scale Assembly Design 2	
		SIZE A	DWG NO AssemblyDesign2-1	REV
		SCALE 0.07 : 1	SHEET 5 OF 11

B   B

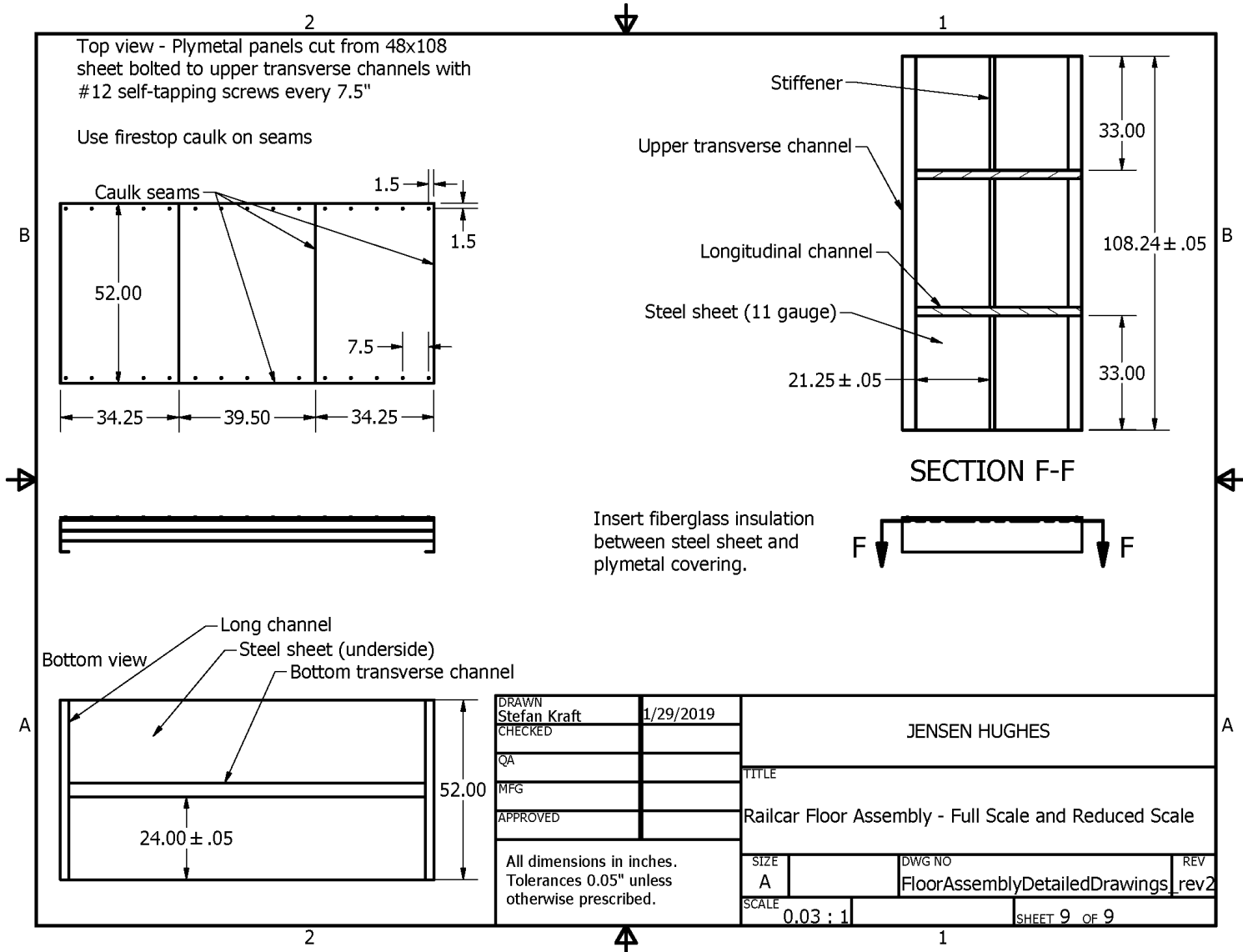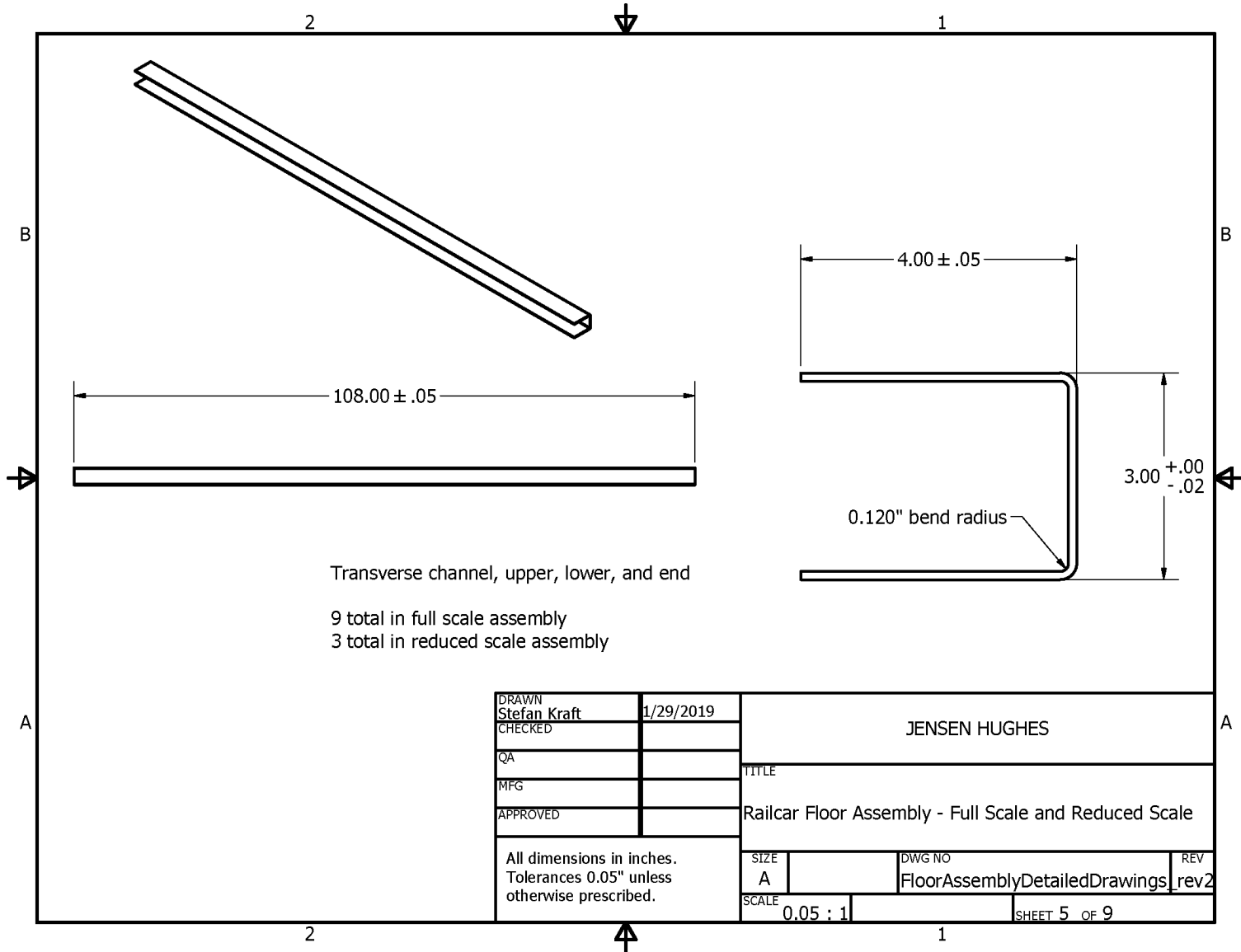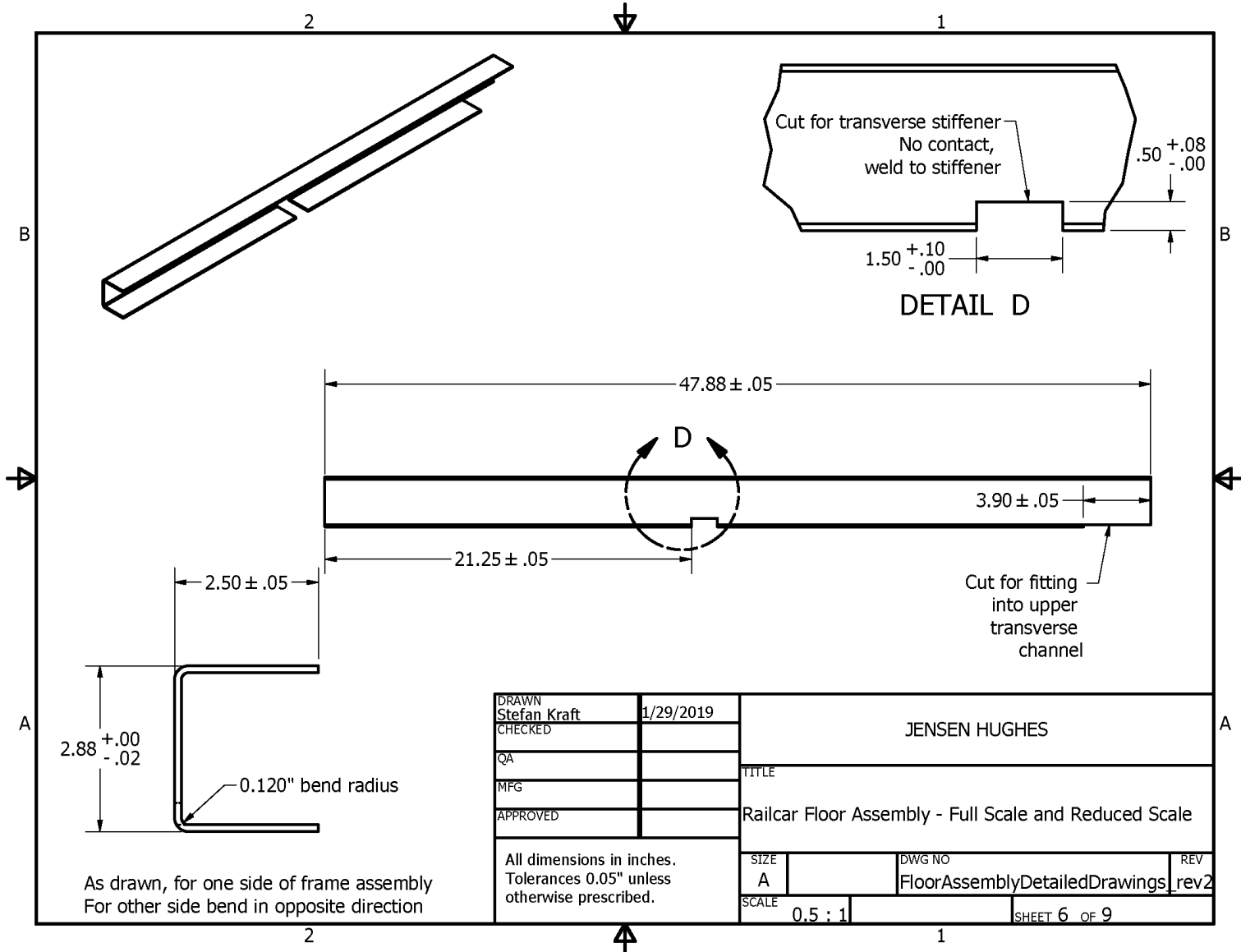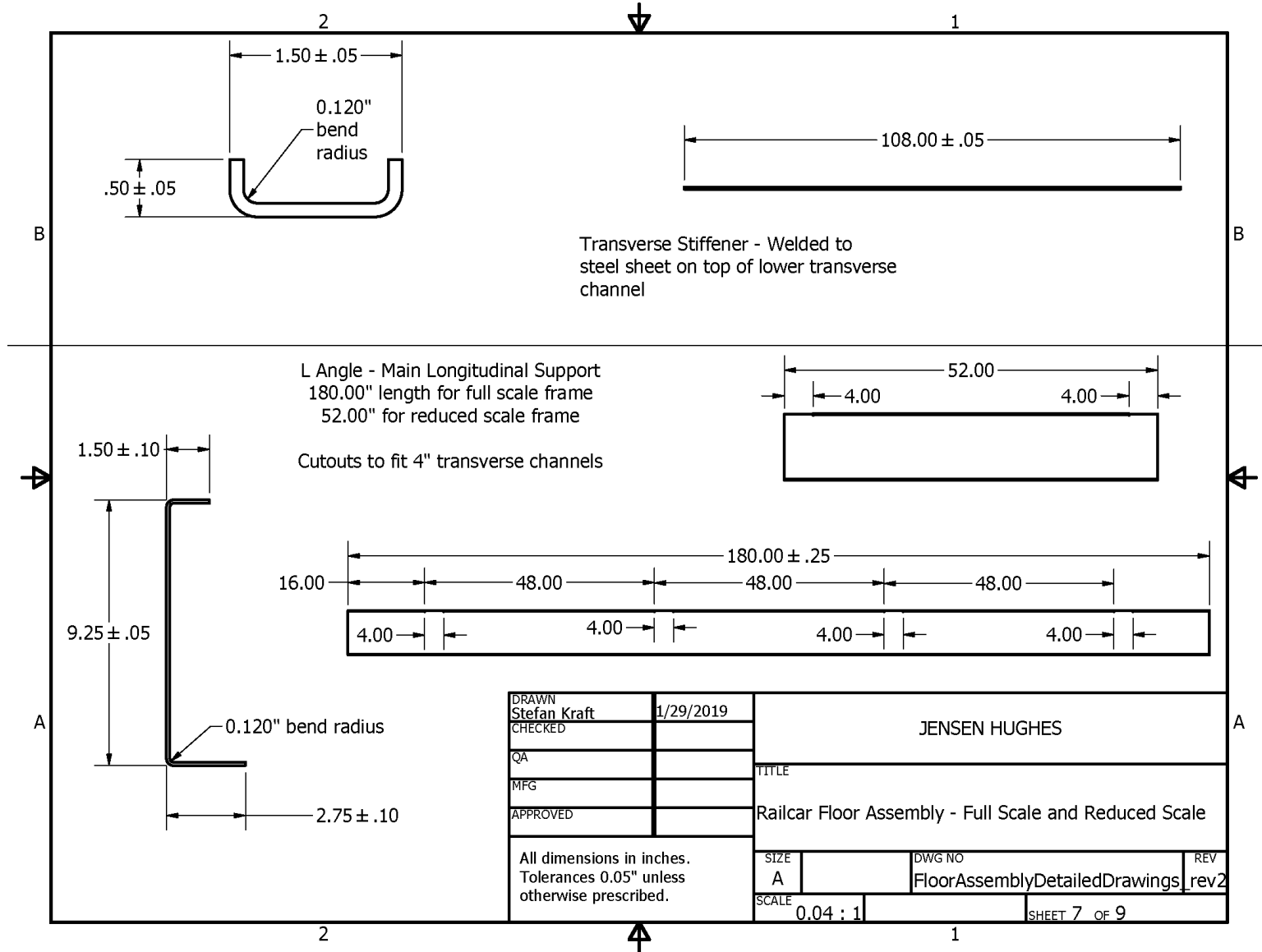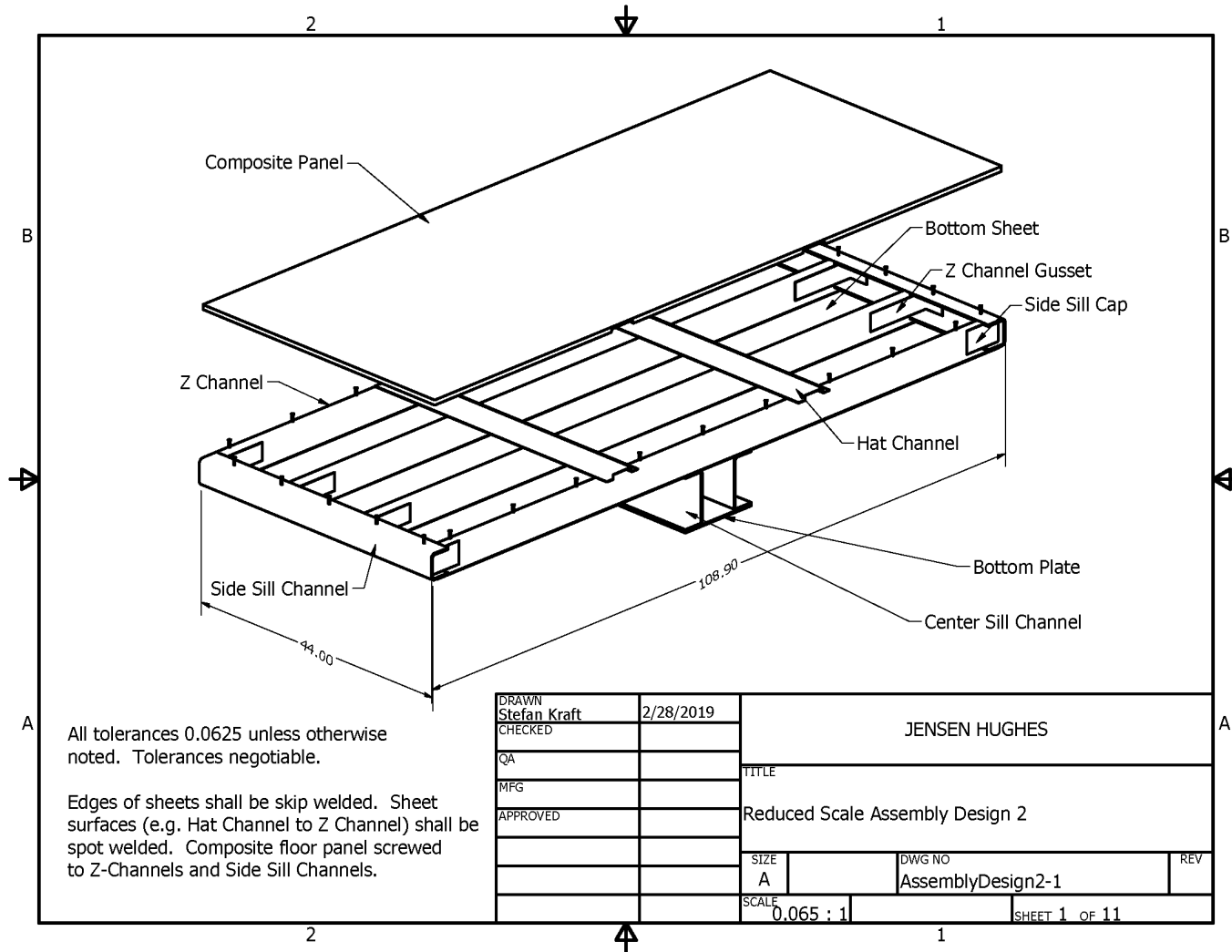A   A

2   1
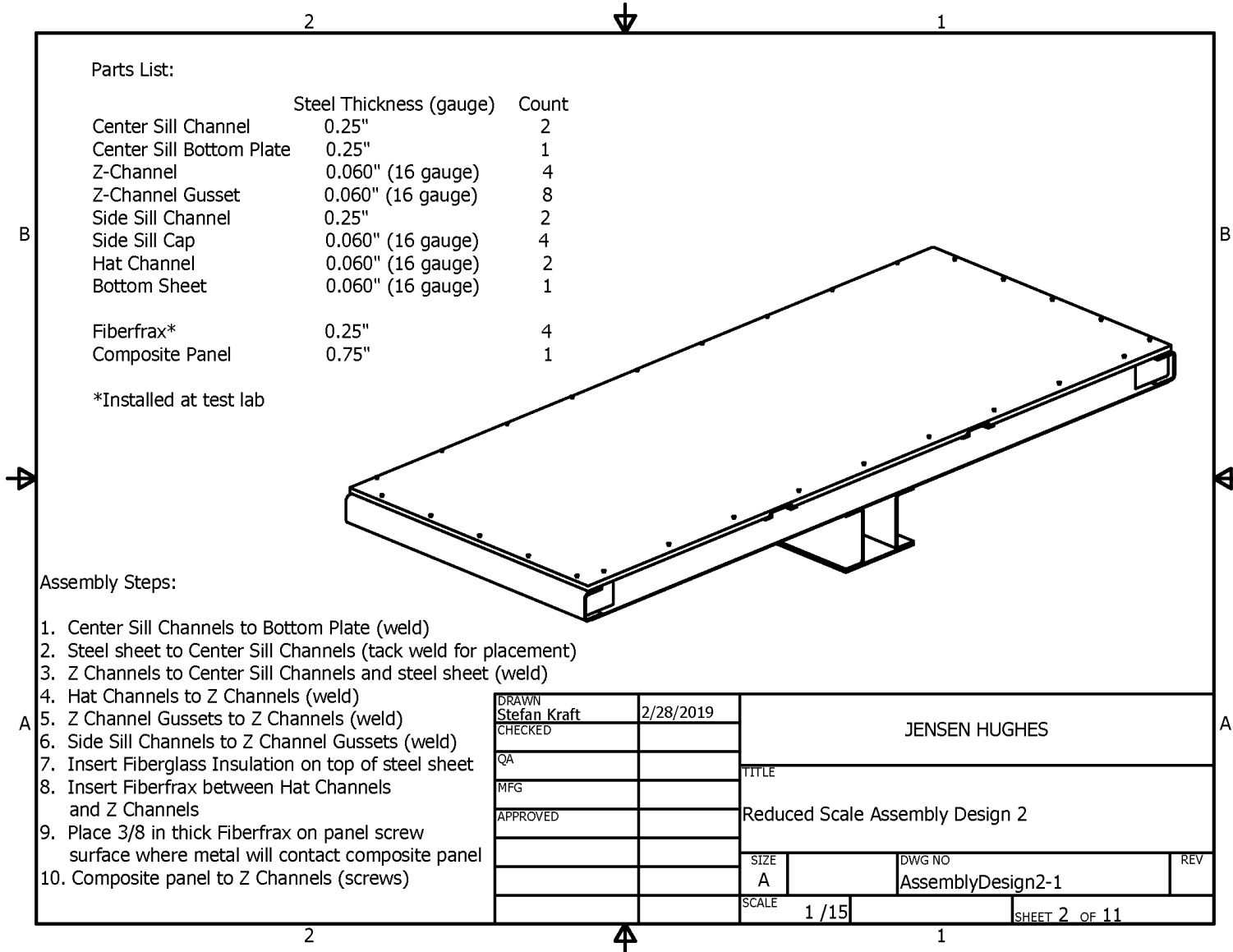
Figure B24. Test Article 3b assembly drawing sheet 5

118

Side Sill Channel

3.94

B

.25

3.20

R.63

44.00

VIEW B-B
SCALE 0.2 : 1

DRAWN Stefan Kraft	2/28/2019	JENSEN HUGHES		
CHECKED				
QA		TITLE		
MFG				
APPROVED		Reduced Scale Assembly Design 2		
		SIZE A	DWG NO AssemblyDesign2-1	REV
		SCALE 0.2 : 1		SHEET 6 OF 11
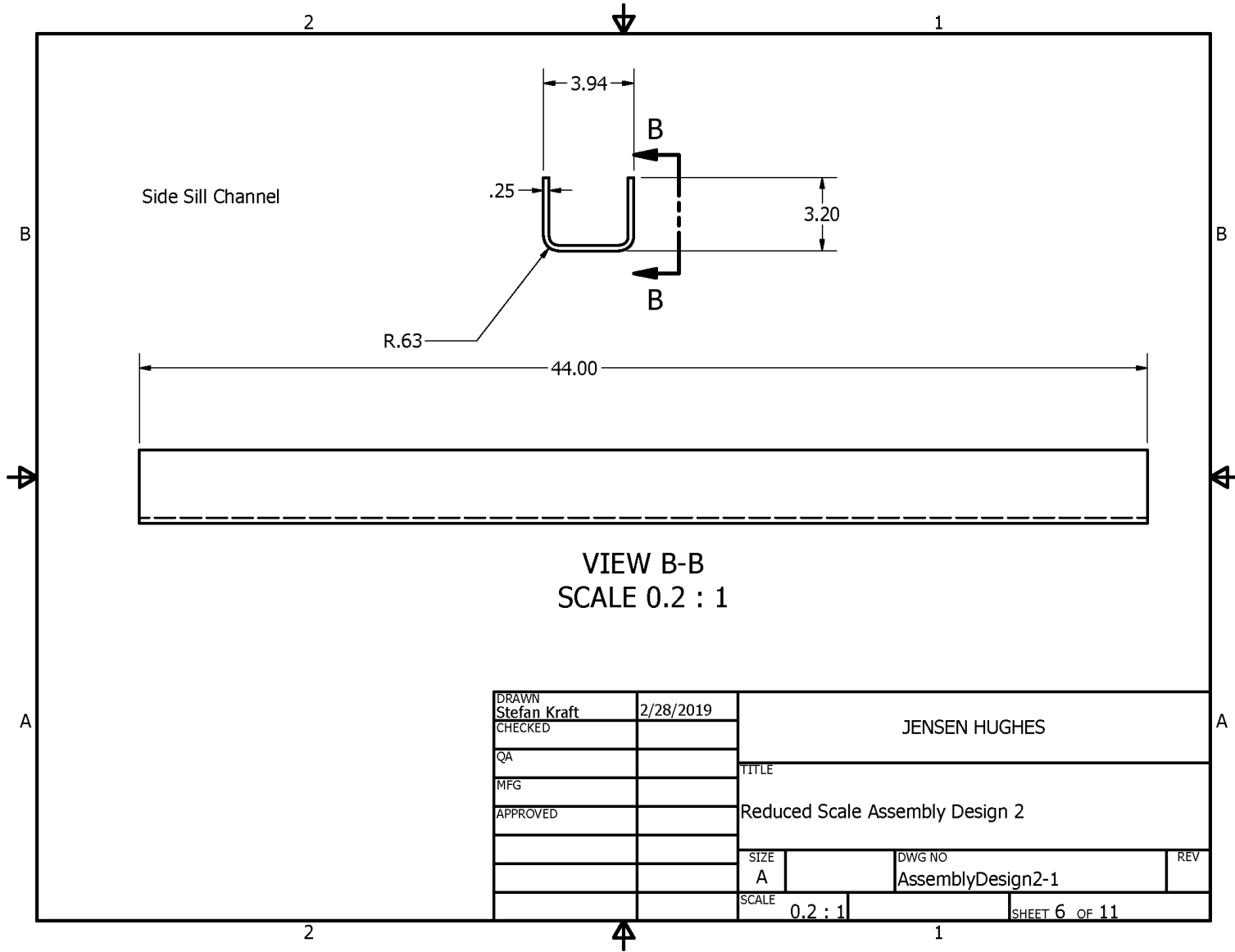
Figure B25. Test Article 3b assembly drawing sheet 6

119

Z-Channel

2.14

.060

G

3.94

1.10

G

102.50

VIEW G-G
SCALE 1 : 15

DRAWN Stefan Kraft	2/28/2019	JENSEN HUGHES		
CHECKED				
QA		TITLE		
MFG				
APPROVED		Reduced Scale Assembly Design 2		
		SIZE A	DWG NO AssemblyDesign2-1	REV
		SCALE 1 : 2		SHEET 7 OF 11
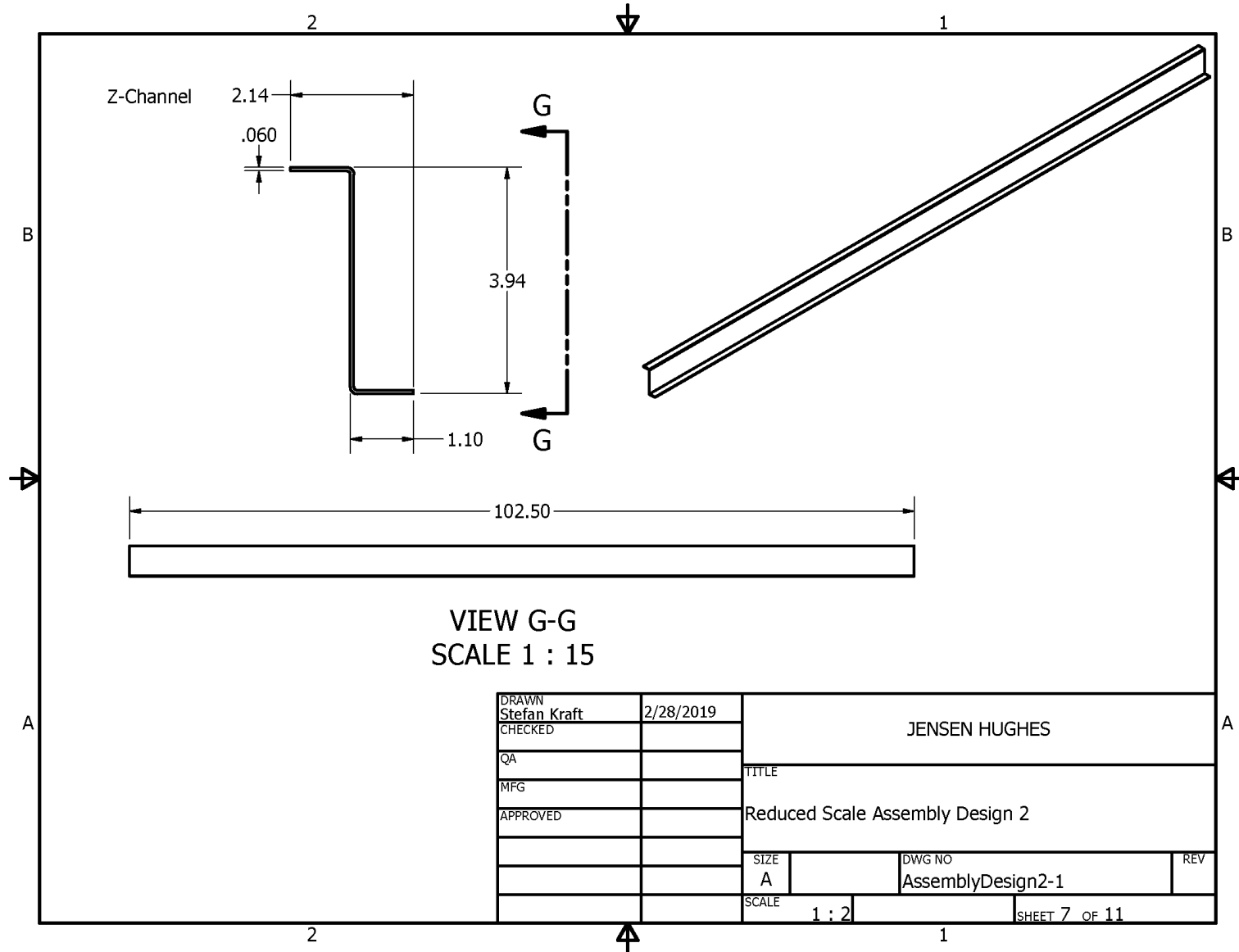
Figure B26. Test Article 3b assembly drawing sheet 7

3.20

Z-Channel Gusset

10.50

.063

B B

Side Sill Cap

.063

A .38

3.44

DRAWN Stefan Kraft	2/28/2019	JENSEN HUGHES	
CHECKED			
QA		TITLE	
MFG			
APPROVED		Reduced Scale Assembly Design 2	

6.00

SIZE A		DWG NO AssemblyDesign2-1	REV
SCALE 1 / 4		SHEET 8 OF 11	
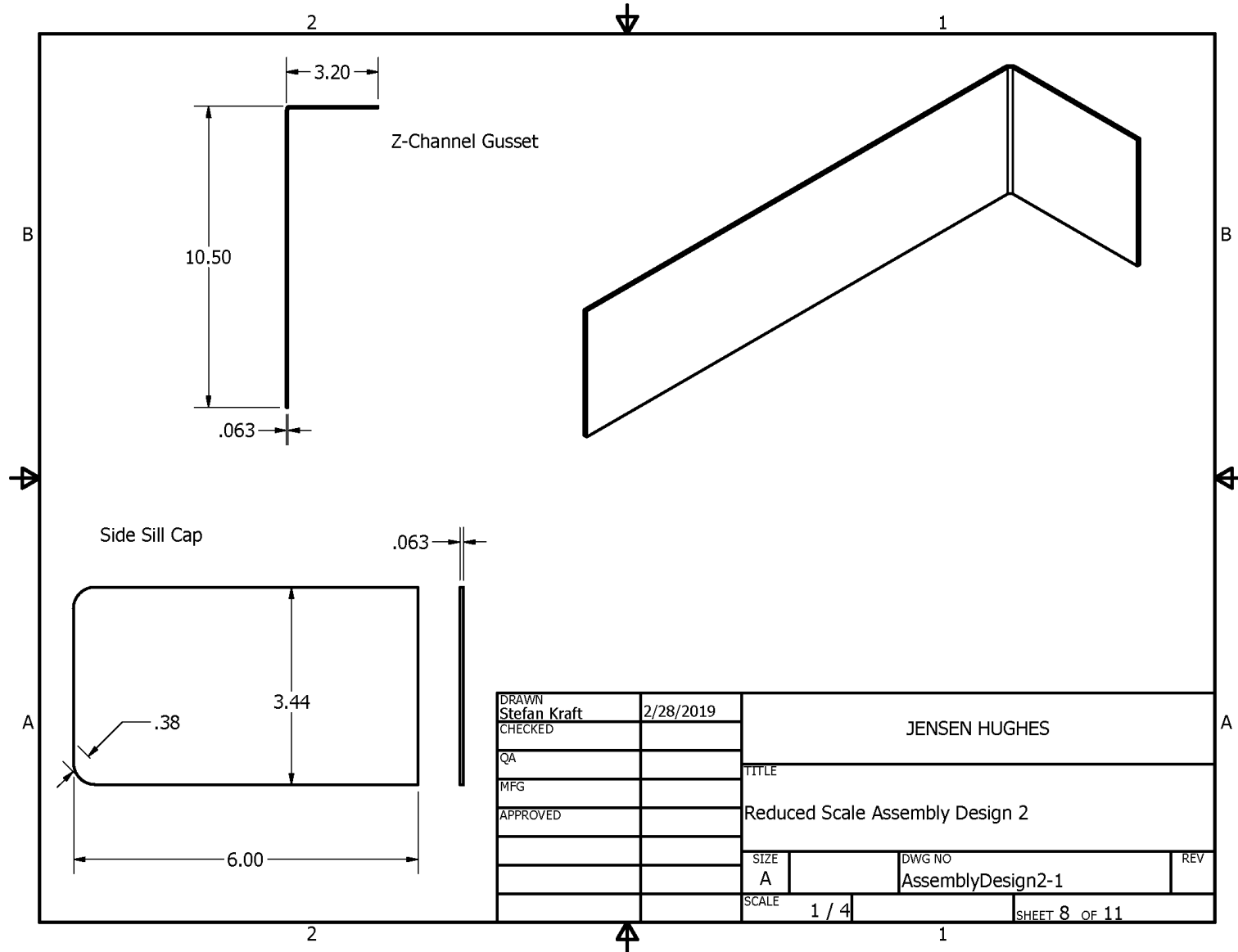
Figure B27. Test Article 3b assembly drawing sheet 8

Center Sill Bottom Plate

Bottom Sheet

← 44.00 →

← 12.50 →

B   B

44.00

106.40

.25

.063

DRAWN Stefan Kraft	2/28/2019	JENSEN HUGHES		
CHECKED				
QA		TITLE		
MFG				
APPROVED		Reduced Scale Assembly Design 2		
		SIZE A	DWG NO AssemblyDesign2-1	REV
		SCALE 0.07 : 1		SHEET 9 OF 11

A   A
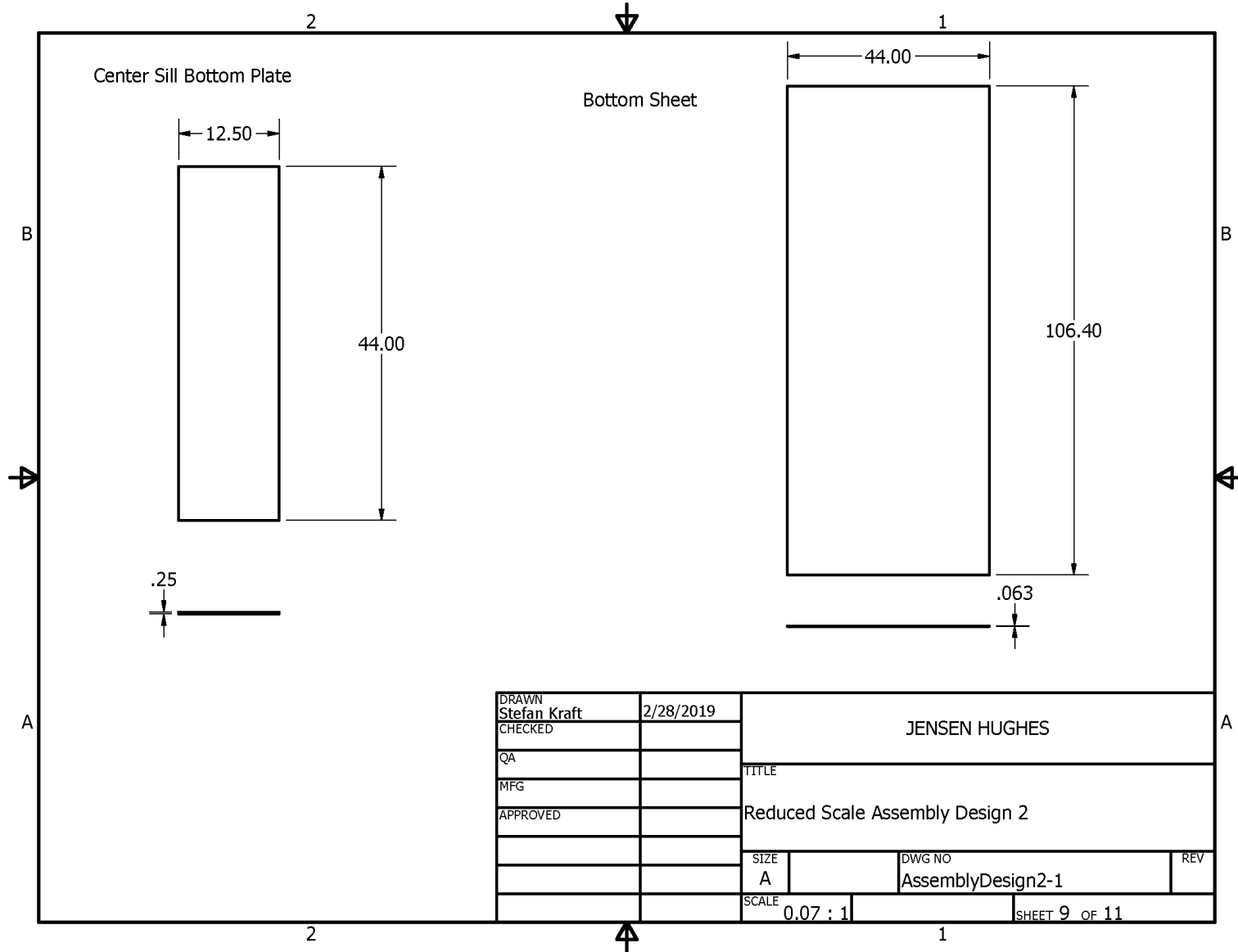
Figure B28. Test Article 3b assembly drawing sheet 9

Center Sill Channel

44.00

3.25

8.00

.25

8.00

DRAWN Stefan Kraft	2/28/2019	JENSEN HUGHES	
CHECKED			
QA		TITLE	
MFG			
APPROVED		Reduced Scale Assembly Design 2	
		SIZE A	DWG NO AssemblyDesign2-1	REV
		SCALE 1/8	SHEET 10 OF 11
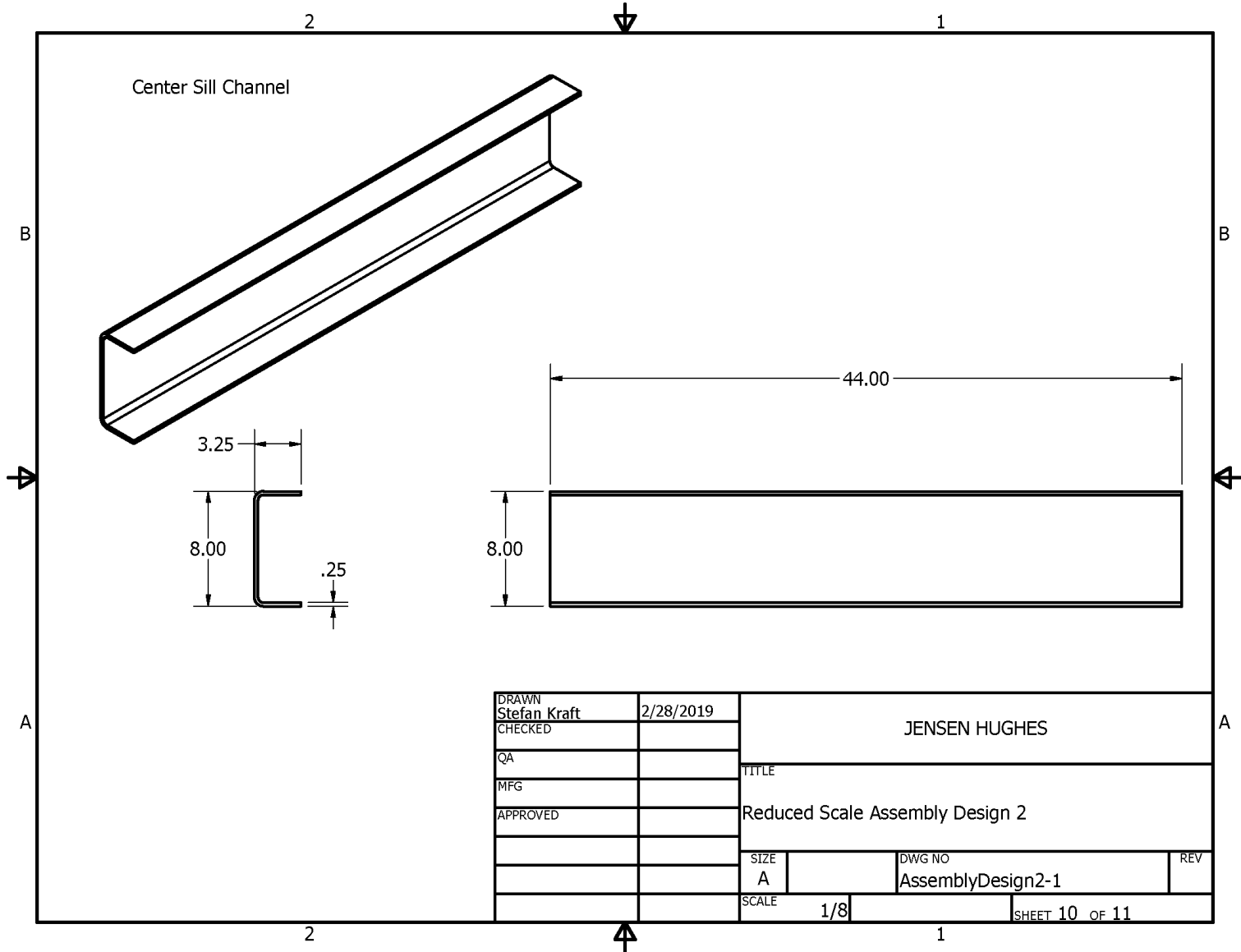
Figure B29. Test Article 3b assembly drawing sheet 10

DRAWN			
Stefan Kraft	2/28/2019	JENSEN HUGHES	
CHECKED			
QA		TITLE	
MFG			
APPROVED		Reduced Scale Assembly Design 2	

SIZE		DWG NO	REV
A		AssemblyDesign2-1	

SCALE			
1 / 8		SHEET 11 OF 11	
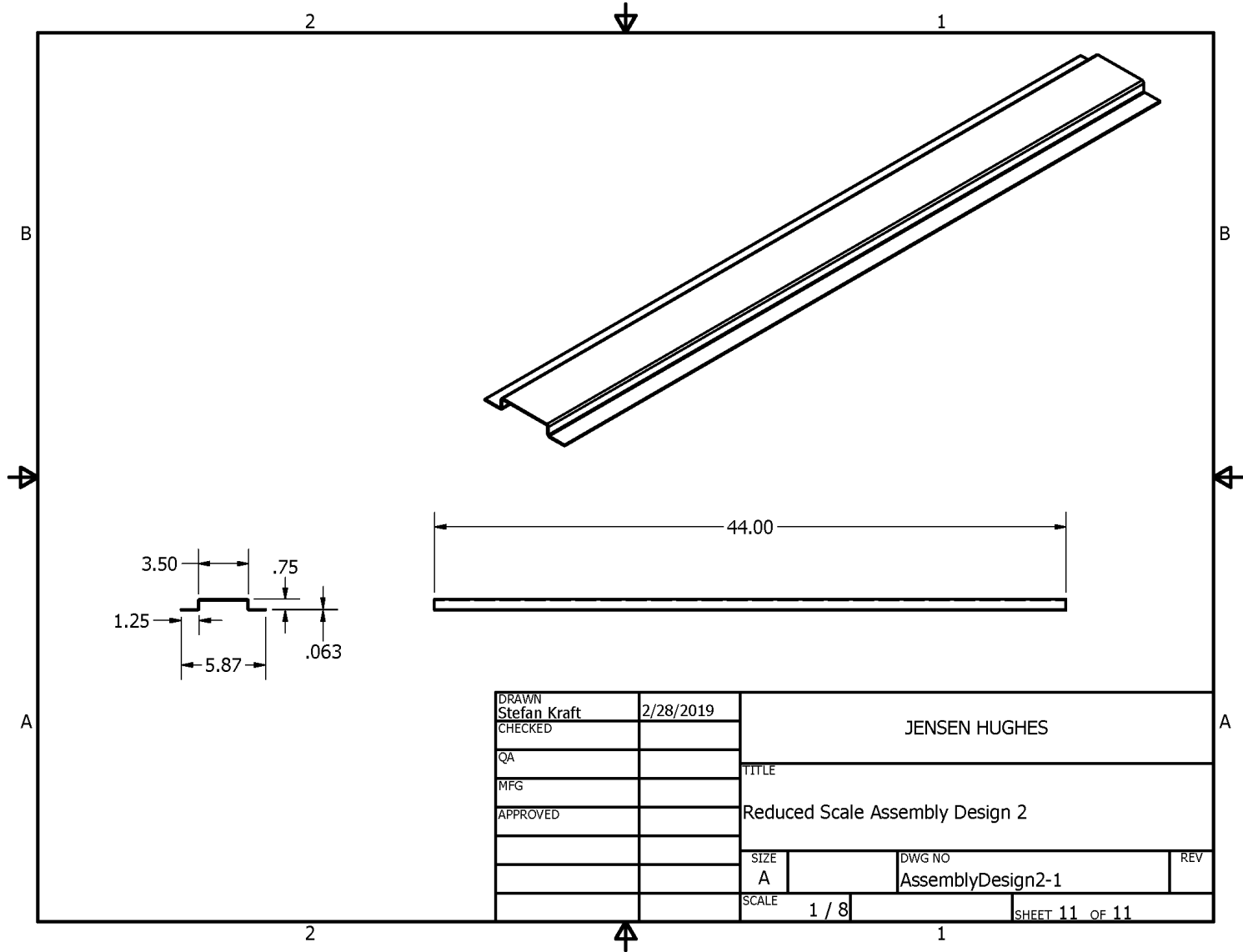
Figure B30. Test Article 3b assembly drawing sheet 11

124

Abbreviations and Acronyms

ACRONYMS	EXPLANATION
CFR	Code of Federal Regulations
CAE	Complete Abaqus Environment
FRA	Federal Railroad Administration
FRP	Fiber Reinforced Polymer
FE	Finite Element
FEA	Finite Element Analysis
FDS	Fire Dynamics Simulator
NFPA	National Fire Protection Association
SCE	Shuffled Complex Evolution
SwRI	Southwest Research Institute
TC	Thermocouple
Virginia Tech	Virginia Polytechnic Institute and State University